

TUNNEL BASED SPIN INJECTION DEVICES FOR
SEMICONDUCTOR SPINTRONICS

A DISSERTATION
SUBMITTED TO THE DEPARTMENT OF APPLIED PHYSICS
AND THE COMMITTEE ON GRADUATE STUDIES
OF STANFORD UNIVERSITY
IN PARTIAL FULFILLMENT OF THE REQUIREMENTS
FOR THE DEGREE OF
DOCTOR OF PHILOSOPHY

Xin Jiang
February 2004

© Copyright by Xin Jiang 2004
All Rights Reserved

I certify that I have read this dissertation and that, in my opinion, it is fully adequate in scope and quality as a dissertation for the degree of Doctor of Philosophy.

James S. Harris
(Principal Co-Advisor)

I certify that I have read this dissertation and that, in my opinion, it is fully adequate in scope and quality as a dissertation for the degree of Doctor of Philosophy.

Stuart S. P. Parkin
(Principal Co-Advisor)

I certify that I have read this dissertation and that, in my opinion, it is fully adequate in scope and quality as a dissertation for the degree of Doctor of Philosophy.

Walter A. Harrison

Approved for the University Committee on Graduate Studies.

Abstract

This dissertation summarizes the work on spin-dependent electron transport and spin injection in tunnel based spintronic devices. In particular, it focuses on a novel three terminal hot electron device combining ferromagnetic metals and semiconductors – the magnetic tunnel transistor (MTT).

The MTT has extremely high magnetic field sensitivity and is a useful tool to explore spin-dependent electron transport in metals, semiconductors, and at their interfaces over a wide energy range. In Chap. 1, the basic concept and fabrication of the MTT are discussed. Two types of MTTs, with ferromagnetic single and spin-valve base layers, respectively, are introduced and compared. In the following chapters, the transport properties of the MTT are discussed in detail, including the spin-dependent hot electron attenuation lengths in CoFe and NiFe thin films on GaAs (Chap. 2), the bias voltage dependence of the magneto-current (Chap. 3), the giant magneto-current effect in MTTs with a spin-valve base (Chap. 4), and the influence of non-magnetic seed layers on magneto-electronic properties of MTTs with a Si collector (Chap. 5).

Chap. 6 concentrates on electrical injection of spin-polarized electrons into semiconductors, which is an essential ingredient in semiconductor spintronics. Two types of spin injectors are discussed: an MTT injector and a CoFe/MgO tunnel injector. The spin polarization of the injected electron current is detected optically by measuring the circular polarization of electroluminescence from a quantum well light emitting diode. Using an MTT injector a spin polarization of $\sim 10\%$ is found for injection electron energy of ~ 2 eV at 1.4 K. This moderate spin polarization is most likely limited by significant electron spin relaxation at high energy. Much higher spin injection efficiency is obtained by using a CoFe/MgO tunnel injector with spin polarization

values of $\sim 50\%$ at 100K. The temperature and bias dependence of the electroluminescence polarization provides insight into spin relaxation mechanisms within the semiconductor heterostructure.

Acknowledgments

I first met Dr. Harris in 1998 when I was looking for a research topic for my Ph.D.'s degree. He introduced me into the world of spins and coached me as my advisor through the past years. He has always had confidence in me, encouraging me and being patient with me even when I was making little progress. He has also been a great source of knowledge and information when I encountered difficulties in my research.

In 2000, Dr. Parkin from IBM Almaden research center initiated a joint project on spin injection with Dr. Harris. As part of the collaboration, I started to work in Dr. Parkin's lab at Almaden, which turned out to be much more rewarding than I ever expected. As my advisor, Dr. Parkin gave me tremendous support and guidance. He showed me what it takes to be a great researcher: creativity, hard-working, enthusiasm, and optimism.

There is a long list of people that I am indebted to. I worked very closely with Sebastiaan van Dijken, then a post-doc at IBM, for one year and a half. He was my mentor and taught me how to conduct research. Roger Wang, Robert Shelby, Roger Macfarlane and Glenn Solomon have been my collaborators for a long time. I am grateful to them for all the fun that we had together. Alex Panchula and Christian Kaiser are wonderful friends, who make life interesting both in and outside the lab. Kevin Roche, See-hun Yang, Brian Hughes and Mahesh Samant gave me a lot of help in the lab. Ron Marks, Andrew Kellock, Phil Rice, Vaughn Deline, and Dolores Miller assisted me with AFM, RBS, TEM, SIMS, Auger, and XPS analysis. Robin Farrow generously shared his knowledge and experience with me. Dan Grupp and Olaf van 't Erve taught me the basics about spin-dependent electron transport at the

beginning stage of my research. Seth Bank, Zhigang Xie, Kai Ma grew high quality GaAs quantum well structures for me. Douglas King helped me with the optical measurements.

Dr. Harrison provided important insights into the interpretation of the bias voltage dependence of the magneto-current in the magnetic tunnel transistor. I enjoyed his lectures on solid state physics.

I want to thank other members of the Parkin group at IBM Almaden research center and the Harris group at Stanford University. I am thankful to Gail Chuncreech, Paula Perron, and Claire Nicholas for their administration assistance.

The financial support from Mr. and Mrs. Dwight through the Stanford Graduate Fellowship gave me freedom to pursue my interests during my first three years at Stanford University.

I can never say enough about how I appreciate the support from my family and friends over all these years. Especially, I would like to thank my parents and my wife. They have brought so much love and happiness into my life and really made it joyful and complete.

Contents

Abstract	v
Acknowledgments	vii
1 Magnetic Tunnel Transistors (MTTs)	1
1.1 Magnetic Tunnel Transistors	1
1.2 Fabrication of Magnetic Tunnel Transistors	8
2 Hot Electron Attenuation Lengths	13
2.1 Introduction	13
2.2 Attenuation Lengths in $\text{Ni}_{81}\text{Fe}_{19}$ Thin Films	16
2.3 Attenuation Lengths in $\text{Co}_{84}\text{Fe}_{16}$ Thin Films	20
2.4 Discussion	24
3 Bias Dependence of Magneto-Current (MC)	31
3.1 Introduction	31
3.2 Experiment	32
3.3 Model	34
3.4 Discussion	39
4 MTTs with a Spin-Valve Base	49
4.1 Introduction	49
4.2 Giant MC Effect	50
4.3 Comparison of Cu and Au Spacer Layers	55

5	Seed Layers for MTTs with a Si collector	61
5.1	Introduction	61
5.2	Magnetic Switching	62
5.3	Transfer Ratio	68
5.4	Magneto-Current	72
5.5	Magnetic Anisotropy	74
5.6	SIMS Analysis	78
5.7	Discussion and Summary	80
6	Spin Injection	83
6.1	Introduction	83
6.2	Selection Rules and Spin Relaxation Mechanisms	85
6.3	Spin Injection from an MTT Injector	87
6.4	Spin Injection from a CoFe/MgO Injector	95
7	Summary	105
	Bibliography	109

List of Tables

3.1	Overview of typical MTT structures.	32
3.2	Electron effective masses of the GaAs Γ , L and X conduction bands. .	40
4.1	Comparison of TMR and MC.	52
5.1	Schottky barrier heights at the metal/Si(001) interfaces.	71

List of Figures

1.1	Band diagram of an SVT.	2
1.2	Band diagram of an MTT with a single layer base.	3
1.3	I_C vs. H for a single layer base MTT.	5
1.4	Band diagram of an MTT with a spin-valve base.	5
1.5	I_C vs. H for a spin-valve base MTT.	7
1.6	Schematic drawing of a sample fabricated with shadow masks.	10
1.7	Photo of an MTT fabricated with shadow masks.	10
1.8	MC vs. V_{EB} at room temperature for a single layer base MTT.	11
2.1	I_C/I_E as a function of the $\text{Ni}_{81}\text{Fe}_{19}$ base layer thickness.	17
2.2	Majority electron attenuation length in $\text{Ni}_{81}\text{Fe}_{19}$	17
2.3	MC as a function of the $\text{Ni}_{81}\text{Fe}_{19}$ base layer thickness.	18
2.4	Minority electron attenuation length in $\text{Ni}_{81}\text{Fe}_{19}$	19
2.5	Ratio of majority to minority electron attenuation lengths in $\text{Ni}_{81}\text{Fe}_{19}$	19
2.6	I_C/I_E as a function of the $\text{Co}_{84}\text{Fe}_{16}$ base layer thickness.	21
2.7	Majority electron attenuation length in $\text{Co}_{84}\text{Fe}_{16}$	22
2.8	MC as a function of the $\text{Co}_{84}\text{Fe}_{16}$ base layer thickness.	22
2.9	Minority electron attenuation length in $\text{Co}_{84}\text{Fe}_{16}$	23
2.10	Ratio of majority to minority electron attenuation lengths in $\text{Co}_{84}\text{Fe}_{16}$	23
2.11	Transfer ratio at $t = 0$ for $\text{Ni}_{81}\text{Fe}_{19}$ and $\text{Co}_{84}\text{Fe}_{16}$ base layers.	28
2.12	Required base layer thicknesses for 95% and 98% spin-polarized electron current.	29
3.1	Bias voltage dependence of the MC.	33

3.2	Calculated hot electron angular distributions.	36
3.3	Calculated hot electron energy distributions.	36
3.4	Cartoon of the majority and minority electron collection.	38
3.5	Fits to the MC and I_C/I_E data for an MTT with a GaAs collector. . .	39
3.6	Same as Fig. 3.5, but assuming narrow angular distributions.	42
3.7	Same as Fig. 3.5, but assuming different angular distributions for the majority and minority electrons.	43
3.8	Same as Fig. 3.5, but assuming identical energy distributions for the majority and minority electrons.	45
3.9	Fits to the MC and I_C/I_E data for an MTT with a Si collector. . . .	47
4.1	MC and P_{Tran} as a function of the ferromagnetic layer thickness. . . .	52
4.2	Bias dependence of the MC and TR.	53
4.3	TR vs. V_{EB} for MTTs with single layer and spin-valve bases.	54
4.4	I_C vs. H for MTTs with Cu and Au spacer layers.	56
4.5	MC vs. V_{EB} for MTTs with Cu and Au spacer layers.	57
4.6	TR vs. V_{EB} for MTTs with Cu and Au spacer layers.	58
4.7	GMR of spin-valve bases with Cu and Au spacer layers.	60
5.1	I_C and base magnetic moments as a function of the magnetic field for MTTs without a seed layer.	63
5.2	I_C vs. H for spin-valve MTTs with seed layers.	65
5.3	I_C and base magnetic moments as a function of the magnetic field for MTTs with Cu and Au seed layers.	66
5.4	NiFe and CoFe switching fields.	67
5.5	TR as a function of seed layer material and thickness at $V_{EB} = 1.0$ V. .	69
5.6	TR vs. V_{EB} for MTTs with Cu and Pt seed layers.	70
5.7	TR as a function of seed layer material and thickness at $V_{EB} = 1.4$ V. .	71
5.8	MC as a function of the electron energy.	73
5.9	I_C as a function of the magnetic field applied along different directions for an MTT without a seed layer.	75

5.10	I_C as a function of the magnetic field applied along different directions for an MTT with a Cu seed layer.	76
5.11	MC as a function of the magnetic field direction for MTTs with a Cu seed layer.	77
5.12	MC as a function of the magnetic field direction for MTTs with or without seed layers.	78
5.13	SIMS analysis of metal silicide formation.	79
5.14	SIMS analysis of Si depth profiles.	80
6.1	Optical selection rules in the Faraday geometry.	86
6.2	An MTT spin injector with a QW detector.	88
6.3	Optical setup for the EL polarization measurements.	89
6.4	EL spectrum for an MTT injector.	91
6.5	EL polarization as a function of the magnetic field for an MTT injector.	92
6.6	Collector/base bias dependence of EL polarization and intensity.	94
6.7	A CoFe/MgO spin injector with a QW detector.	97
6.8	EL spectrum for a CoFe/MgO injector.	98
6.9	EL polarization as a function of the magnetic field for a CoFe/MgO injector.	99
6.10	Bias and temperature dependence of P_C for a CoFe/MgO injector.	101
6.11	Measured and calculated temperature dependence of P_C for a CoFe/MgO injector.	102

Chapter 1

Magnetic Tunnel Transistors

1.1 Magnetic Tunnel Transistors

The development of modern electronic devices has followed Moore's law for several decades [1]. As the device size continues to shrink towards fundamental physical limits, there is an increasing interest in exploring alternate technologies. Spin-based electronics, or spintronics, is a promising technology, where the spin states of carriers are utilized as an additional degree of freedom for information processing and storage. It could lead to a new generation of electronics with novel functionalities and superior device performance [2].

Spins have played a central role in magneto-electronic devices, such as spin-valves and magnetic tunnel junctions (MTJs), for a long time. The spin-valve consists of two ferromagnetic (FM) metal layers separated by a non-magnetic metal spacer layer, while the MTJ is comprised of two ferromagnetic metal electrodes separated by a thin insulating tunnel barrier. The resistance of these devices is found to be sensitive to the alignment of magnetic moments within the multilayered structures. The discovery of the giant magnetoresistance (GMR) effect in spin-valves [3–6] and the tunneling magnetoresistance (TMR) effect in MTJs [7–9] has had a profound impact on the storage and recording industry [10]. It makes high speed, high performance magnetic sensors and hard disk drives available and promises a new non-volatile memory, the magnetic random access memory (MRAM) [11].

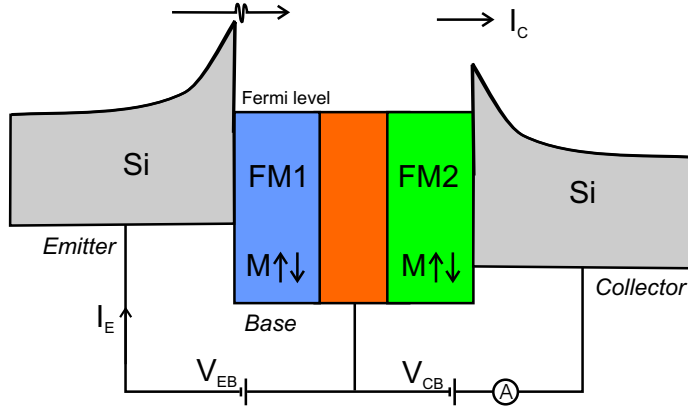


Fig. 1.1: Band diagram of an SVT.

In devices such as spin-valves, electron transport occurs at an energy near the Fermi level of the metals. Spin-dependent transport of hot electrons, i.e., electrons with energies much above the Fermi level, can also be very important for the functionality of magneto-electronic devices. One interesting hot electron device is the spin-valve transistor (SVT) (Fig. 1.1), which is comprised of a semiconductor emitter, a metal spin-valve base and a semiconductor collector, with Schottky barriers formed at the metal/semiconductor interfaces [12, 13]. When the emitter Schottky barrier is forward biased, hot electrons are injected from the emitter into the base and subsequently travel across the base region. Upon arrival at the base/collector interface, a portion of these electrons, which maintains enough energy to overcome the collector Schottky barrier, forms the collector current in the semiconductor. The magnitude of the collector current is very sensitive to spin-dependent electron scattering in the base region, and therefore, depends on the alignment of magnetic moments within the spin-valve base. The relative change in the collector current when the alignment is varied from anti-parallel to parallel, denoted as the magneto-current, can be as high as 560% at 80 K and 350% at 290 K [14]. The large magneto-current effect makes the SVT attractive as a magnetic sensor. However, in the SVT, the hot electron energy is limited by the emitter Schottky barrier height to about 0.9 eV, which leads to a small collector current and a very limited energy range for device operation.

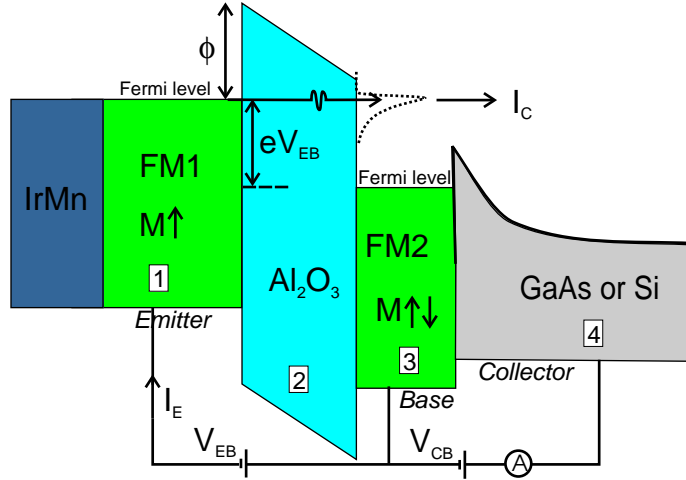


Fig. 1.2: Band diagram of an MTT with a single layer base.

In the magnetic tunnel transistor (MTT), a tunnel barrier replaces the emitter Schottky barrier [15–17]. As a result, the hot electron energy can easily be controlled by the emitter/base bias voltage (V_{EB}) across the tunnel barrier, giving rise to a larger collector current and a wider energy range for device operation than the SVT. Fig. 1.2 shows one type of the MTT, where the emitter (region 1) and base (region 3) each consists of a single ferromagnetic metal layer, FM1 and FM2, respectively. The collector (region 4) is a n-type semiconductor, such as GaAs or Si, which forms a Schottky barrier with the metal base. An anti-ferromagnetic layer (e.g., IrMn) is grown next to the emitter, which pins the emitter magnetic moment orientation through exchange bias [18]. Consequently, the base magnetic moment orientation can be switched by applying an appropriate external magnetic field while keeping the emitter magnetic moment direction unaltered. When the tunnel barrier is forward biased, spin-polarized hot electrons are injected from the emitter into the base and form the emitter current (I_E). These electrons experience spin-dependent scattering as they traverse the base region. The scattering rate is lower for electrons that have a spin direction parallel to the majority spin direction in the base (referred to as the majority electrons hereafter) and is higher for electrons with the opposite spin direction (referred to as the minority electrons hereafter). When the electrons reach the base/collector interface, only those that maintain enough energy to surmount

the Schottky barrier and that can be transmitted into available states in the semiconductor conduction bands will be collected and contribute to the collector current (I_C). Scattering in the base layer causes the hot electrons to lose energy and/or change momentum, and consequently, reduces their chances of being collected. The minority electrons, with a higher scattering rate, are more likely to be eliminated from the collected current. In this sense, the ferromagnetic base layer acts as a spin filter and preferentially removes minority electrons from the collector current. In the parallel alignment of the emitter and base magnetic moments, most of the hot electrons are majority electrons which have a lower scattering rate, giving rise to a large collector current. In the anti-parallel alignment, most of the hot electrons are minority electrons and are thus less likely to be collected, which results in a small collector current. The relative change in the collector current, when the alignment of the emitter and base magnetic moments is varied from anti-parallel to parallel, is a measure of the magnetic field sensitivity of the MTT device, which is quantified by the magneto-current (MC):

$$MC = \frac{I_{C,P} - I_{C,AP}}{I_{C,AP}} \quad (1.1)$$

where $I_{C,P}$ and $I_{C,AP}$ are the collector currents in the parallel and anti-parallel alignment of the emitter and base magnetic moments, respectively. Another important parameter of the MTT device is the amount of output current for a given input current, which is defined as the transfer ratio (TR):

$$TR = \frac{I_{C,P}}{I_E} \quad (1.2)$$

In Fig. 1.3, the collector current at 77 K is depicted as a function of the magnetic field for a typical single layer base MTT with the following structure:

$$\text{GaAs}(111)/30 \text{ \AA} \text{ Co}_{84}\text{Fe}_{16}/23 \text{ \AA} \text{ Al}_2\text{O}_3/50 \text{ \AA} \text{ Co}_{84}\text{Fe}_{16}/300 \text{ \AA} \text{ Ir}_{22}\text{Mn}_{78}/50 \text{ \AA} \text{ Ta}$$

As the magnetic field is swept between ± 80 Oe, the base magnetic moment switches at ~ 20 Oe, while the emitter magnetic moment remains the same orientation in the applied field range. At $V_{EB} = 1.0$ V, $I_{C,P}$ (~ 11.5 nA) is almost twice as large as $I_{C,AP}$, giving rise to an MC value of 97% and a transfer ratio of 7.6×10^{-6} .

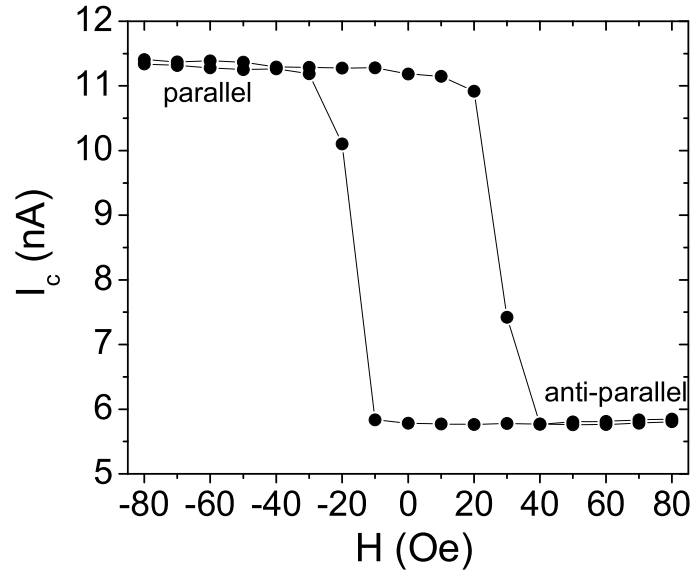


Fig. 1.3: Collector current as a function of the magnetic field for a single layer base MTT at 77 K with $V_{EB} = 1.0$ V.

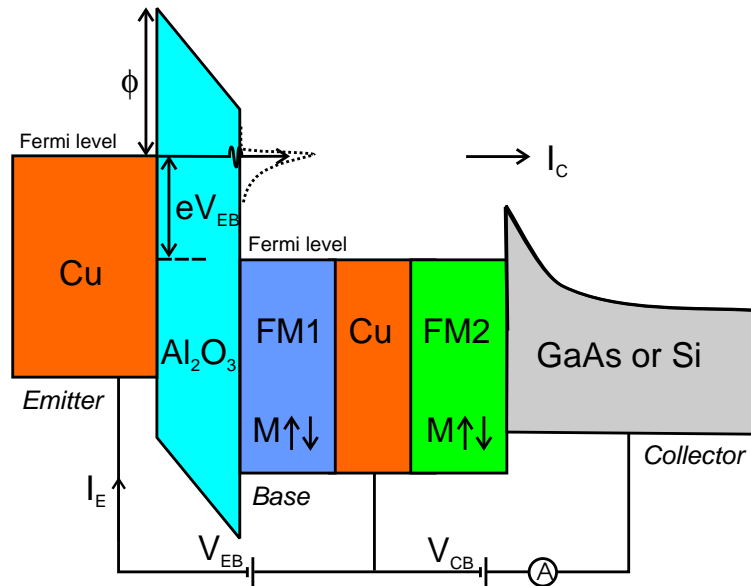


Fig. 1.4: Band diagram of an MTT with a spin-valve base.

A different type of MTT is shown in Fig. 1.4, where the emitter is a non-magnetic Cu layer and the base consists of a spin-valve structure FM1/Cu/FM2 [19, 20]. Due to spin-dependent electron scattering, the unpolarized hot electrons injected from the emitter into the base become spin-polarized after passing through the first ferromagnetic layer FM1. The subsequent transmission of these electrons through the second ferromagnetic layer FM2 is extremely sensitive to the alignment of the magnetic moments of FM1 and FM2, giving rise to a giant MC effect. The realization of parallel and anti-parallel magnetic configurations requires distinct switching fields for the magnetic moments within the spin-valve base, which can be readily achieved by, for example, choosing materials with different coercivities such as CoFe and NiFe to be FM1 and FM2.

In the single layer base MTT, the magnitude of the MC is determined by both the spin polarization of the emitter current (the emitter spin polarization) and the spin-filtering effect in the ferromagnetic base. The emitter spin polarization for typical ferromagnetic $3d$ transition metals, when an Al_2O_3 tunnel barrier is used, is about 45% [21], while spin-filtering in the base can result in a spin polarization of more than 95% when the base layer thickness is large compared to the minority electron attenuation length [22]. Therefore, the MC in a single layer base MTT is often limited by the emitter spin polarization to be on the order of 100%. In contrast, the spin-valve base MTT is free of such a limitation since it relies solely on spin-filtering in the ferromagnetic layers. Consequently, a much larger MC effect can be obtained. More detailed discussions on this topic will be given in Chap. 4.

Fig. 1.5 shows the magnetic field dependence of the collector current of a spin-valve base MTT at 77 K with $V_{EB} = 0.8$ V and 2.5 V. The MTT structure is given by:

$$\text{GaAs}(001)/50 \text{ \AA} \quad \text{Co}_{70}\text{Fe}_{30}/40 \text{ \AA} \quad \text{Cu}/50 \text{ \AA} \quad \text{Ni}_{81}\text{Fe}_{19}/25 \text{ \AA} \quad \text{Al}_2\text{O}_3/300 \text{ \AA} \quad \text{Cu}$$

The NiFe and CoFe layers have distinct switching fields of ~ 20 Oe and ~ 120 Oe, respectively. For magnetic fields larger than 120 Oe, both the NiFe and CoFe moments are aligned with the field and the collector current is maximized. As the field is swept, the abrupt switching of the NiFe moment gives rise to an almost perfect anti-parallel

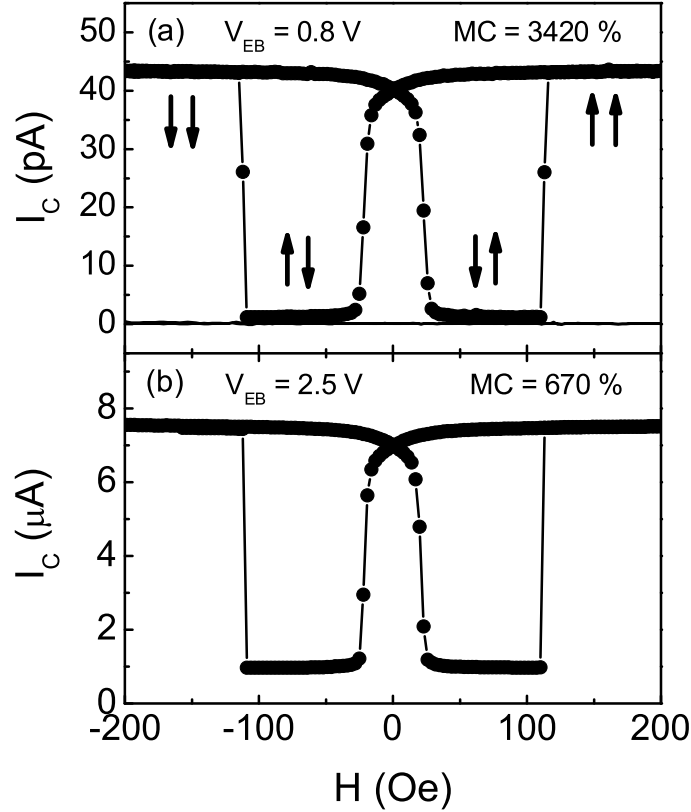


Fig. 1.5: Collector current as a function of the magnetic field for a spin-valve base MTT at 77 K with $V_{EB} = 0.8$ V (a) and 2.5 V (b). The solid line in (a) is the Schottky barrier leakage current. The arrows in (a) denote the CoFe and NiFe magnetic moment orientations.

alignment of the base moments and minimizes the collector current. The large change in the collector current leads to a giant MC value exceeding 3400% at $V_{EB} = 0.8$ V. The solid line in Fig. 1.5(a) is the collector current measured at $V_{EB} = 0.6$ V, which indicates a negligible leakage current of the Schottky barrier. At high bias voltages, the MC value is reduced, but is still quite large. More importantly, the collector current is significantly increased, reaching 7.5 μ A at $V_{EB} = 2.5$ V, while maintaining an MC value of 670%. The large output current, in combination with the huge MC

effect, is very attractive for device applications.

1.2 Fabrication of Magnetic Tunnel Transistors

The magnetic tunnel transistors are fabricated with a combination of deposition techniques including dc magnetron sputtering and ion beam sputtering at ambient temperature. Both n-type GaAs and Si substrates are used as the MTT collector. The GaAs substrates are two-inch round wafers purchased from AXT Inc. with two different crystalline orientations (001) and (111). The doping concentrations are $0.7 - 3.6 \times 10^{17} \text{ cm}^{-3}$ and $3 - 5.4 \times 10^{16} \text{ cm}^{-3}$ for the (001) and (111) substrate, respectively. Since the deposition system can only process one-inch substrates, the GaAs wafers are cleaved into quarters before loading into the system. The Si(001) substrates are one-inch round wafers purchased from Virginia Semiconductor Inc. with a doping concentration of $0.5 - 2 \times 10^{15} \text{ cm}^{-3}$ and a surface oxide thickness of $\sim 250 \text{ \AA}$.

Hot electron transport in the MTT device is very sensitive to scattering at the metal/semiconductor interface. Excessive interface scattering can drastically reduce the magnitude and spin polarization of the collector current. The latter is particularly harmful when the MTT is used for electrical injection of spin-polarized currents into semiconductors. Therefore, great care has to be taken in order to prepare a clean semiconductor interface before film deposition. The GaAs substrates are cleaned by thermal annealing at $\sim 490 - 550 \text{ }^\circ\text{C}$ in situ to remove surface oxide after they are loaded into the deposition chamber. The Si substrates are cleaned using a series of cleaning steps in the following order: eight minutes in an ultra-violet ozone cleaning system, three minutes in a deionized water bath, three minutes in an isopropanol vapor degreaser, and three minutes in a hot nitrogen tunnel. The surface silicon oxide is then removed by dipping the wafers into a 6% hydrofluoric acid solution for one minute. After the oxide removal, the Si substrates are cleaned using deionized water. By doing this, the Si surface is passivated with hydrogen. These passivated substrates are then promptly loaded into the deposition chamber for film growth.

The MTT with a GaAs collector is grown in an advanced sputtering system (A-system) equipped with six dc magnetron sputtering guns, five ion beam sputtering targets, two effusion cells, and a plasma oxidation source. The base pressure of the chamber prior to film deposition is in the low 10^{-8} Torr range. The ferromagnetic and non-magnetic metals are normally sputtered in pure argon gas at 3 mTorr pressure. Oxides and nitrides can be reactively sputtered by introducing a small amount of oxygen or nitrogen into the argon gas during deposition. The optimal oxygen or nitrogen content and sputtering gas pressure depend on the particular oxides or nitrides that are grown. Oxides can also be grown by first depositing a metal film and subsequently oxidizing it with an oxygen plasma. Ion beam sputtering is carried out in pure Xenon gas at a pressure of $\sim 7 \times 10^{-5}$ Torr. The anti-ferromagnetic IrMn film, which serves as the exchange bias coupling layer, is normally deposited by ion beam sputtering in the A-system. A shadow masking technique is used to fabricate the MTT. A maximum of twenty-four one-inch substrates and eight metal shadow masks can be loaded into the system at one time.

The MTT with a Si collector is grown in a simpler but otherwise similar sputtering system (S-system), which is equipped with six dc magnetron guns and a plasma oxidation source. The S-system has a base pressure in the low 10^{-9} Torr range prior to film deposition. A maximum of twenty one-inch substrates and eight shadow masks can be loaded at once. Magnetron sputtering, reactive sputtering, and plasma oxidation procedures in the S-system are similar to those in the A-system. Deposition of IrMn films is done by magnetron sputtering in the S-system.

Three shadow masks are used to form the base, the isolation pads, and the emitter of the MTT, respectively. The base layer, as indicated by the long rectangles in Fig. 1.6, is first deposited as two $1 \times 8 \text{ mm}^2$ and one $1 \times 10 \text{ mm}^2$ pads. A thin oxide tunnel barrier is then deposited covering the entire wafer by either plasma oxidation or reactive sputtering. The dark pads in Fig. 1.7 are isolation layers which electrically insulate the emitter from the base and the semiconductor collector. They are formed by reactive sputtering of a thick oxide layer (usually $200 - 600 \text{ \AA}$ Al_2O_3). Finally, the emitter layer is deposited. Ten MTT devices are fabricated on each substrate with two different active junction areas of $\sim 100 \times 150 \text{ }\mu\text{m}^2$ and $100 \times 300 \text{ }\mu\text{m}^2$,

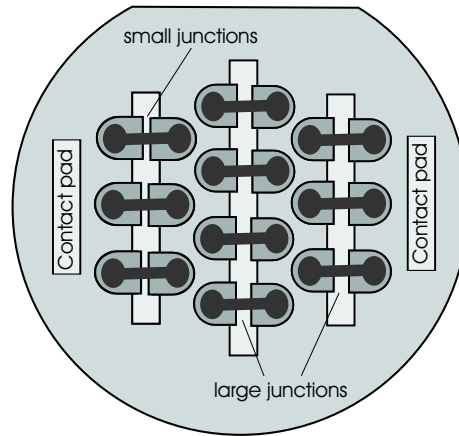


Fig. 1.6: Schematic drawing of ten MTJs and two contact pads fabricated with shadow masks.

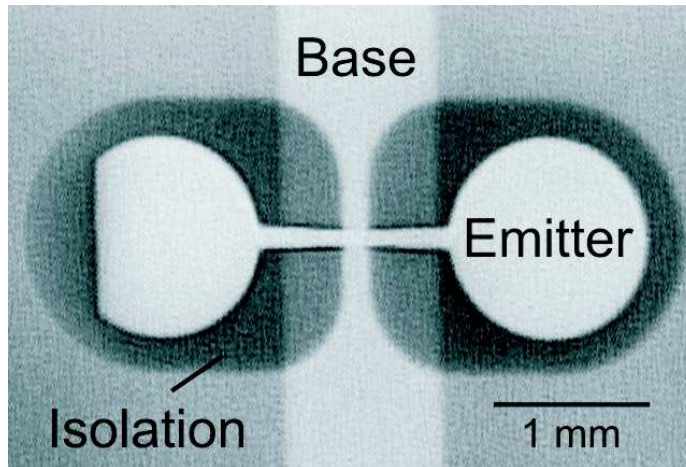


Fig. 1.7: Photo of an MTT fabricated with shadow masks.

respectively (Fig. 1.6). In addition, two rectangular contact pads are deposited during the MTT fabrication process. The contact pad on the right (Fig. 1.6) contains the base, the tunnel barrier and the emitter layers, while the contact pad on the left contains only the base and the tunnel barrier. These pads are used for contacting the semiconductor collector and for magnetic characterization measurements.

A disadvantage of the shadow masking technique is the resulting large base layer area, which is about 300 – 500 times larger than the active area of the MTT. This leads to a large Schottky barrier leakage current (I_{leak}) at room temperature. The

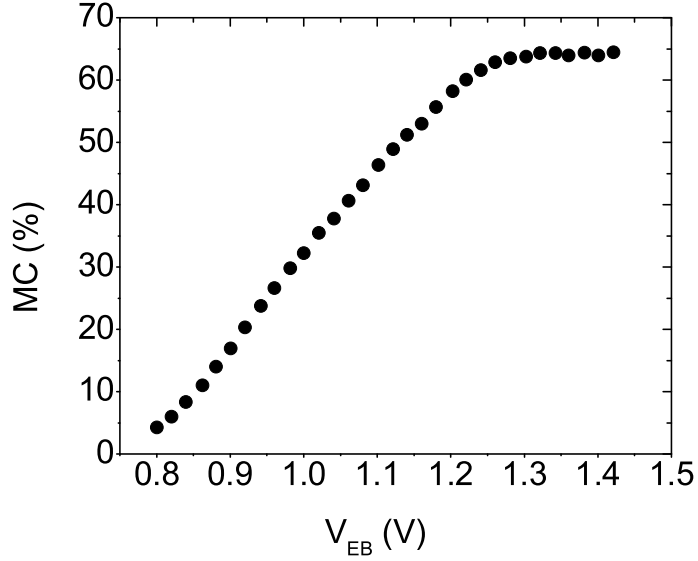


Fig. 1.8: MC as a function of the emitter/base bias voltage for a single layer base MTT at room temperature.

leakage current, unfortunately, does not depend on the alignment of the emitter and base magnetic moments and therefore can dramatically decrease the MC effect at low bias. When the leakage current is not negligible compared to the collector current, the measured MC is given by:

$$MC = \frac{(I_{C,P} + I_{leak}) - (I_{C,AP} + I_{leak})}{I_{C,AP} + I_{leak}} = \frac{I_{C,P} - I_{C,AP}}{I_{C,AP} + I_{leak}} \quad (1.3)$$

Thus, the larger the leakage current, the smaller the MC.

Fig. 1.8 shows the MC as a function of the emitter/base bias voltage at room temperature for the MTT described in Fig. 1.3. At low bias, the collector current is small and the MC effect is greatly reduced by the leakage current. At high bias, the collector current increases rapidly (see Chap 2). The influence of the leakage current can be ignored for bias above about 1.3 V, which leads to larger MC values.

Despite the leakage current problem at room temperature, the use of shadow masks

avoids time consuming lithography and allows fabrication of about twenty samples with different structures and materials in a single growth run. This enables thorough investigation of the MTT properties and comparison between various materials within a short time, which makes the shadow masking technique very attractive. The leakage current can be suppressed by conducting transport experiments at low temperatures. All the MTT transport measurements described in this dissertation are made at 77 K unless otherwise stated. In addition, the collector/base bias voltage (V_{CB}) is normally set to be zero to minimize the leakage current.

Chapter 2

Spin-Dependent Hot Electron Attenuation Lengths in Ferromagnetic Thin Films on GaAs(001)

2.1 Introduction

Much research has been stimulated into spin-dependent electron transport in ferromagnetic materials by its importance to the functionality of many magneto-electronic devices. For instance, Pappas *et al.* used spin-polarized photoemission to measure electron inelastic mean free paths (IMFP) in an Fe overlayer on Cu(001). They found a spin asymmetry in IMFP such that the minority electrons are scattered more strongly than the majority electrons at electron energies (E_E) of more than 10 eV (E_E is referenced to the Fermi energy E_F) [23]. Drouhin *et al.* [24] and Oberli *et al.* [25] studied spin-resolved electron transmission by passing electrons through free-standing ferromagnetic thin films and found similar asymmetries in the majority and minority electron transmission. The minimum electron energy in the photoemission and electron transmission experiments is limited by the work function of the ferromagnetic layer or the supporting materials to be more than ~ 2 eV, larger than the

upper edge of the minority electron d -band in ferromagnetic $3d$ transition metals, and therefore, far away from the energy range in which the maximum spin asymmetry between the majority and minority electrons is envisioned [26]. Aeschlimann *et al.* [27] studied spin-dependent electron lifetimes using two-photon photoemission (2PPE). In the 2PPE experiments, electrons in the ferromagnetic material are first excited by a laser pulse into an intermediate energy state below the vacuum level. After a time delay, a second laser pulse excites these electrons above the vacuum level and a photocurrent results. By analyzing the spin polarization of the photocurrent as a function of the delay time, the spin-dependent electron lifetimes at the intermediate energy level can be extracted. The 2PPE technique, in principle, can provide useful information about spin-dependent electron scattering from very low electron energies up to a few eV. However, due to time resolution constraints in the experiments, the electron energy is limited to less than 1.1 eV, above which the electron lifetimes are too short for reliable measurements. Finally, Vlutters *et al.* [28] used spin-valve transistors to investigate hot electron transport in NiFe thin films, where the electron energy is set by the Pt/Si Schottky barrier height to be about 0.9 eV.

The methods described above have difficulties covering the intermediate electron energy range of 1 – 2 eV. One useful technique which can solve this problem is ballistic electron magnetic microscopy (BEMM) [29], where hot electrons are injected into magnetic metal multilayers by a scanning tunneling microscope (STM) tip. The electron scattering asymmetry can be analyzed by measuring the transmitted electron current into a semiconductor collector. In addition, the energy of the electrons can be controlled by a bias voltage. An interesting alternative to BEMM is the magnetic tunnel transistor, which is capable of exploring an energy range of $\sim 0.7 - 2.5$ eV. In this chapter, the spin-dependent hot electron attenuation lengths in $\text{Ni}_{81}\text{Fe}_{19}$ and $\text{Co}_{84}\text{Fe}_{16}$ thin films on GaAs(001) are measured at various electron energies using the MTT [22]. The contribution of different electron scattering processes to the electron current attenuation in the bulk of the ferromagnetic layers and at the ferromagnetic metal/GaAs interface is discussed in detail. Furthermore, the potential application of the MTT as a highly spin-polarized electron source is discussed.

In a simple model ignoring spin-flip processes, the collector current in an MTT is

carried by the majority and minority electrons independently. The attenuation of hot electron current in each channel is described by the corresponding bulk attenuation length and interface collection efficiency. The collector current for parallel (P) and anti-parallel (AP) alignments of the emitter and base magnetic moments can therefore be written as:

$$I_{C,P(AP)} = I_E \frac{1 + P_E}{2} e^{-t/\lambda_{\uparrow(\downarrow)}} \alpha_{\uparrow(\downarrow)} + I_E \frac{1 - P_E}{2} e^{-t/\lambda_{\downarrow(\uparrow)}} \alpha_{\downarrow(\uparrow)} \quad (2.1)$$

where I_E is the emitter current, P_E is the emitter spin polarization, t is the base layer thickness, $\lambda_{\uparrow(\downarrow)}$ is the attenuation length for the majority (minority) electrons within the ferromagnetic base layer, and α is the electron collection efficiency at the base/collector interface. $\lambda_{\uparrow(\downarrow)}$ can be written in terms of attenuation lengths of individual scattering processes:

$$\frac{1}{\lambda_{\uparrow(\downarrow)}} = \frac{1}{\lambda_{el-el\uparrow(\downarrow)}} + \frac{1}{\lambda_{ph\uparrow(\downarrow)}} + \frac{1}{\lambda_{sw\uparrow(\downarrow)}} + \frac{1}{\lambda_{el\uparrow(\downarrow)}} \quad (2.2)$$

where $\lambda_{el-el\uparrow(\downarrow)}$, $\lambda_{ph\uparrow(\downarrow)}$, $\lambda_{sw\uparrow(\downarrow)}$, and $\lambda_{el\uparrow(\downarrow)}$ refer to attenuation lengths associated with electron-electron scattering, phonon scattering, spin wave scattering, and elastic scattering, respectively.

Note that the electron attenuation length $\lambda_{\uparrow(\downarrow)}$ describes the exponential decay of the hot electron current with increasing base layer thickness. Thus, $\lambda_{\uparrow(\downarrow)}$ is correlated, but not equivalent, to the electron scattering mean free path. For a GaAs collector, at electron energies barely above the collector Schottky barrier height, only a small portion of the Γ conduction band is available for electron collection. Therefore, only electrons with very small lateral wave vectors can be collected. Since a scattering event in the base region reduces the energy and/or changes the lateral wave vector of the electron, it almost certainly removes the scattered electron from the collector current. This, however, is no longer true at electron energies well above the Schottky barrier height since the scattered electron might still retain enough energy to overcome the Schottky barrier, even after losing a small amount of energy. Moreover, the number of GaAs conduction band states increases rapidly at elevated energies. Additional

conduction band states around the L and X points of the Brillouin zone also become available for electron collection at high energies. Thus, electrons with large lateral wave vectors can be collected as well and, as a consequence, the contribution of scattered electrons to the collector current is enhanced.

In Eq. 2.1, multiple passage of hot electrons through the ferromagnetic base layer is excluded. Since the hot electron attenuation length in ferromagnetic 3d transition metals is quite small [23, 30–33], the error introduced by such a simplification is negligible. For hot electron transport in noble metals such as Au, the multiple passage of electrons can be important [34].

The hot electron attenuation length $\lambda_{\uparrow(\downarrow)}$ provides important information about spin-dependent scattering in the ferromagnetic base layer. Using Eq. 2.1, it is possible to extract $\lambda_{\uparrow(\downarrow)}$ by measuring the base layer thickness dependence of the collector current in MTTs. For this purpose, a series of MTTs were fabricated in a single growth run with the following structure:

$$\text{GaAs}(001)/t \text{ base}/25 \text{ \AA} \text{ Al}_2\text{O}_3/50 \text{ \AA} \text{ Co}_{84}\text{Fe}_{16}/300 \text{ \AA} \text{ Ir}_{22}\text{Mn}_{78}/50 \text{ \AA} \text{ Ta}$$

where the base consisted of either $\text{Ni}_{81}\text{Fe}_{19}$ or $\text{Co}_{84}\text{Fe}_{16}$, and t was the film thickness. The Al_2O_3 barrier was formed by plasma oxidizing an 18-Å-thick Al film, which was deposited by magnetron sputtering. Details of the MTT fabrication is discussed in Chap 1. Transport measurements of these MTTs were conducted at 77 K in an energy range of 1.0 – 1.9 eV to determine the majority and minority electron attenuation lengths in $\text{Ni}_{81}\text{Fe}_{19}$ and $\text{Co}_{84}\text{Fe}_{16}$ thin films.

2.2 Attenuation Lengths in $\text{Ni}_{81}\text{Fe}_{19}$ Thin Films

In Fig. 2.1, the logarithm of I_C/I_E for parallel (solid circles) and anti-parallel (open circles) alignment of the emitter and base magnetic moments is plotted as a function of the $\text{Ni}_{81}\text{Fe}_{19}$ base layer thickness at $V_{EB} = 1.4$ V. In both cases, I_C/I_E decreases exponentially with the base layer thickness. The slopes of the solid lines, which represent linear fits to the data, only differ slightly. This indicates that the majority electrons, with a larger attenuation length, dominate the collector current

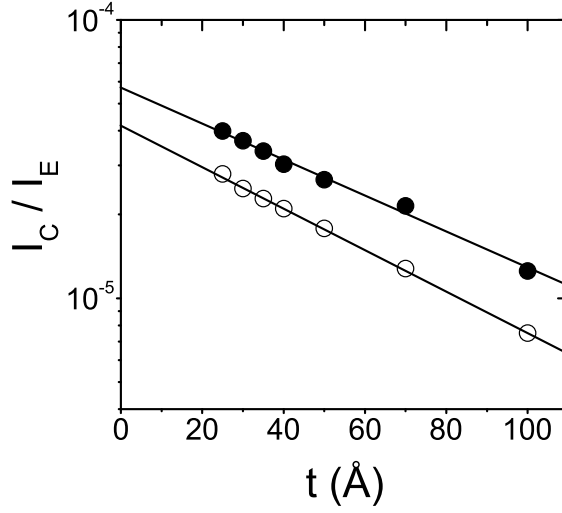


Fig. 2.1: I_C/I_E as a function of the $\text{Ni}_{81}\text{Fe}_{19}$ base layer thickness at $V_{EB} = 1.4$ V for parallel (solid circles) and anti-parallel (open circles) alignment of the emitter and base magnetic moments. The solid lines represent linear fits to the data.

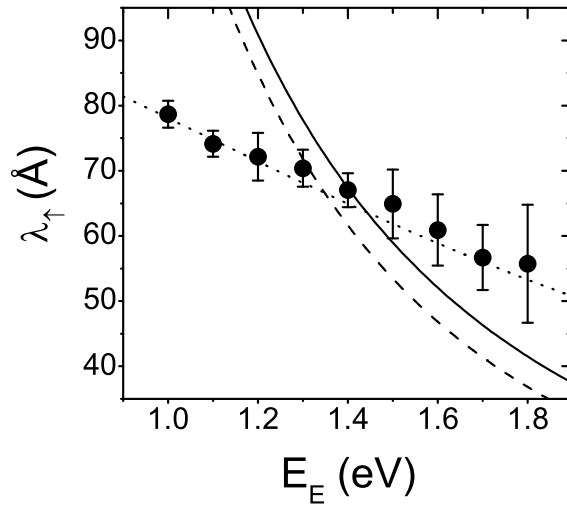


Fig. 2.2: Majority electron attenuation length in $\text{Ni}_{81}\text{Fe}_{19}$ (solid circles) as a function of the electron energy. The lines are model calculations discussed in Sec. 2.4.

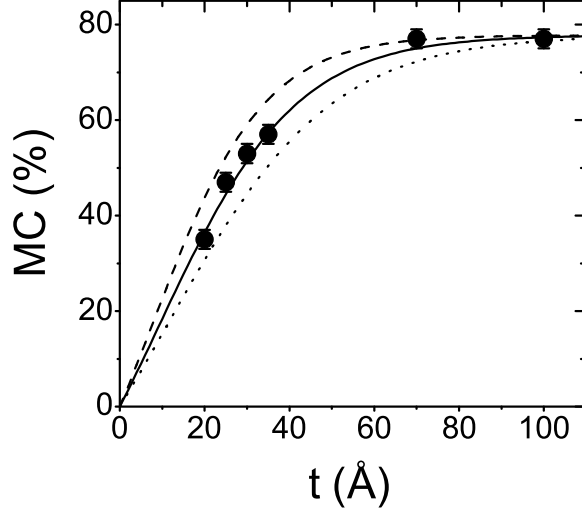


Fig. 2.3: MC as a function of the $\text{Ni}_{81}\text{Fe}_{19}$ base layer thickness at $V_{EB} = 1.4$ V. The lines represent fits for $\lambda_{\perp} = 11$ Å (dashed line), 13 Å (solid line), and 15 Å (dotted line).

in both alignments. Therefore, the terms including $e^{-t/\lambda_{\perp}}$ in Eq. 2.1 can be neglected at large base layer thicknesses in the parallel alignment. In this case, the right hand side of Eq. 2.1 reduces to a single exponential term containing $e^{-t/\lambda_{\perp}}$ and the slope of the linear fit is equal to $-1/(\lambda_{\perp}\ln 10)$. The fit for $\text{Ni}_{81}\text{Fe}_{19}$ yields a majority electron attenuation length $\lambda_{\uparrow} = 67.0 \pm 2.6$ Å at an electron energy $E_E = 1.4$ eV. The base layer thickness dependence of I_C/I_E is measured at various electron energies by varying the emitter/base bias voltage. The majority electron attenuation length is extracted at each energy in the same way as described above. The results for the energy range of 1.0 – 1.8 eV are shown in Fig. 2.2 (solid circles). The majority electron attenuation length decreases monotonically with electron energy from 79 Å at 1 eV to 56 Å at 1.8 eV, i.e., the scattering probability for the majority electrons is smaller at low electron energy.

The attenuation length of the minority electrons is determined by measurements of the magneto-current as a function of base layer thickness. The experimental results

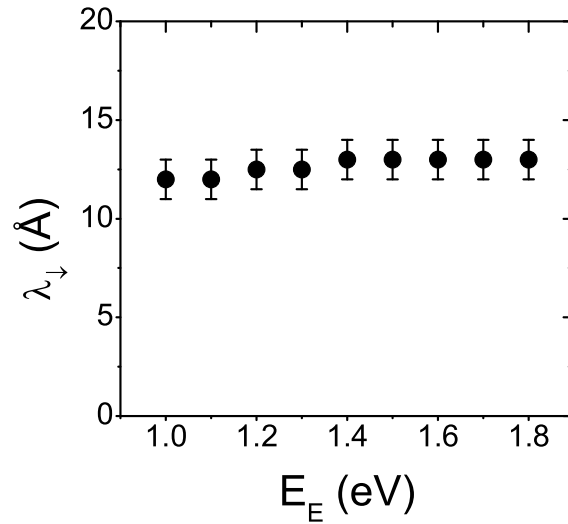


Fig. 2.4: Minority electron attenuation length in $\text{Ni}_{81}\text{Fe}_{19}$ as a function of the electron energy.

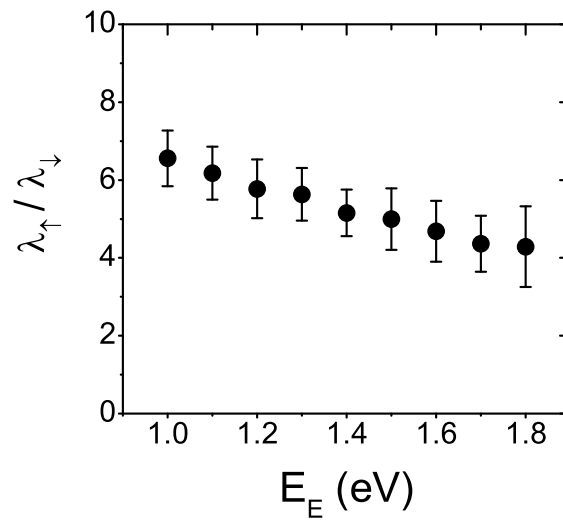


Fig. 2.5: Ratio of the majority to minority electron attenuation lengths in $\text{Ni}_{81}\text{Fe}_{19}$ as a function of the electron energy.

at $V_{EB} = 1.4$ eV are shown in Fig. 2.3 (solid circles). The MC initially increases with the base layer thickness, but subsequently saturates at $\sim 78\%$ for base layers thicker than ~ 60 Å. The constant value of the MC at large base layer thicknesses indicates that transport of the minority electrons across the base layer is negligibly small. In this case, the MC is determined mainly by the emitter spin polarization, P_E . At smaller base layer thicknesses, however, the minority electrons are not completely removed from the hot electron current, which diminishes the MC effect. The rapid decrease of the MC towards zero at thin base layer thicknesses suggests that electron scattering at the base/collector interface is largely spin-independent, i.e., $\alpha_{\uparrow} \approx \alpha_{\downarrow}$. The minority electron attenuation length can be determined by fitting the data in Fig. 2.3 with Eq. 2.1 and using the previously found majority electron attenuation length. Using fitting parameters $\lambda_{\uparrow} = 67$ Å, $P_E = 28\%$ and $\alpha_{\uparrow}/\alpha_{\downarrow} = 1$, the three lines displayed in Fig. 2.3 represent fits for $\lambda_{\downarrow} = 11$ Å (dashed line), 13 Å (solid line), and 15 Å (dotted line), respectively. This fitting procedure yields $\lambda_{\downarrow} = 13 \pm 1$ Å at an electron energy $E_E = 1.4$ eV. The attenuation length of the minority electrons is thus about five times smaller than that of the majority electrons at this energy.

The energy dependence of the minority electron attenuation length is determined by similar base layer thickness dependence measurements of the MC at different emitter/base bias voltages. The results are summarized in Fig. 2.4. Contrary to the majority electron attenuation length, the minority electron attenuation length is almost independent of the electron energy for $1.0 \text{ eV} \leq E_E \leq 1.8 \text{ eV}$. Fig. 2.5 shows the ratio of the majority to minority electron attenuation lengths as a function of the electron energy. The attenuation length ratio decreases from 6.5 at 1.0 eV to 4.2 at 1.8 eV. Spin-filtering in the $\text{Ni}_{81}\text{Fe}_{19}$ base layer is thus less efficient at elevated electron energies.

2.3 Attenuation Lengths in $\text{Co}_{84}\text{Fe}_{16}$ Thin Films

The logarithm of I_C/I_E for parallel (solid circles) and anti-parallel (open circles) alignment of the emitter and base magnetic moments is depicted in Fig. 2.6 as a function of the $\text{Co}_{84}\text{Fe}_{16}$ base layer thickness at $V_{EB} = 1.4$ V. Again, the slopes of the

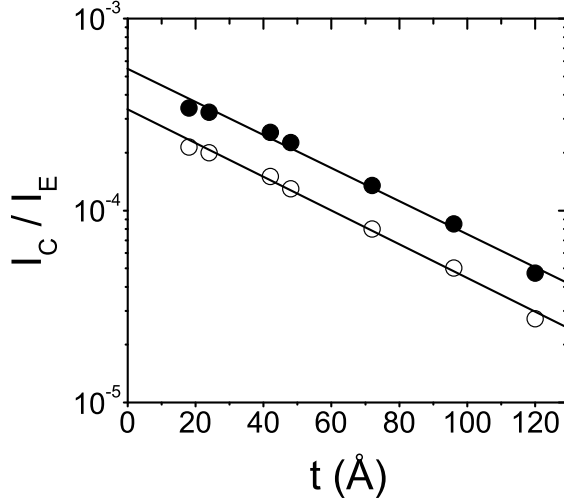


Fig. 2.6: I_C/I_E as a function of the $\text{Co}_{84}\text{Fe}_{16}$ base layer thickness at $V_{EB} = 1.4$ V for parallel (solid circles) and anti-parallel (open circles) alignment of the emitter and base magnetic moments. The solid lines represent linear fits to the data.

linear fits (solid lines) only differ slightly. Hence, the majority electron transmission dominates the collector current in both alignments. The slope of the fit to the data in the parallel alignment gives a majority electron attenuation length $\lambda_{\uparrow} = 50 \pm 3$ Å at $E_E = 1.4$ eV. The electron energy dependence of λ_{\uparrow} is shown in Fig. 2.7. Similar to what is observed in $\text{Ni}_{81}\text{Fe}_{19}$, the majority electron attenuation length in $\text{Co}_{84}\text{Fe}_{16}$ decreases monotonically with increasing electron energy from 58 Å at 1 eV to 43 Å at 1.9 eV.

Fig. 2.8 shows the MC as a function of the $\text{Co}_{84}\text{Fe}_{16}$ base layer thickness at $V_{EB} = 1.4$ V. Assuming negligible spin dependence of electron scattering at the base/collector interface, the solid line represents a fit using parameters $\alpha_{\uparrow}/\alpha_{\downarrow} = 1$, $P_E = 27\%$, $\lambda_{\uparrow} = 50$ Å, and $\lambda_{\downarrow} = 7$ Å, which agrees well with the data. However, the MC remains quite large when $\text{Co}_{84}\text{Fe}_{16}$ is used as the base layer, even at small film thicknesses. Therefore, the spin dependence of the base/collector interface scattering cannot be completely excluded. The dashed line in Fig. 2.8 represents a fit that accounts for spin-dependent interface scattering, which gives $\lambda_{\downarrow} = 11$ Å. Although this fit agrees

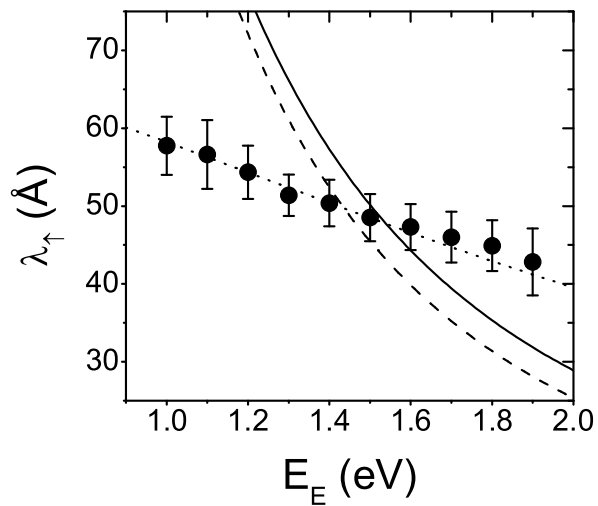


Fig. 2.7: Majority electron attenuation length in $\text{Co}_{84}\text{Fe}_{16}$ as a function of the hot electron energy (solid circles). The lines are model calculations discussed in Sec. 2.4.

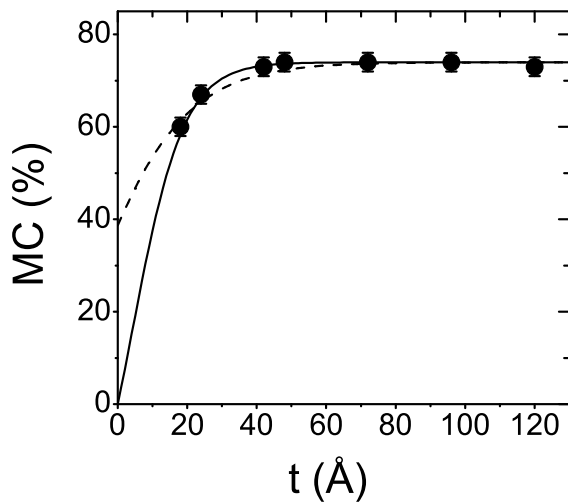


Fig. 2.8: MC as a function of the $\text{Co}_{84}\text{Fe}_{16}$ base layer thickness at $V_{EB} = 1.4$ V. The lines represent fits to the data assuming spin-independent (solid line) and spin-dependent (dashed line) electron scattering at the base/collector interface.

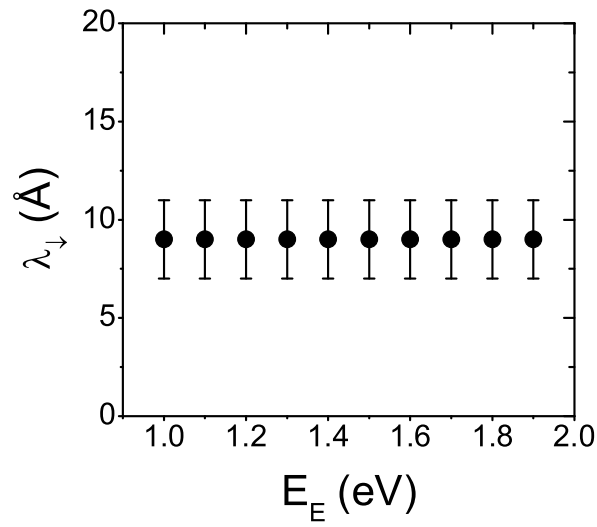


Fig. 2.9: Minority electron attenuation length in $\text{Co}_{84}\text{Fe}_{16}$ as a function of the electron energy.

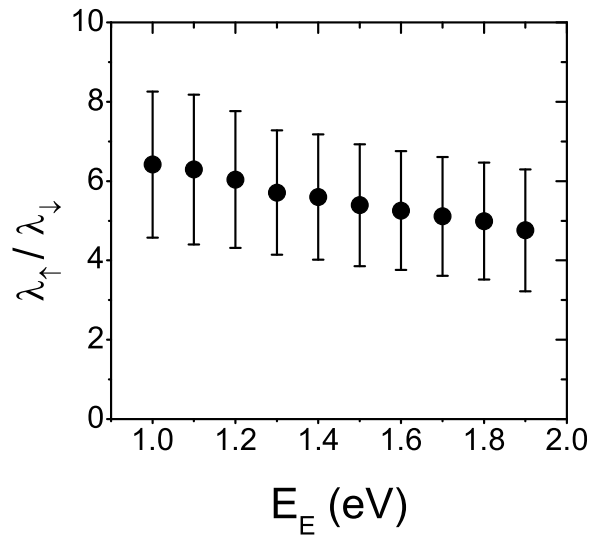


Fig. 2.10: Ratio of the majority to minority electron attenuation lengths in $\text{Co}_{84}\text{Fe}_{16}$ as a function of the electron energy.

reasonably well with the experimental data, it seems unlikely that interface electron scattering could give rise to such a large spin polarization of the hot electron current of nearly 40%. Studies of the bias voltage dependence of the MC in similar MTT devices suggest that electron scattering at the CoFe/GaAs interface broadens the electron angular distribution for both the majority and minority electrons to a similar extent (see Chap. 3), which implies that the spin asymmetry of the interface scattering is small. To unambiguously determine the spin dependence of the interface scattering and consequently the minority electron attenuation length requires fabrication and measurements of MTTs with very thin base layers. Unfortunately, the intermixing between $\text{Co}_{84}\text{Fe}_{16}$ and GaAs leads to a magnetically dead interface layer and degrades the performance of MTTs when the base layer is thinner than about 20 Å. Inserting a thin non-magnetic seed layer between the $\text{Co}_{84}\text{Fe}_{16}$ base and GaAs may be able to limit such intermixing and enable accurate measurements of the minority electron attenuation length. Further investigation is necessary to find the appropriate seed layer. In the present study, the minority electron attenuation length is taken as the average of the two fits discussed above, which gives $\lambda_{\downarrow} = 9 \pm 2$ Å at $E_E = 1.4$ eV.

The energy dependence of the minority electron attenuation length in $\text{Co}_{84}\text{Fe}_{16}$ is extracted from base layer thickness dependence measurements of the MC at different electron energies and the results are summarized in Fig. 2.9. Similar to what is observed in $\text{Ni}_{81}\text{Fe}_{19}$, the minority electron attenuation length is nearly constant in the energy range of 1.0 – 1.9 eV.

Fig. 2.10 shows the energy dependence of the attenuation length ratio $\lambda_{\uparrow}/\lambda_{\downarrow}$ in $\text{Co}_{84}\text{Fe}_{16}$ films on GaAs(001). The decrease of $\lambda_{\uparrow}/\lambda_{\downarrow}$ with electron energy leads to a reduction of hot electron spin polarization at elevated electron energies.

2.4 Discussion

The large spin asymmetry in hot electron scattering rates in ferromagnetic 3d transition metals is often considered to be a consequence of electron-electron interactions. The electron energy bands of 3d transition metals are split into a majority and a minority spin band. For $\text{Ni}_{81}\text{Fe}_{19}$ and $\text{Co}_{84}\text{Fe}_{16}$, the majority *d* band is fully

occupied, whereas a portion of the minority d band remains empty. Minority electron scattering into the empty d states just above the Fermi level is believed to be very efficient, while the majority electrons can only be scattered into the less abundant s - p states, which results in a larger scattering rate and therefore a smaller attenuation length for the minority electrons than for the majority electrons. This simple picture is in qualitative agreement with the experimental observations for hot electron scattering in $\text{Ni}_{81}\text{Fe}_{19}$ and $\text{Co}_{84}\text{Fe}_{16}$ thin films on GaAs(001). However, other scattering processes have to be considered in order to account for the energy dependence of the majority and minority electron attenuation lengths.

The electron-electron scattering rate in metals was studied by Quinn using a free electron model, where he found that the electron lifetime is inversely proportional to the square of the electron energy [35]. Since the attenuation length is equal to the product of the electron lifetime and velocity [proportional to $(E_E + E_F)^{1/2}$], it can be written as:

$$\lambda_{el-el\uparrow} = b_0(E_E + E_F)^{1/2}/E_E^2 \quad (2.3)$$

where b_0 is a proportionality prefactor. The free electron model predicts a very strong energy dependence of the electron attenuation length, as shown by the solid lines in Fig. 2.2 and Fig. 2.7, where the parameters used in the calculations are: $E_F = 9.5$ eV, $b_0 = 40$ for $\text{Ni}_{81}\text{Fe}_{19}$ and $E_F = 8.9$ eV, $b_0 = 35$ for $\text{Co}_{84}\text{Fe}_{16}$. The observed majority electron attenuation length, however, shows a much weaker energy dependence than the calculations. It decreases approximately linearly with electron energy, similar to the results obtained in ballistic electron emission microscopy experiments [34]. The free-electron model assumed a smooth density of states (DOS) of the electron energy band and used a Taylor expansion near the Fermi level to calculate the electron lifetime. Thus the calculated results, strictly speaking, are only valid at electron energies very close to the Fermi level. Zarate *et al.* included a more realistic DOS in their calculations and derived the following equation [36]:

$$\lambda_{el-el\uparrow} = a_0(E_E + E_F)^{1/2}/[E_E^2 + (E_E - \Delta E)^2/a_1] \quad (2.4)$$

where a_0 and a_1 are constants independent of energy, and ΔE is the energy difference

between the Fermi level and the upper edge of the majority d band. The dashed lines in Fig. 2.2 and Fig. 2.7 are calculated results using this modification with $a_0 = 40$ for $\text{Ni}_{81}\text{Fe}_{19}$ and 35 for $\text{Co}_{84}\text{Fe}_{16}$, $a_1 = 3.5$, and $\Delta E = 0.6$ eV. As can be seen, the energy dependence of the majority electron attenuation length is not significantly changed and the experimental data cannot be accounted for.

The majority electron attenuation length is also influenced by other scattering processes, such as phonon scattering, thermal spin wave scattering, and elastic scattering. Phonon scattering and thermal spin wave scattering are sensitive to temperature and relatively weak at 77 K. On the other hand, elastic electron scattering contributes to the hot electron current loss, but its energy dependence in the experimental energy range is not well known. The dotted lines in Fig. 2.2 and Fig. 2.7 are calculated results taking into account these scattering processes:

$$\frac{1}{\lambda_{\uparrow}} = \frac{1}{\lambda_{el-el\uparrow}} + \frac{1}{\lambda_{t\uparrow}} \quad (2.5)$$

where $\lambda_{el-el\uparrow}$ is calculated using Eq. 2.3 with $b_0 = 110$ and $\lambda_{t\uparrow}$ is the majority electron attenuation length due to scattering processes other than electron-electron interactions, which are assumed to be energy independent. $\lambda_{t\uparrow}$ values of 100 Å and 70 Å are used for $\text{Ni}_{81}\text{Fe}_{19}$ and $\text{Co}_{84}\text{Fe}_{16}$, respectively.

For both $\text{Ni}_{81}\text{Fe}_{19}$ and $\text{Co}_{84}\text{Fe}_{16}$, the attenuation length of the minority electrons is about 4 – 7 times smaller than that of the majority electrons at electron energies between 1.0 and 1.9 eV. This large spin asymmetry can in principle be explained by efficient scattering of the minority electrons into the empty d states just above the Fermi level. Calculations of electron-electron scattering, which take the structure of the majority and minority d bands into account, indeed predict a smaller scattering rate for the majority electrons than for the minority electrons [36–39]. Other spin-dependent processes, such as spin wave scattering [14, 28, 40–42] and elastic scattering [43], also contribute to the spin asymmetry. At low temperatures, thermal spin wave scattering is much weaker than spontaneous spin wave emission. Since spin waves carry an angular momentum equal to the momentum change of flipping a majority electron spin to a minority electron spin [44], spontaneous spin wave emission

is limited to minority electrons only in order to conserve the total angular momentum and turns them into majority electrons. This gives rise to a spin asymmetry in hot electron scattering rates. In a recent study it was argued that spontaneous spin wave emission can account for the large difference between the majority and minority attenuation lengths in the spin-valve transistor [28]. Hot electrons can be scattered elastically by the metal atoms, impurities, and defects in the ferromagnetic base layer. The spin-dependence of the cross section for elastic scattering originates from the exchange coupling between the electron and atom moments, which has been used to explain the spin asymmetry in electron transmission through thin Fe films [43]. Besides the three aforementioned scattering processes, a change in the minority electron velocity might also influence the energy dependence of the minority electron attenuation length. The upper edge of the minority d band is close to or even inside the electron energy range in which the experiments are conducted [36,37]. Consequently, a crossover from minority electrons traversing the base layer in the more localized d band to the more mobile s - p band might occur [26]. This crossover tends to increase the minority electron velocities, and therefore compensates for the higher scattering rates at elevated electron energies. Phonon scattering at 77 K is weak and should not contribute significantly to the observed spin asymmetry in the electron attenuation lengths.

In Fig. 2.1 and Fig. 2.6, $I_{C,P}/I_E$ varies exponentially with the base layer thickness t . The intercepts of the linear fits to the data give the extrapolated transfer ratio at $t = 0$, which is a measure of the electron collection efficiency at the base/collector interface. The energy dependence of the transfer ratio at $t = 0$ is summarized in Fig. 2.11 for $\text{Ni}_{81}\text{Fe}_{19}$ (open circles) and $\text{Co}_{84}\text{Fe}_{16}$ (solid circles). As can be seen, the hot electron current loss due to electron scattering at the base/collector interface is very large in both cases. In addition, the transfer ratio at $t = 0$ is much smaller for $\text{Ni}_{81}\text{Fe}_{19}/\text{GaAs}$ than for $\text{Co}_{84}\text{Fe}_{16}/\text{GaAs}$, suggesting that the interfacial hot electron scattering is about eight times stronger at the $\text{Ni}_{81}\text{Fe}_{19}/\text{GaAs}$ interface. For both materials, the transfer ratio at $t = 0$ increases with electron energy due to an increase of available conduction band states in GaAs for electron collection. Although the interface scattering is stronger for $\text{Ni}_{81}\text{Fe}_{19}$ films on GaAs(001), the data in Fig. 2.3

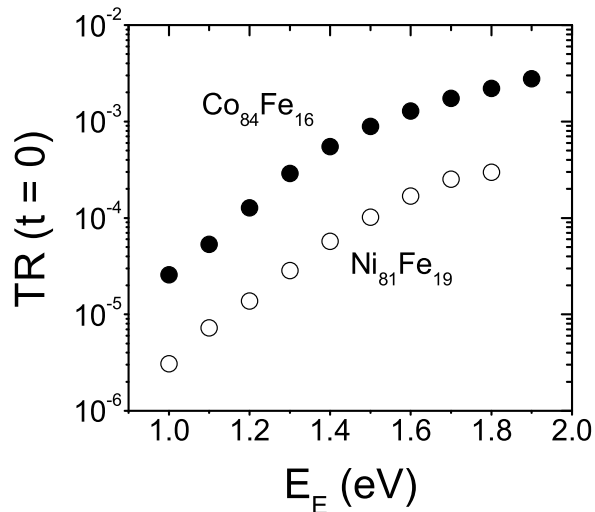


Fig. 2.11: Extrapolated transfer ratio at zero base layer thickness as a function of the hot electron energy for MTTs with a Ni₈₁Fe₁₉ (open circles) and a Co₈₄Fe₁₆ (solid circles) base, respectively.

suggest that its spin-dependence is negligible. On the other hand, the interface scattering is significantly weaker for Co₈₄Fe₁₆/GaAs, but its spin-dependence cannot be excluded. The difference between Ni₈₁Fe₁₉ and Co₈₄Fe₁₆ might be explained by interface alloying during the initial stage of the base layer growth. The growth of Co and Fe on GaAs differs from other transition metals in that they induce very limited substrate disruption [45, 46]. The disrupted Ga and As atoms outdiffuse into the metal layer. While the Ga atoms are mostly concentrated near the metal/GaAs interface, the As atoms exhibit a double decay profile, i.e., they are concentrated near both interfaces of the metal film with only a small quantity dissolved inside the metal bulk. On the other hand, rather extensive reactivity has been found at the Ni/GaAs(001) interface [47], leading to the formation of a NiGaAs compound which has a CsCl structure, such that Ni atoms occupy one sublattice and Ga or As atoms randomly occupy the other sublattice. This interfacial layer may lead to severe attenuation of the hot electron current. Besides the different alloying effects at the interface,

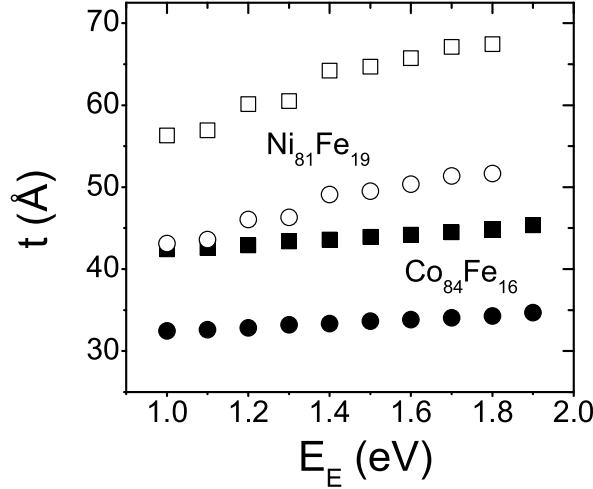


Fig. 2.12: Required base layer thicknesses to obtain 95% (circles) and 98% (squares) spin-polarized electron current at the base/collector interface as a function of the electron energy for a Ni₈₁Fe₁₉ (open symbols) and a Co₈₄Fe₁₆ (solid symbols) base layer.

the film structure and/or roughness might also contribute to an increased amount of scattering at the Ni₈₁Fe₁₉/GaAs interface than at the Co₈₄Fe₁₆/GaAs interface.

The magnetic tunnel transistor can be utilized to inject highly spin-polarized hot electron currents into semiconductors, which is a prerequisite for semiconductor spintronics. The realization of efficient spin injection from ferromagnetic materials into semiconductors could lead to an array of novel spintronic devices. Theoretical as well as experimental work over a number of years suggested, however, that it is difficult to achieve injection efficiencies of more than a few percent with diffusive ferromagnetic metal contacts due to a conductivity mismatch between the metals and the semiconductors [48–52]. One possible solution is to use the MTT device for spin injection. In the MTT, the electron transport takes place well above the Fermi level and thus is dominated by ballistic electron rather than diffusive electron transport. The use of a tunnel barrier is supported by recent theoretical work, which suggests that a tunnel based spin injector could overcome the conductivity mismatch problem and

enable efficient spin injection into semiconductors [53, 54]. An additional advantage of the MTT spin injector is the feasibility of nearly 100% spin-polarized electron currents at room temperature. Spin-filtering is very efficient in the ferromagnetic base layer due to the large asymmetry between the majority and minority attenuation lengths. Fig. 2.12 shows the needed $\text{Ni}_{81}\text{Fe}_{19}$ (open symbols) and $\text{Co}_{84}\text{Fe}_{16}$ (solid symbols) base layer thicknesses in order to produce 95% (squares) and 98% (circles) spin-polarized hot electron currents near the metal/semiconductor interface. Experimentally determined majority and minority electron attenuation lengths are used in these calculations and an emitter spin polarization of 30% is assumed, which is readily obtainable with CoFe [21]. Spin-filtering is more efficient in a $\text{Co}_{84}\text{Fe}_{16}$ base layer: a 32-Å-thick $\text{Co}_{84}\text{Fe}_{16}$ base layer produces a 95% spin-polarized current at $E_E = 1$ eV, and a 98% spin-polarized current is obtained with a 42-Å-thick $\text{Co}_{84}\text{Fe}_{16}$ base at the same energy. At higher energies, thicker base layers are required due to the decreased attenuation length ratio. Because of its better spin-filtering properties and a smaller amount of hot electron scattering at the base/collector interface, $\text{Co}_{84}\text{Fe}_{16}$ is a better base layer material for spin injection experiments than $\text{Ni}_{81}\text{Fe}_{19}$.

As a final note, the model discussed in this chapter does not explicitly consider the effects of the GaAs electronic structure on hot electron transport in the MTT, which will be shown in Chap. 3 to be very important. Instead, the influence of the GaAs conduction band structure on the collector current is included in the phenomenological parameters P_E and $\alpha_{\uparrow(\downarrow)}$, while the base layer thickness dependence of the collector current is described by the electron attenuation lengths $\lambda_{\uparrow(\downarrow)}$. As a result, the model may slightly overestimate the spin asymmetry in the electron attenuation lengths, especially at large electron energies. Despite the simplicity of this model, it accounts well for the experimental data and is helpful for understanding spin-dependent electron scattering in the magnetic tunnel transistor.

Chapter 3

Bias Voltage Dependence of the Magneto-Current

3.1 Introduction

The collector current and magneto-current of the MTT are very sensitive to electron scattering process in the base layers and at the base/collector interface, and also to the conduction band structure of the semiconductor collector. This means that the MTT can serve as a useful tool to investigate the electron scattering process as well as to probe the energy dependence of hot electron transport on the semiconductor electronic structure. One such example is presented in this chapter, in which the variation of the MC as a function of the emitter/base bias voltage, i.e., the hot electron energy, is studied in single layer base MTTs with GaAs(001), GaAs(111), and Si(001) collectors [55, 56]. For MTTs with either GaAs(001) or GaAs(111) collectors, a pronounced non-monotonic bias dependence of the MC is observed, whereas for MTTs with Si collectors the MC decreases monotonically with bias voltage. A model calculation reveals that spin-dependent inelastic electron scattering in the base layer and strong electron scattering at the base/collector interface give rise to the experimental observations. The different bias voltage dependences of the MC for MTTs with GaAs and Si collectors can be attributed to the distinct conduction band structures of GaAs and Si.

3.2 Experiment

A number of MTTs were fabricated with either GaAs or Si collectors using the procedures described in Chap. 1. The final structures of the MTTs were:

$$\text{collector}/t \text{ FM base}/23 \text{ \AA Al}_2\text{O}_3/50 \text{ \AA CoFe}/300 \text{ \AA Ir}_{22}\text{Mn}_{78}/50 \text{ \AA Ta}$$

where t was the thickness of the base layer, the FM base was formed from $\text{Co}_{84}\text{Fe}_{16}$, $\text{Co}_{70}\text{Fe}_{30}$, or $\text{Ni}_{81}\text{Fe}_{19}$, and the collector was n-type GaAs(001) (silicon doped, $0.7 - 3.6 \times 10^{17} \text{ cm}^{-3}$), GaAs(111) (silicon doped, $3 - 5.4 \times 10^{16} \text{ cm}^{-3}$), or Si(001) (phosphorus doped, $0.5 - 2 \times 10^{15} \text{ cm}^{-3}$). The Al_2O_3 tunnel barrier was formed by plasma oxidation of a sputtered Al thin film. The emitter CoFe was $\text{Co}_{84}\text{Fe}_{16}$ and $\text{Co}_{70}\text{Fe}_{30}$ for MTTs with GaAs and Si collectors, respectively. For MTTs with Si collectors, the $\text{Co}_{70}\text{Fe}_{30}$ base layer tends to react with the Si and form a silicide layer, which drastically degrades the device performance. In order to limit such silicide formation, a thin Fe layer can be inserted at the base/collector interface before growing the remainder of the base layer. This seed layer was found to improve the magneto-current and the breakdown voltage of the tunnel barrier. An overview of several typical MTT structures that have been studied is given in Table 3.1.

sample number	base	collector	TMR
1	30 \AA $\text{Co}_{84}\text{Fe}_{16}$	GaAs(001)	46.4%
2	45 \AA $\text{Co}_{84}\text{Fe}_{16}$	GaAs(001)	40.7%
3	100 \AA $\text{Co}_{84}\text{Fe}_{16}$	GaAs(001)	31.7%
4	74 \AA $\text{Ni}_{81}\text{Fe}_{19}$	GaAs(001)	14.7%
5	30 \AA $\text{Co}_{84}\text{Fe}_{16}$	GaAs(111)	29.0%
6	3 \AA Fe / 50 \AA $\text{Co}_{70}\text{Fe}_{30}$	Si(001)	33.8%

Table 3.1: Overview of typical MTT structures. The measured MC data are shown in Fig. 3.1.

The bias voltage dependence of the MC was measured at 77 K. The results are summarized in Fig. 3.1. The MTTs with GaAs collectors (sample 1 – 5) have various

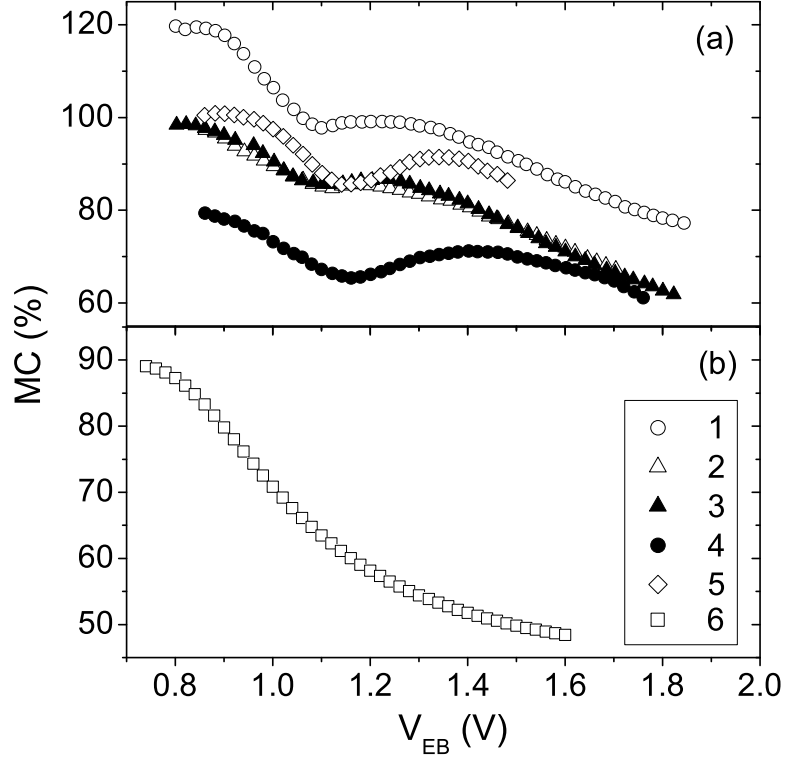


Fig. 3.1: Compilation of typical bias voltage dependences of the MC for various MTTs. The structural details for each of the six samples are given in Table 3.1.

base layer materials, and are grown on GaAs substrates with two different crystalline orientations. However, they all show a pronounced non-monotonic bias dependence of the MC: when the bias voltage V_{EB} exceeds the Schottky barrier height (~ 0.78 V from current-voltage measurements), a large MC is observed, which decreases with V_{EB} up to ~ 1.1 V, then increases slightly, and finally decreases gradually. Quantitative differences between the MC values of these samples can be attributed to variations in film growth and/or tunnel barrier formation. For example, the growth of magnetic tunnel junctions depends critically on the particular materials used. Moreover, the growth of the base layers can be quite different on GaAs(001) and GaAs(111) substrates. This is confirmed by large variations in the tunneling magnetoresistance

values measured for samples 1 – 5 (see Table 3.1).

Note that the MC values of sample 2 and 3 are smaller than that of sample 1 although they have thicker $\text{Co}_{84}\text{Fe}_{16}$ base layers. This appears to be inconsistent with the base layer thickness dependence of the spin-filtering effect. However, the MC of a single layer base MTT depends on both the spin-filtering effect in the base and the emitter spin polarization. When the ferromagnetic base layer is much thicker than the minority electron attenuation length, the MC is limited by the emitter spin polarization (see Chap. 2), which is very sensitive to the interface between the ferromagnetic metal and the tunnel barrier. The smaller MC of sample 2 and 3 can therefore be explained by different emitter spin polarizations due to different ferromagnetic metal/tunnel barrier interface formation. Another important consideration is that the maximum spin-filtering effect will eventually be limited by spin-flip scattering mechanisms in the base layer, which gives a lower limit to the minority electron current, and so limits the maximum possible MC values (see Chap. 4). If spin-flip scattering processes are ignored for MTTs with thick enough base layers, the bias voltage dependence of the MC should become weak. The fact that this is not observed experimentally suggests that the spin-mixing effect should be taken into account for MTTs with thick base layers, which is beyond the scope of the model presented in this chapter.

In contrast to MTTs with GaAs collectors, MTTs with Si collectors show a monotonic bias dependence of the MC. A large MC is initially observed when the bias voltage just exceeds the base/collector Schottky barrier height (~ 0.7 V). The MC then monotonically decreases with bias until the tunnel barrier breaks down.

3.3 Model

Hot electron transport across metal/semiconductor Schottky barriers has been widely studied using ballistic electron emission microscopy (BEEM) and many models have been developed to account for these experiments [57–59]. In these models, the transmission and reflection coefficients of the incident hot electrons at the

metal/semiconductor interface are evaluated quantum mechanically. The incident electron angular distribution and the semiconductor conduction band structure are often found to be important in order to properly account for the collector current. In the following, a simple model is presented to explain the observed bias dependence of the MC, which is similar to these BEEM models, but is extended to include spin-dependent electron inelastic scattering in the ferromagnetic base layer. In this model, the collector current is calculated using the following equation:

$$\begin{aligned}
I_{C,P(AP)} = & I_E \frac{1 + P_E}{2} e^{\frac{-t}{\lambda_{\uparrow(\downarrow)}}} \int_{\Phi_S}^{eV_{EB}} \int f_{\uparrow(\downarrow)}(E_E) D_{\uparrow(\downarrow)}(E_E, \vec{k}_{\parallel}) T(E_E, \vec{k}_{\parallel}) d\vec{k}_{\parallel} dE_E \\
& + I_E \frac{1 - P_E}{2} e^{\frac{-t}{\lambda_{\downarrow(\uparrow)}}} \int_{\Phi_S}^{eV_{EB}} \int f_{\downarrow(\uparrow)}(E_E) D_{\downarrow(\uparrow)}(E_E, \vec{k}_{\parallel}) T(E_E, \vec{k}_{\parallel}) d\vec{k}_{\parallel} dE_E \quad (3.1)
\end{aligned}$$

where I_E is the emitter current, P_E is the emitter spin polarization, t is the base layer thickness, $\lambda_{\uparrow(\downarrow)}$ is the spin-dependent attenuation length for the quasi-elastic majority (minority) electrons, E_E is the hot electron energy, $f_{\uparrow(\downarrow)}$ and $D_{\uparrow(\downarrow)}$ are the energy and angular distribution functions of the hot electrons at the base/collector interface, respectively, T is the electron transmission coefficient across the Schottky barrier, and \vec{k}_{\parallel} is the component of the electron wave vector that is parallel to the film planes.

Note that P_E and $\lambda_{\uparrow(\downarrow)}$ used in Eq. 3.1 are subtly different from those defined in Eq. 2.1. In Eq. 2.1, the collector electronic structure is not explicitly considered. Rather, the influence of the semiconductor conduction band structure on the collector current is included in the emitter spin polarization P_E , and $\lambda_{\uparrow(\downarrow)}$ characterizes the base layer thickness dependence of the collector current attenuation. In contrast, Eq. 3.1 explicitly takes into account the collector electronic structure effects by including the energy and angular distributions of the hot electrons and the calculated electron transmission coefficients $T(E_E, \vec{k}_{\parallel})$. P_E is a constant in these calculations and $\lambda_{\uparrow(\downarrow)}$ describes the attenuation of the quasi-elastic majority (minority) electron current in the base.

The angular distribution $D_{\uparrow(\downarrow)}$ is assumed to be a two-dimensional Gaussian distribution centered at $k_{\parallel} = 0$ with a width of $\sigma_{\uparrow(\downarrow)}$, where k_{\parallel} is the magnitude of \vec{k}_{\parallel} ,

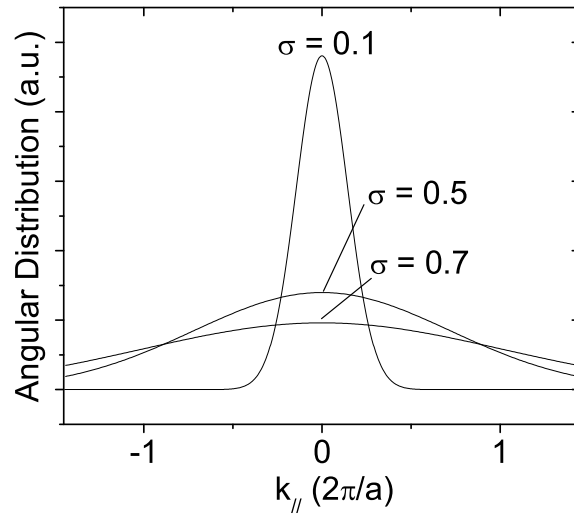


Fig. 3.2: Calculated hot electron angular distributions at the base/collector interface assuming Gaussian distributions with different widths.

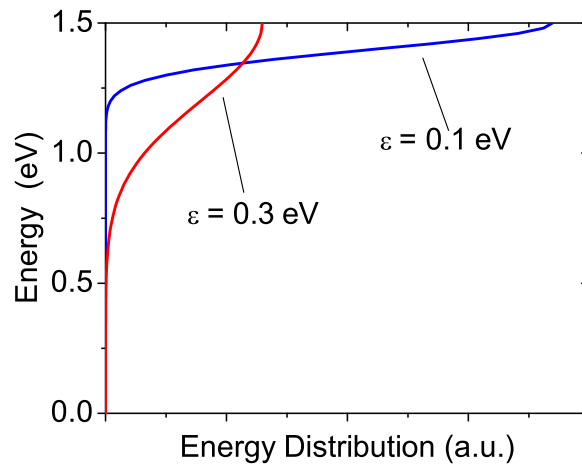


Fig. 3.3: Calculated hot electron energy distributions at the base/collector interface assuming Gaussian distributions with different widths at a bias voltage $V_{EB} = 1.5$ V.

and σ is a fraction of k_B , the maximum hot electron wave vector in the base layer:

$$k_B = \sqrt{\frac{2m_B(V_{EB} + E_F)}{\hbar^2}} \quad (3.2)$$

where m_B is the electron mass in the base, and E_F is the Fermi energy. The energy distribution $f_{\uparrow(\downarrow)}$ is assumed to be a half-Gaussian centered at eV_{EB} with a width of $\varepsilon_{\uparrow(\downarrow)}$. The hot electron angular and energy distributions are illustrated in Fig. 3.2 and Fig. 3.3 for different widths.

The transmission coefficient $T(E_E, \vec{k}_{\parallel})$ is calculated assuming continuity of the electron wave function and average electron current at the base/collector interface [57]. Eq. 5 and 6 in Ref. [59] are used in the model calculations.

In the MTT the spin-polarized hot electrons that are injected from the emitter into the base initially have very narrow energy and angular distributions. This is because that the tunneling process is highly sensitive to the height and thickness of the tunnel barrier. Therefore electrons are selectively injected with energies close to the emitter Fermi level and with small parallel wave vector components. As these hot electrons traverse the base layer, they experience inelastic scattering and lose energy. As a consequence, the energy distribution of the hot electrons broadens across the base layer. Since the scattering rate is typically lower for the majority electrons than for the minority electrons, the minority electrons are more likely to lose energy and thus have a broader energy distribution. Additional electron scattering occurs at the base/collector interface, after which a fraction of the incident electrons are collected by the semiconductor collector. This interface scattering could broaden the angular distribution of the hot electrons.

The GaAs conduction band has its lowest energy band at the center of the Brillouin zone (Γ conduction valley). At energies ~ 0.29 eV above the Γ point, there are eight conduction bands along the $\langle 111 \rangle$ axes (L conduction valleys) [60]. At an even higher energy, ~ 0.48 eV above the Γ point, there are six conduction bands along the $\langle 001 \rangle$ axes (X conduction valleys) [60]. When the bias voltage exceeds the Schottky barrier height by just a small margin, the hot electron current is collected

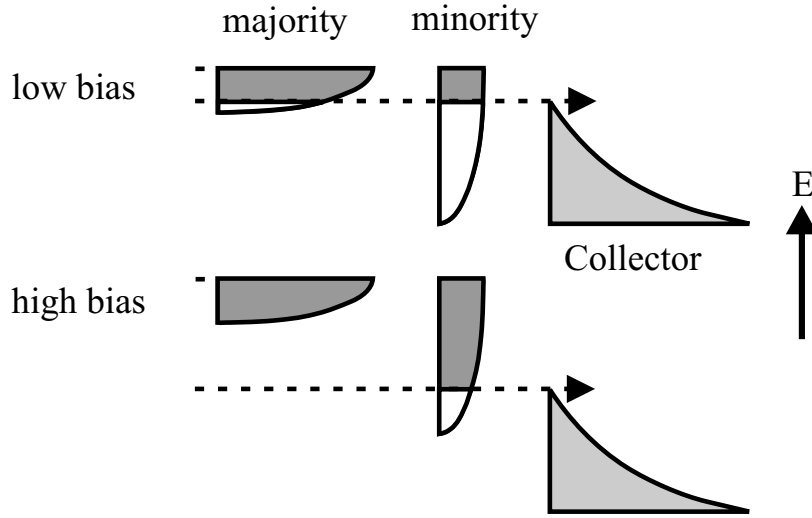


Fig. 3.4: Schematic drawing of the majority and minority electron collection at low and high bias voltages. The dark areas indicate electrons that have enough energy to surmount the Schottky barrier. At a low bias voltage (upper half), most of the majority electrons, but only a small portion of the minority electrons have enough energy to surmount the Schottky barrier. At a high bias voltage (lower half), this asymmetry is reduced since a large portion of the minority electrons can also be collected.

through the central Γ conduction valley only. Because of their narrower energy distribution, a larger portion of the majority electrons is able to surmount the Schottky barrier and contributes to the collector current. On the other hand, a smaller portion of the minority electrons has enough energy to be collected. This is schematically illustrated in Fig. 3.4. The large spin asymmetry in hot electron collection results in a large MC value at low bias. At elevated bias voltages, increasingly more of the scattered minority electrons are able to surmount the Schottky barrier, which leads to a smaller MC value. If all the collector conduction bands open up at the same energy level, a monotonic decrease of the MC with bias is expected, as observed in MTTs with Si collectors. However, for GaAs, the L and X conduction valleys open up at higher energies than the Γ conduction valley. When these conduction valleys become available for hot electron injection, they initially favor the majority electron collection and thus tend to increase the MC. This gives rise to the observed non-monotonic bias voltage dependence of the MC for MTTs with GaAs collectors [Fig. 3.1(a)].

3.4 Discussion

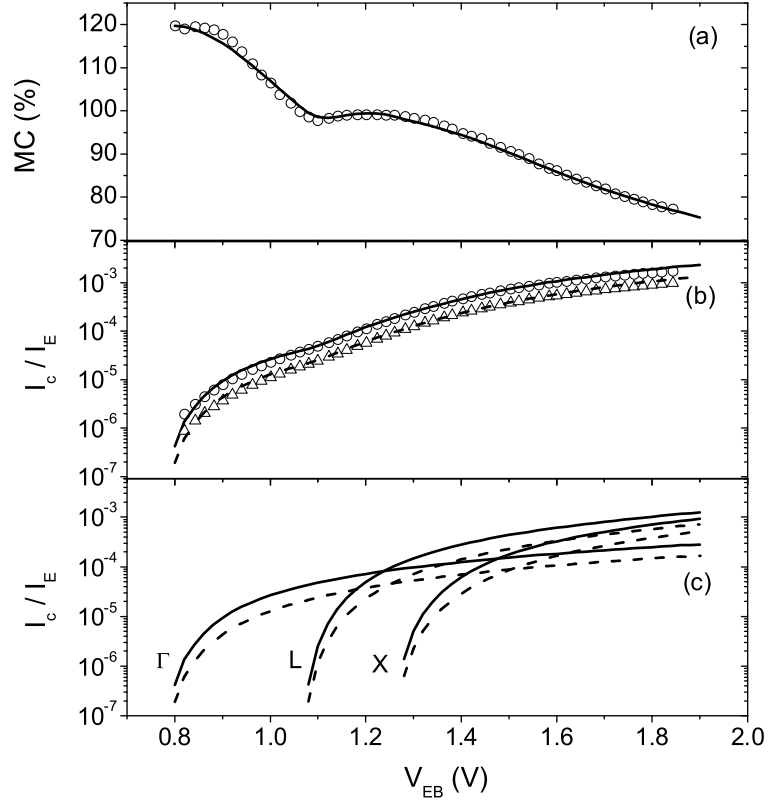


Fig. 3.5: The measured (symbols) and calculated (lines) bias voltage dependence of the MC (a) and I_C/I_E [(b) and (c)] for parallel (circles/solid lines) and anti-parallel (triangles/dashed lines) alignment of the emitter and base magnetic moments for the MTT of sample 1 in Table 3.1. (c) displays the calculated I_C/I_E for the Γ , L, and X conduction bands separately. The angular distribution is assumed to be broad and identical for the majority and minority electrons.

The discussion presented in this section will focus on sample 1 and 6 in Table 3.1. The main conclusions are applicable to all the samples, although the fitting parameters may vary from sample to sample.

The measured (open circles) and calculated (solid line) MCs are plotted in Fig. 3.5(a) for sample 1. The fitting parameters used in the calculations are:

$$\begin{aligned}\Phi_S &= 0.78 \text{ eV}, P_E = 50\%, E_F = 8.9 \text{ eV}, \lambda_{\uparrow} = 50 \text{ \AA}, \lambda_{\downarrow} = 20 \text{ \AA}, \\ \varepsilon_{\uparrow} &= 0.1 \text{ eV}, \varepsilon_{\downarrow} = 0.3 \text{ eV}, \sigma_{\uparrow} = \sigma_{\downarrow} = 0.5\end{aligned}$$

A free electron approximation is used to describe electrons in the metal base layer, while an energy-dependent effective mass model is used for electrons in the GaAs conduction bands, as given by the following equation:

$$m^*(E) = m^*(0)(1 + \beta E) \quad (3.3)$$

where $m^*(0)$ is the electron effective mass at the conduction band minima, β is the non-parabolicity parameter of the conduction bands, and E is the electron energy with respect to the bottom of the conduction band. $m^*(0)$ and β values for the Γ , L and X conduction bands are summarized in Table 3.2 [59], where m_0 is the free electron mass, l and t refer to the longitudinal and transverse electron effective masses, respectively.

conduction band	$m^*(0)/m_0$	β (eV ⁻¹)
Γ	0.067	0.69
L	1.9 (l), 0.075 (t)	0.65
X	1.3 (l), 0.23 (t)	0.5

Table 3.2: Electron effective masses of the GaAs Γ , L and X conduction bands.

In Fig. 3.5(b), the measured I_C/I_E data for parallel (open circles) and anti-parallel (open triangles) alignment of the emitter and base magnetic moments are plotted together with the calculated results (solid and dashed lines for parallel and anti-parallel alignment, respectively). The calculations agree very well with the experimental data. In Fig. 3.5(c), the contributions to the collector current from the Γ , L and X conduction band valleys are depicted separately. For bias voltages less than the L conduction

band threshold, all the electrons are injected into the Γ conduction valley and the MC decreases with the bias voltage as predicted by the model. At $V_{EB} \approx 1.1$ V, the L conduction valleys become available for hot electron collection. Initially, more majority electrons are collected than minority electrons, which results in an increase in the MC. The longitudinal electron effective mass of the L conduction valleys is much larger than the effective mass of the Γ conduction valley. Consequently, the number of available energy states in the L conduction valleys increases very rapidly with bias voltage, giving rise to a significant contribution to the collector current from the L conduction valleys [Fig. 3.5(c)]. As the bias voltage further increases, more minority electrons can also be collected by the L conduction valleys, and the MC decreases again. The energy states in the X conduction valleys become available for hot electron injection at $V_{EB} \approx 1.3$ V. However, the current collected through the Γ and L conduction valleys is already very large and, hence, no significant change in the MC or I_C/I_E results by the small additional current collected through the X conduction valleys.

For the calculations shown in Fig. 3.5, a broad angular distribution is assumed for both the majority and minority electrons ($\sigma_{\uparrow} = \sigma_{\downarrow} = 0.5$). This is essential for reproducing the non-monotonic bias voltage dependence of the MC. As discussed above, the observed bias dependence of the MC is due to electron collection through the L conduction valleys at high bias. Since these valleys are located far away from the Brillouin zone center, a large parallel wave vector is required for the hot electrons to access them. If the incident electron angular distribution at the base/collector interface is narrow, very few electrons will be collected by the L conduction valleys and a monotonic decrease of the MC with bias is expected. This is clearly illustrated by the calculated results shown in Fig. 3.6(a), where the fitting parameters are the same as those used for Fig. 3.5 except that a much narrower angular distribution is assumed: $\sigma_{\uparrow} = \sigma_{\downarrow} = 0.1$. As shown in Fig. 3.6(c), the contribution to the collector current from the L conduction valley is too small to have an effect on the bias dependence of the MC. On the other hand, a large number of electrons can readily access the central Γ conduction band with a narrow angular distribution. The calculated I_C/I_E ratios at low bias voltages, when the electrons are injected into the Γ conduction valley only,

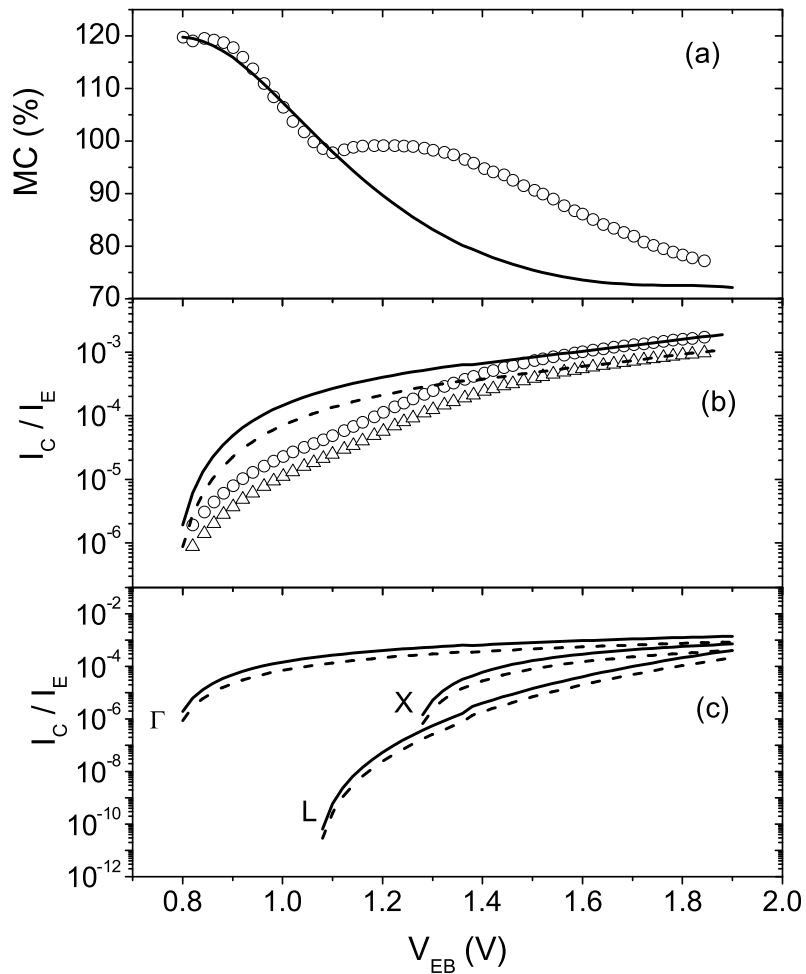


Fig. 3.6: Same as Fig. 3.5, but the angular distribution is assumed to be narrow and identical for the majority and minority electrons.

is therefore much larger than the experimental data [Fig. 3.6(b)].

In the previous calculations, it is assumed that the minority electrons have a broader energy distribution than the majority electrons. The spin-dependent broadening of the electron energy distribution can be rationalized by spin-dependent electron scattering in the ferromagnetic base layer. As discussed in Chap. 2, the majority

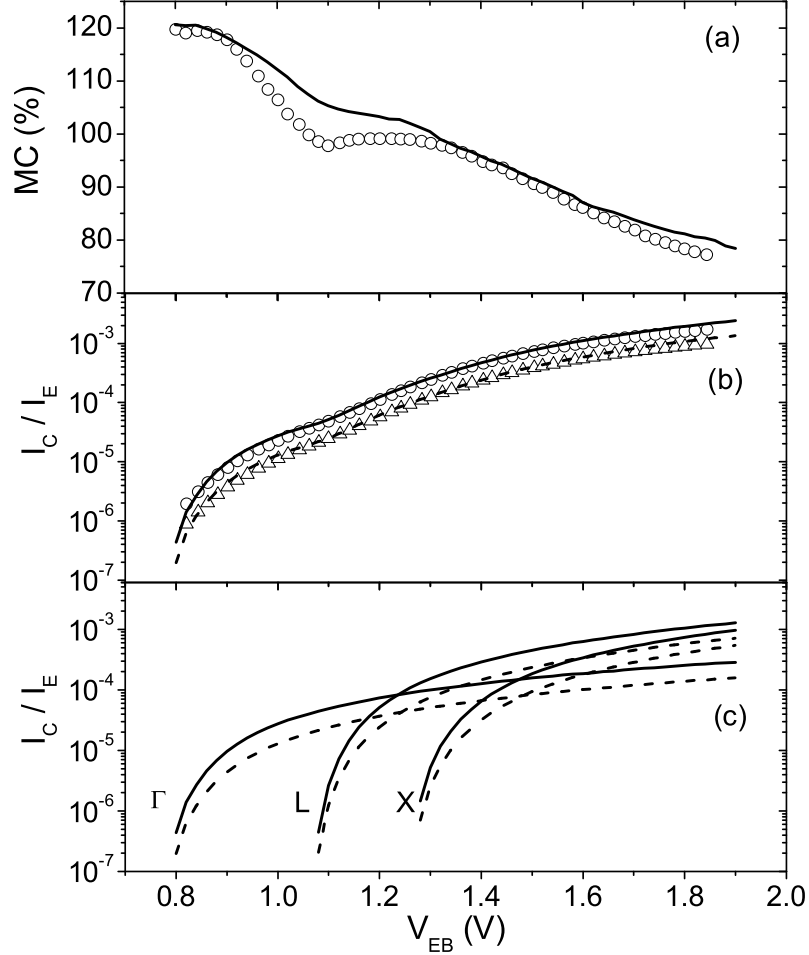


Fig. 3.7: Same as Fig. 3.5, but the angular distribution is assumed to be broader for the majority electrons than for the minority electrons.

electron d band in ferromagnetic $3d$ transition metals is fully or nearly fully occupied, whereas a portion of the minority electron d band is unoccupied. Scattering of the minority electrons into the empty d states above the Fermi level is efficient and is often held responsible for the difference between the majority and minority attenuation lengths. The minority electrons that are scattered into the empty d states excite electrons with either spin orientation from the occupied states below the Fermi level.

Due to the abundance of minority d states just below the Fermi level, the number of excited minority electrons will be significantly larger than the number of excited majority electrons. This scattering process plus others [38] thus contribute to the spin asymmetry in the electron energy distribution. In contrast to the spin-dependent energy distributions, the electron angular distribution is assumed to be identical for the majority and minority electrons. If the broadening of the angular distribution is due to spin-dependent electron scattering in the base layer, it might seem that the angular distribution is also broader for the minority electrons than for the majority electrons. The calculated results based on such an assumption are given in Fig. 3.7, where the fitting parameters are the same as those used for Fig. 3.5 except that $P_E = 46\%$, $\sigma_{\uparrow} = 0.5$ and $\sigma_{\downarrow} = 0.7$. With a broader angular distribution, the minority electrons can access the L conduction valleys more easily than the majority electrons. This partly compensates for the lower collection efficiency of the minority electrons due to their broader energy distribution. As a consequence, when the L conduction valleys open up for electron collection, the spin asymmetry in the electron collection efficiency is reduced, and the MC decreases monotonically with the bias voltage. A similarly broad angular distribution for the majority and minority electrons, which is necessary to interpret the experimental data, can be rationalized by efficient spin-independent electron scattering at the base/collector interface, which may be caused by metal/semiconductor alloying, residual oxide on the semiconductor surface, and interfacial defects. In BEEM studies, diffusive electron scattering at non-epitaxial metal/semiconductor interfaces is believed to broaden the hot electron angular distribution and has been proposed to explain similar BEEM currents for Au/Si(001) and Au/Si(111) systems [58]. Indeed, a strong electron scattering at the base/collector interface is observed in the base layer thickness dependent transport measurements of similar MTT devices, as discussed in Chap. 2.

The assumption of a spin-dependent hot electron energy distribution is important in order to account for the experimental data. Fig. 3.8 shows the calculated results assuming the same energy distribution for the majority and minority electrons. In addition, the majority and minority electrons are assumed to have a narrow and broad angular distribution, respectively. The fitting parameters in the calculations are the

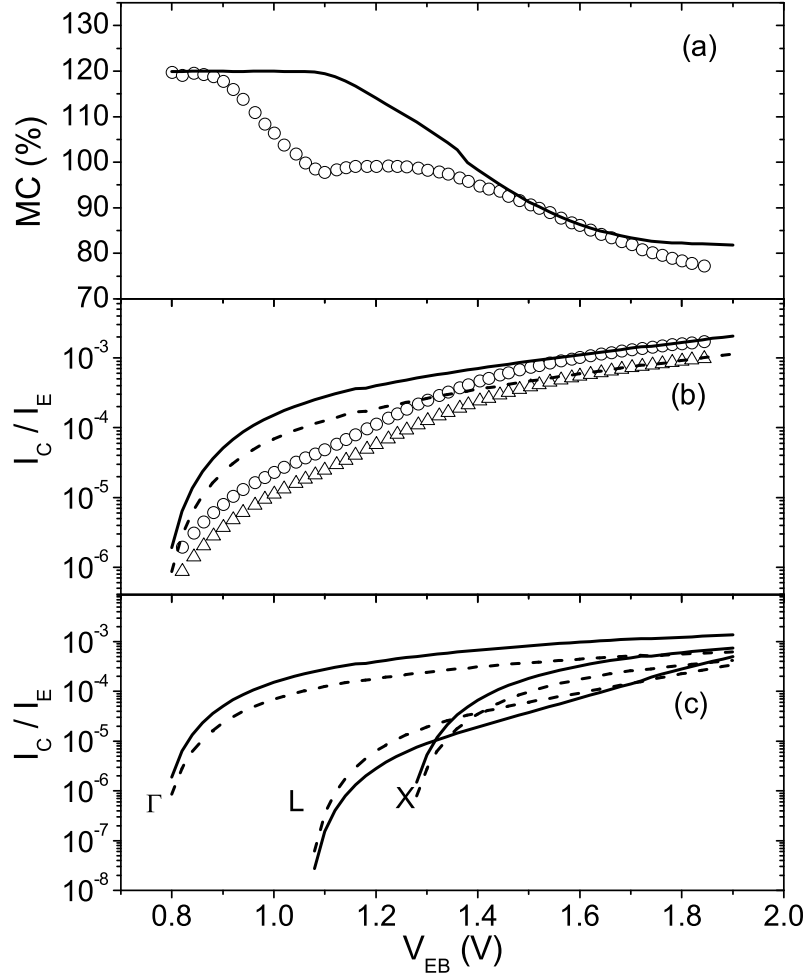


Fig. 3.8: Same as Fig. 3.5, but the energy distribution is assumed to be identical for the majority and minority electrons. The angular distribution is assumed to be narrow for the majority electrons and broad for the minority electrons.

same as those used for Fig. 3.5 except that $P_E = 39\%$, $\varepsilon_{\uparrow} = \varepsilon_{\downarrow} = 0.1$ eV, $\sigma_{\uparrow} = 0.1$, $\sigma_{\downarrow} = 0.5$. At low bias voltages, the MC stays approximately constant since the same energy distribution is assumed for the majority and minority electrons. When the L conduction valleys become available for electron injection at higher bias voltages, more

minority electrons are collected than majority electrons due to their broader angular distribution. As shown in Fig. 3.8(c), the current collected by the L conduction bands is larger in the anti-parallel alignment of the emitter and base magnetic moments. As a result, the MC decreases monotonically with bias voltage. On the other hand, if a broad angular distribution is assumed for the majority electrons and a narrow angular distribution is assumed for the minority electrons, the MC will become negative (not shown), which is opposite to what is observed in the experiments. Note that very similar bias voltage dependences of the MC are measured for MTTs with GaAs(001) and GaAs(111) collectors, although the projections of the conduction bands onto the interface plane are very different for the two substrate orientations. This is strong evidence that extensive diffusive scattering occurs at the base/collector interface and that the measured bias voltage dependence of the MC cannot be explained by different angular distributions for the majority and minority electrons.

In the model described in Sec. 3.3, the observed non-monotonic bias dependence of the MC is closely related to the GaAs conduction band structure. If the semiconductor collector has a single conduction band energy minimum, a monotonic variation of the MC with the bias voltage is expected. Si has six conduction valleys along the $\langle 001 \rangle$ axes and they all have the same energy minimum. Hence, measuring the bias dependence of the MC in an MTT with a Si collector provides a good test of the validity of the model. The experimental results are shown in Fig. 3.9 (symbols), and are consistent with the model prediction. The calculated results (lines) agree very well with the experimental data, where the following fitting parameters are used:

$$\begin{aligned} \Phi_S &= 0.72 \text{ eV}, P_E = 41.7\%, E_F = 8.9 \text{ eV}, \lambda_\uparrow = 50 \text{ \AA}, \lambda_\downarrow = 28 \text{ \AA}, \\ \varepsilon_\uparrow &= 0.08 \text{ eV}, \varepsilon_\downarrow = 0.26 \text{ eV}, \sigma_\uparrow = \sigma_\downarrow = 0.5 \end{aligned}$$

Similar to GaAs, energy-dependent effective masses are used in the calculations for electrons in the Si conduction bands [57]:

$$m_l^*(0) = 0.98 m_0, m_t^*(0) = 0.19 m_0, \beta = 0.5 \text{ eV}^{-1}$$

Mizushima *et al.* also measured a monotonic decrease of the MC with electron energy in the range 1 – 1.5 eV in an MTT with a Si collector [15]. It was proposed that

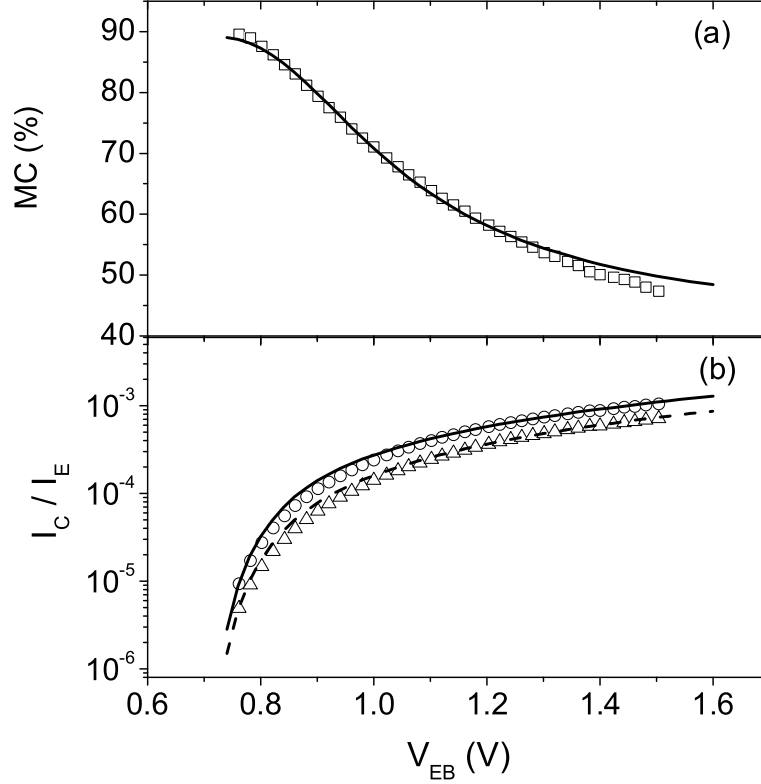


Fig. 3.9: The measured (symbols) and calculated (lines) bias voltage dependence of the MC (a) and I_C/I_E (b) in parallel (circles/solid line) and anti-parallel (triangles/dashed line) alignment of the emitter and base magnetic moments for MTTs of sample 6 in Table 3.1. The angular distribution is assumed to be broad and identical for the majority and minority electrons.

different angular distributions for the majority and minority electrons can account for this observation [61]. Such an explanation, however, will lead to a monotonic decrease of the MC in MTTs with both GaAs(001) and GaAs(111) collectors. The model in Sec. 3.3, on the other hand, explains the non-monotonic bias dependence of the MC in MTTs with GaAs collectors, as well as the monotonic decrease of the MC in MTTs with Si collectors. It reveals the important roles of the spin-dependent inelastic

electron scattering in the base layer and the semiconductor collector conduction band structure in hot electron transport in the MTTs.

Chapter 4

Magnetic Tunnel Transistors with a Spin-Valve Base

4.1 Introduction

In magnetic tunnel transistors with a single layer base, a spin-polarized electron current is first generated by spin-dependent tunneling from the emitter to the base. The polarization of the current is subsequently enhanced through spin-filtering in the base. The emitter tunneling spin polarization derives from the difference in the density of states and tunneling matrix elements of the majority and minority electron bands near the Fermi level. It is typically less than 50% when an Al_2O_3 tunnel barrier is used. In contrast, spin-filtering in the base can give rise to a much higher spin polarization when the base layer thickness exceeds the minority electron attenuation length. Therefore, the emitter spin polarization is often the limiting factor of the MC effect. The use of a ferromagnetic spin-valve base can overcome this problem. In this case, the initial electron spin polarization derives from spin-filtering in the first ferromagnetic layer and therefore can be more than 95%. As shown in Chap. 1, an MTT with a carefully designed spin-valve base exhibits a giant MC and a large output current. Such a device could be useful for a range of magneto-electronic applications. In this chapter, spin-dependent hot electron transport in MTTs with a spin-valve base is discussed [19,20]. In Sec. 4.2, the concept of transmission polarization is introduced

and used to explain the giant MC effect in MTTs with a spin-valve base. In Sec. 4.3, the transport properties of spin-valve base MTTs with Cu and Au spacer layers are compared. While the MC effects in these devices are very similar, the transfer ratio for the Cu spacer is almost ten times higher than that for the Au spacer. These results show the importance of optimizing the spacer layer material to improve the device properties. Current-in-plane GMR measurements were conducted on the spin-valve bases with Cu and Au spacer layers: the GMR effects differ by a factor of two. This suggests different origins of the spin-dependent electron transport in the GMR and MC measurements.

4.2 Giant Magneto-Current in Magnetic Tunnel Transistors with a Spin-Valve Base

The spin-valve base MTTs were formed by magnetron sputtering on GaAs(001) substrates at room temperature. The device structure was given by:

$$\text{GaAs(001)}/t \text{ Co}_{70}\text{Fe}_{30}/40 \text{ \AA} \text{ Cu}/t \text{ Ni}_{81}\text{Fe}_{19}/23 \text{ \AA} \text{ Al}_2\text{O}_3/300 \text{ \AA} \text{ Cu}$$

where t was the thickness of the ferromagnetic layers. The Al_2O_3 tunnel barrier was formed by plasma oxidizing a 18-Å-thick Al layer. The two ferromagnetic layers in the spin-valve base were chosen for optimized film growth and well separated magnetic switching fields. As shown in Fig. 1.3, giant collector current changes are obtained when the relative alignment of the CoFe and NiFe magnetic moments within the base layer is varied by a small external magnetic field. An MC value exceeding 3400% is observed at $V_{EB} = 0.8 \text{ V}$ for 50-Å-thick ferromagnetic layers. The collector current I_C increases with bias voltage. At $V_{EB} = 2.5 \text{ V}$, I_C reaches $\sim 7.5 \mu\text{A}$ while maintaining a high MC value of 670%.

The giant MC effect originates from spin-filtering in the ferromagnetic base layers. In ferromagnetic 3d transition metals and their alloys, hot electron scattering is much stronger for the minority electrons than for the majority electrons. Consequently, the unpolarized hot electron current, which is injected from the Cu emitter into the base, becomes spin-polarized after passing through the NiFe layer. The reduction of the

hot electron current in the CoFe layer is highly sensitive to the relative alignment of the magnetic moments within the spin-valve base. The attenuation is smallest when the majority electrons (referenced to the NiFe layer) are scattered less in the CoFe layer than the minority electrons; that is, when the magnetic moment of the CoFe layer is oriented parallel to that of the NiFe layer.

The transmission polarization of a ferromagnetic layer, ignoring interface contributions, can be written as:

$$P_{Tran} = \frac{n_{\uparrow} - n_{\downarrow}}{n_{\uparrow} + n_{\downarrow}} = \frac{e^{-t/\lambda_{\uparrow}} - e^{-t/\lambda_{\downarrow}}}{e^{-t/\lambda_{\uparrow}} + e^{-t/\lambda_{\downarrow}}} \quad (4.1)$$

where $n_{\uparrow(\downarrow)}$ is the number of majority (minority) electrons after passing through the ferromagnetic layer, and $\lambda_{\uparrow(\downarrow)}$ is the spin-dependent electron attenuation length. This expression does not consider the spin-dependence of interface scattering which is very small at the Cu interfaces. Scattering at the CoFe/GaAs interface, while significant, is largely spin-independent [22, 29]. The MC of a spin-valve base MTT can be written in terms of the effective transmission polarization of the two ferromagnetic layers, namely,

$$MC = 2P_1P_2/(1 - P_1P_2) \quad (4.2)$$

where P_1 and P_2 denote the polarization of the first and second ferromagnetic layer, respectively. Eq. 4.2 is equivalent to Julliere's formula [7] for calculating tunneling magnetoresistance of magnetic tunnel junctions using the tunneling spin polarization of the two ferromagnetic electrodes. The tunneling spin polarization of ferromagnetic 3d transition metal alloys is typically 40 – 50% when an Al_2O_3 tunnel barrier is used [21], which, according to Julliere's formula, limits the TMR value to about 50%. The transmission polarization of a ferromagnetic layer, on the other hand, can be controlled by varying the film thickness. It can readily reach 90 – 95% for ferromagnetic layer thickness larger than $\sim 30 \text{ \AA}$ (Fig. 4.1). Thus, the MC of an MTT with a spin-valve base is much larger than the TMR of an MTJ. In the case of a single layer base MTT, while the emitter spin polarization is due to tunneling giving rise to a polarization of $\sim 45\%$, spin-filtering in the base can result in a transmission polarization of more than 95%. As a consequence, the MC value is on the order of

100%. The comparison of the TMR for an MTJ and the MC for single layer and spin-valve base MTTs is summarized in Table 4.1.

device	P_1	P_2	MC or TMR
MTJ	45%	45%	51%
single layer base MTT	45%	95%	149%
spin-valve base MTT	95%	95%	1850%

Table 4.1: Comparison of TMR of an MTJ and MC of single layer and spin-valve base MTTs.

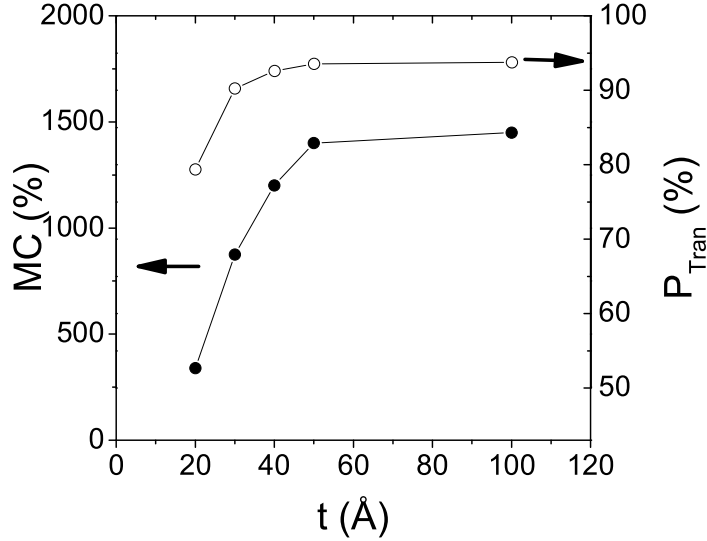


Fig. 4.1: MC (solid circles) and transmission polarization (open circles) as a function of the ferromagnetic layer thickness at $V_{EB} = 1.5$ V.

In Fig. 4.1, the MC and the transmission polarization P_{Tran} are plotted as a function of the ferromagnetic layer thickness at $V_{EB} = 1.5$ V, where P_{Tran} is calculated from $P_{Tran} = \sqrt{MC/(2 + MC)}$. The transmission polarization and, consequently, the

MC saturate at large ferromagnetic layer thicknesses, which indicates that P_{Tran} is limited by a small amount of spin-mixing in the MTT device. As a result, P_{Tran} is less than 100% even for very thick ferromagnetic layers. Increasing the thickness of the ferromagnetic layers reduces the transfer ratio, so a compromise between maximal MC and transfer ratio must be made.

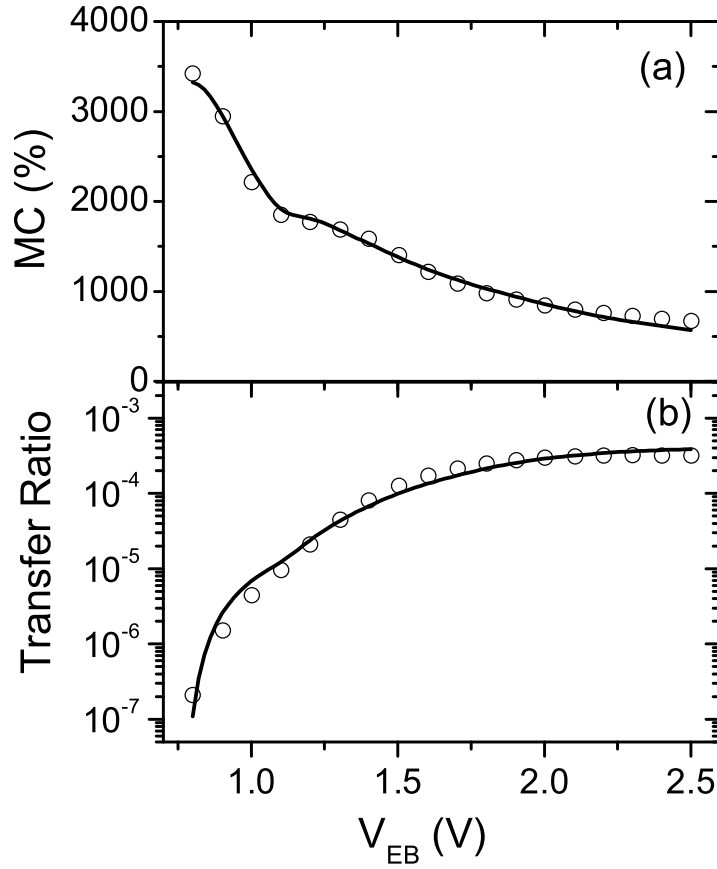


Fig. 4.2: Bias voltage dependence of the MC (a) and transfer ratio (b) for a spin-valve base MTT with $t = 50 \text{ \AA}$. The symbols and the solid lines are data and model calculations, respectively.

The bias voltage dependences of the MC and transfer ratio are depicted in Fig. 4.2 for an MTT with $t = 50 \text{ \AA}$. The decrease of the MC with V_{EB} is a result of different

majority and minority electron energy distributions caused by spin-dependent inelastic scattering in the ferromagnetic base layers, as discussed in Chap. 3. In contrast to the MC, the transfer ratio increases rapidly with V_{EB} at low bias voltages, which is due to an increasing number of available conduction band states in GaAs for electron collection at elevated energies. At high bias voltages, almost the entire GaAs Brillouin zone has available conduction band states for electron collection. Meanwhile, inelastic hot electron scattering rates in the base increases with bias. These lead to a saturation of the transfer ratio at high bias voltages. The same model that is discussed in Chap. 3 accounts very well for the bias dependences of the MC and transfer ratio in the spin-valve base MTT (Fig. 4.2).

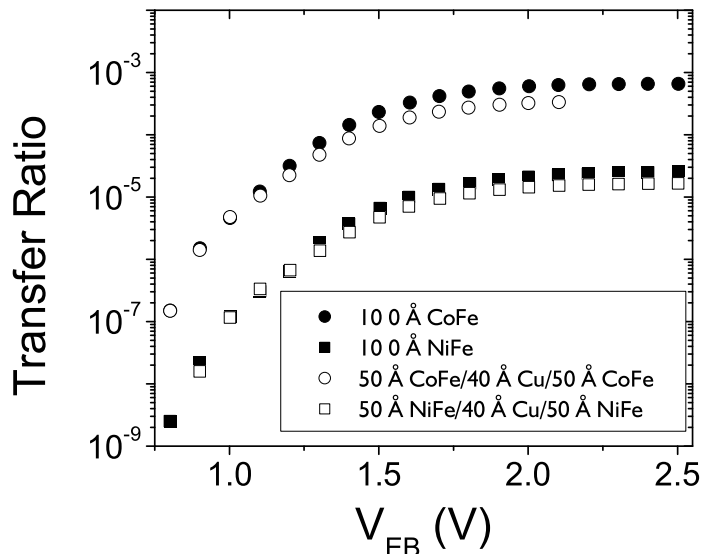


Fig. 4.3: Bias voltage dependence of the transfer ratio for MTTs with base layers consisting of 100 Å $\text{Co}_{70}\text{Fe}_{30}$ (solid circles), 100 Å $\text{Ni}_{81}\text{Fe}_{19}$ (solid squares), 50 Å $\text{Co}_{70}\text{Fe}_{30}/40$ Å Cu/50 Å $\text{Co}_{70}\text{Fe}_{30}$ (open circles), and 50 Å $\text{Ni}_{81}\text{Fe}_{19}/40$ Å Cu/50 Å $\text{Ni}_{81}\text{Fe}_{19}$ (open squares).

For efficient transport of hot electrons perpendicular to a spin-valve sandwich, Cu is the ideal spacer material. Noble metals, such as Cu and Au, have large electron attenuation lengths [62–64]. Therefore, bulk scattering in these metals will not

decrease the hot electron current even when the films are quite thick. CoFe, NiFe, and Cu can grow very well on each other, as found in studies of the giant magnetoresistance effect [6, 65]. Smooth interfaces between these layers are desirable for reducing electron current loss from interfacial scattering. In Fig. 4.3, the bias voltage dependence of the transfer ratio is measured for MTTs with base layer structures consisting of a 50 Å FM/40 Å Cu/50 Å FM spin-valve or a single 100-Å-thick FM layer, where FM is $\text{Co}_{70}\text{Fe}_{30}$ or $\text{Ni}_{81}\text{Fe}_{19}$. The almost identical transfer ratios for the spin-valve and single layer base MTTs indicate that the hot electron current attenuation in the 40-Å-thick Cu film and at the Cu/CoFe or NiFe/Cu interfaces is very small. The slightly lower transfer ratio for the spin-valve base MTTs at elevated bias voltages may be explained by a reduction of the electron attenuation length in the Cu spacer layer at high electron energies due to enhanced electron-electron interactions [37]. Compared to the Cu/FM interfaces, the amount of hot electron scattering at the base/collector interface is much larger. Such interface scattering limits the output current of the MTT and should therefore be minimized by appropriate material selection and growth optimization. The material dependence of the base/collector interface scattering is shown by measurements of MTTs with NiFe and CoFe layers grown on GaAs collectors (Fig. 4.3). The large difference in the transfer ratio can be rationalized by different interface alloying behavior during the initial film growth stages, as discussed in Chap. 2.

4.3 Comparison of Spin-Valve Base Magnetic Tunnel Transistors Containing Cu and Au Spacer Layers

Spin-dependent electron transport in magneto-electronic devices, such as the spin-valves and the MTJs, are extremely sensitive to the properties of the interfaces within the thin film multilayered structures. For example, spin-dependent electron transmission and reflection at the ferromagnetic/non-magnetic metal interfaces of a spin-valve drastically influences its GMR values [66–68]. Similarly, the TMR of an MTJ depends

critically on the interfaces between the ferromagnetic electrodes and the tunnel barrier [69, 70]. In this section, it is shown that in MTTs with a spin-valve base, the interfaces between the ferromagnetic layers and the spacer layer play an important role in the transport of the hot electron current.

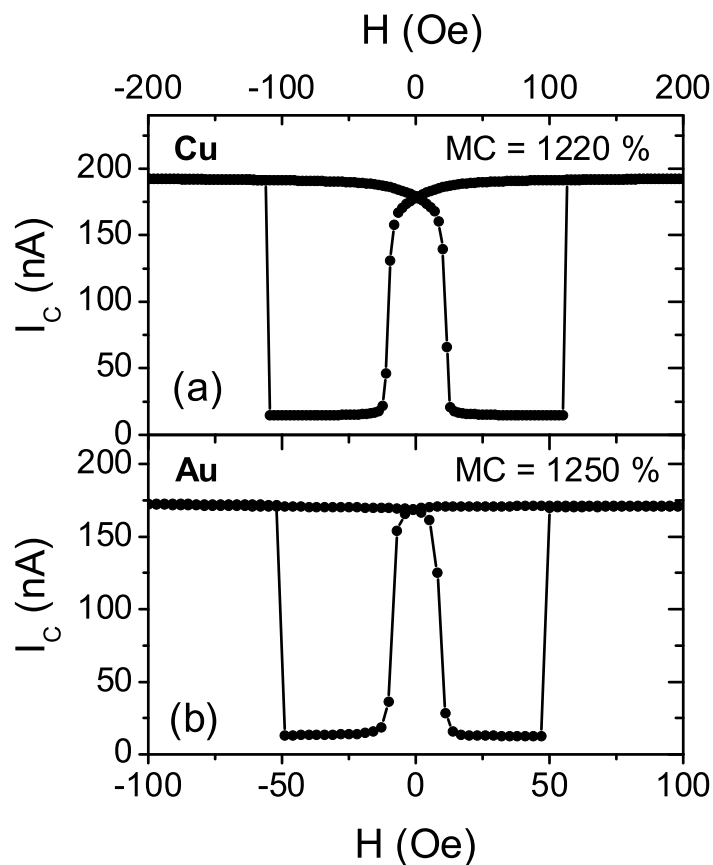


Fig. 4.4: Collector current as a function of the magnetic field for spin-valve base MTTs with Cu (a) and Au (b) spacer layers at $V_{EB} = 1.6$ V.

MTTs with both Cu and Au spacer layers were fabricated with otherwise identical structures as given in Sec. 4.2 ($t = 50$ Å). The magnetic field dependence of the collector current for these MTTs is plotted in Fig. 4.4. A giant MC of more than

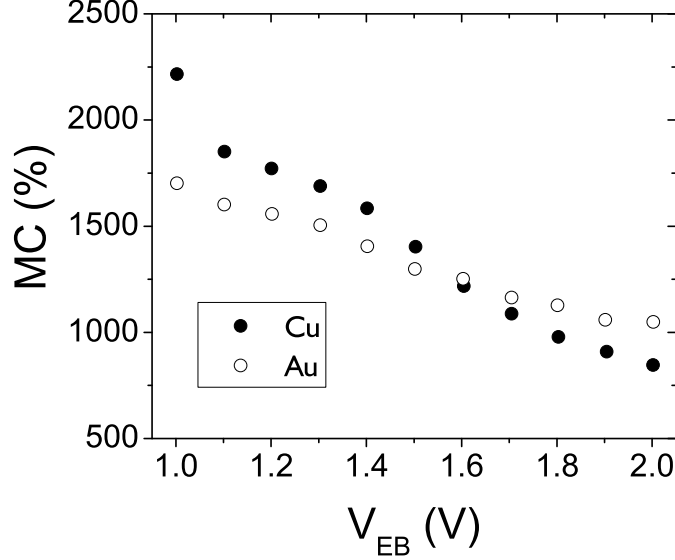


Fig. 4.5: Bias voltage dependence of the MC for spin-valve base MTTs with Cu (solid circles) and Au (open circles).

1200% is observed at $V_{EB} = 1.6$ V for both MTTs. The different switching fields of the CoFe layer (~ 120 Oe for Cu and ~ 50 Oe for Au) are presumably due to variations in the Cu/CoFe and Au/CoFe interface anisotropy. Fig. 4.5 shows the bias voltage dependences of the MC for MTTs with Cu and Au spacer layers, which are quite similar in the electron energy range of 1 – 2 eV.

An important parameter of the MTT device is the transfer ratio, $I_{C,P}/I_E$, which can be written as:

$$\begin{aligned}
 I_{C,P}/I_E &= e^{-t_{NiFe}/\lambda_{NiFe}^\uparrow} T_{NiFe/S}^\uparrow e^{-t_S/\lambda_S^\uparrow} T_{S/CoFe}^\uparrow e^{-t_{CoFe}/\lambda_{CoFe}^\uparrow} T_{CoFe/GaAs}^\uparrow \\
 &+ e^{-t_{NiFe}/\lambda_{NiFe}^\downarrow} T_{NiFe/S}^\downarrow e^{-t_S/\lambda_S^\downarrow} T_{S/CoFe}^\downarrow e^{-t_{CoFe}/\lambda_{CoFe}^\downarrow} T_{CoFe/GaAs}^\downarrow \quad (4.3)
 \end{aligned}$$

where \uparrow and \downarrow refer to the majority and minority electrons, respectively, S refers to the spacer layer, λ is the hot electron attenuation length, t is the ferromagnetic layer thickness, and T is the interface transmission coefficient.

Fig. 4.6 compares the transfer ratio of MTTs with Cu and Au spacer layers. In

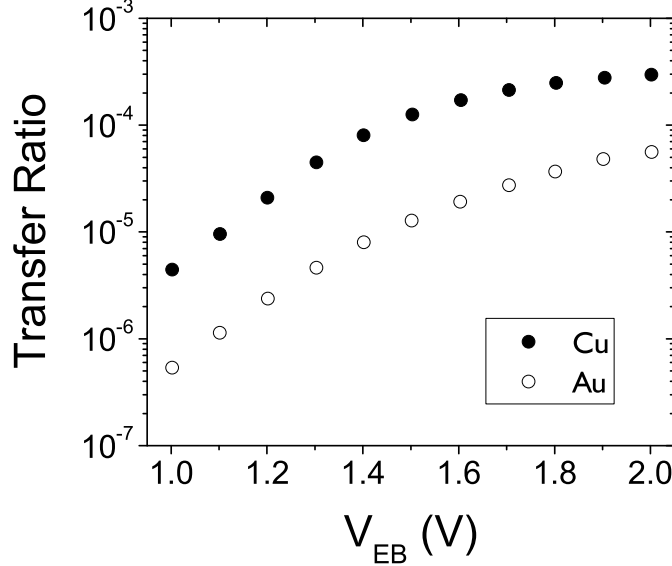


Fig. 4.6: Bias voltage dependence of the transfer ratio for spin-valve base MTTs with Cu (solid circles) and Au (open circles) spacer layers.

contrast with the MC, the transfer ratio depends strongly on the spacer layer material: it is about ten times smaller for Au than for Cu. Since previous measurements of hot electron attenuation lengths in Cu and Au show that they are much larger than the spacer layer thicknesses used here [19, 62–64], the large difference in the transfer ratio can be attributed to hot electron scattering at the interfaces between the ferromagnetic and spacer layers. As shown in Sec. 4.2, the amount of hot electron current loss at the CoFe/Cu and NiFe/Cu interfaces is negligibly small; that is, $T_{NiFe/Cu} \approx T_{Cu/CoFe} \approx 1$. By contrast, the hot electron transmission at FM/Au interfaces is much less efficient. From the data in Fig. 4.6, $T_{NiFe/Au} \times T_{Au/CoFe} \approx 0.1$ is obtained over the experimental energy range.

For the MTT device, it is reasonable to assume that the majority hot electrons traverse the spin-valve base in the high velocity s - p states since the majority d band is completely filled. On the other hand, the minority d band in CoFe and NiFe crosses the Fermi level, but band structure calculations indicate that the upper edge of this

band is located in the lower part of the energy range of the MTT transport measurements [26, 71, 72]. Therefore, the minority hot electrons are also s - p like at high bias voltages. Hot electrons in the s - p band may be treated as free electrons. In such a free electron approximation, the interface transmission coefficients are calculated by projecting the free electron Fermi surfaces onto the interface Brillouin zone. Electrons with parallel wave vectors less than the Fermi wave vectors of the materials on either side of the interface can be readily transmitted. Since the hot electron transport is largely perpendicular to the spin-valve base layers in the MTT, the transmission coefficients are expected to be large for both the majority and minority electrons, irrespective of whether the spacer layer material is Cu or Au. The similar MC values that are obtained for spin-valve bases with Cu and Au spacer layers are consistent with this simple picture: hot electron scattering at the spacer layer interfaces does not depend on the spin states of the electrons and consequently the MC derives solely from spin-filtering in the CoFe and NiFe layers. Such a simple picture does not, however, explain the different transfer ratios for MTTs with Cu and Au spacer layers. Since hot electron attenuation lengths in Cu and Au are much larger than the spacer layer thickness, the smaller transfer ratio for the Au spacer layer can be attributed to strong spin-independent hot electron scattering at the NiFe/Au and Au/CoFe interfaces, which might originate from defects associated with the larger lattice mismatch between the ferromagnetic alloys and Au.

Current-in-plane GMR measurements were conducted at 77 K on the same spin-valve bases containing Cu and Au spacer layers. As shown in Fig. 4.7, the GMR effect is about two times larger for Cu than for Au, which is in agreement with the superior GMR values that are found in Co/Cu multilayers [6]. The different GMR values can be contrasted with the similar MC values measured for the two spin-valve bases. The electron transport in the GMR measurements takes place near the Fermi level. At this energy, the majority and minority electrons have strikingly different characters for both CoFe and NiFe. While the majority electrons are still largely transported in the high velocity s - p band, the minority electrons have mainly a d band character. This difference results in strong band structure effects and spin-dependent interface transmission and reflection coefficients [67]. The band structure difference between

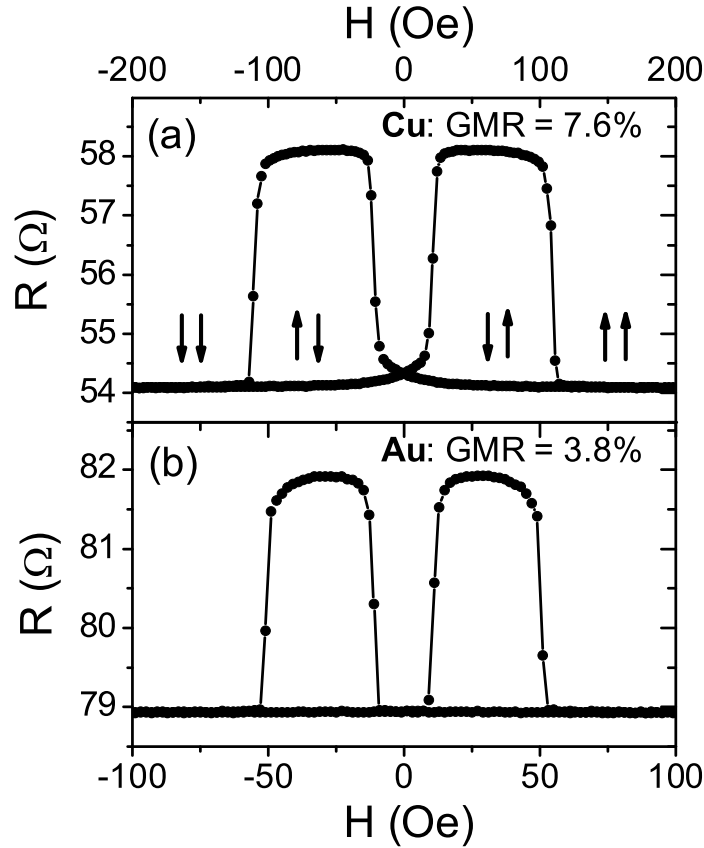


Fig. 4.7: Current-in-plane GMR measurements of the spin-valve bases with Cu (a) and Au (b) spacer layers.

Cu and Au, in combination with a larger number of defects at the CoFe/Au and NiFe/Au interfaces, lead to a significant difference in the GMR values. The MC and GMR measurements for spin-valves with different spacer layers is consistent with the picture that the MC effect is mostly due to bulk spin-dependent electron scattering in the ferromagnetic films while the GMR effect is largely determined by electron scattering at the interfaces between the ferromagnetic layers and the metallic spacer layer.

Chapter 5

Influence of Non-Magnetic Seed Layers on Magneto-Transport Properties of Magnetic Tunnel Transistors with a Si Collector

5.1 Introduction

In the previous chapters, the discussion was focused mainly on magnetic tunnel transistors with a GaAs collector. Since Si is the most widely used material in the semiconductor industry, it is of great interest to fabricate and study MTTs with a silicon collector. However, the integration of a Si collector into the MTT is not trivial. Ferromagnetic metals, such as Co, Fe, and their alloys, form silicides with Si [73–83], which can drastically degrade the performance of the MTT device. To overcome this problem, a non-magnetic seed layer is used to reduce the intermixing between the ferromagnetic layer and the Si substrate. By properly choosing the seed layer material and thickness, it is possible to improve the magnetic switching behavior of the ferromagnetic layers and increase the magnetic field sensitivity and output current of the MTT.

To investigate the influence of non-magnetic seed layers on the magneto-transport

properties of MTTs with a Si collector, a number of spin-valve base MTTs were fabricated with the following structure:

$$\text{Si(001)}/t \text{ seed layer}/t_0 \text{ Co}_{70}\text{Fe}_{30}/40 \text{ \AA} \text{ Cu}/50 \text{ \AA} \text{ Ni}_{81}\text{Fe}_{19}/25 \text{ \AA} \text{ Al}_2\text{O}_3/300 \text{ \AA} \text{ Cu}$$

where the seed layer materials were Cu, Au, Pt, Pd, Ti, or Ta, t and t_0 were seed layer and CoFe layer thicknesses, respectively. The Al_2O_3 tunnel barrier was formed by plasma oxidation of a sputtered thin Al film.

The transport experiments were conducted at 77 K. SQUID measurements were performed using the rectangular contact pads on the samples (see Sec. 1.2) at 77 K to characterize magnetic switching behavior of the ferromagnetic layers. The influence of non-magnetic seed layers on the switching fields of the ferromagnetic layers (Sec. 5.2), the MTT transfer ratio (Sec. 5.3) and MC (Sec. 5.4), and the magnetic anisotropy of the ferromagnetic layers (Sec. 5.5) are presented in separate sections. Secondary ion mass spectrometer (SIMS) analysis is used to gain insight into the silicide formation between the metals and the Si substrates (Sec. 5.6). The experimental results are further discussed in Sec. 5.7.

5.2 Magnetic Switching

Fig. 5.1(a) and (c) show the magnetic field dependence of the collector current for MTTs with a 50 \AA CoFe/40 \AA Cu/50 \AA NiFe and a 90 \AA CoFe/40 \AA Cu/50 \AA NiFe spin-valve base, respectively. Giant collector current changes are obtained when the relative alignment of the CoFe and NiFe magnetic moments is varied by an external magnetic field. The switching behavior of the base magnetic moments [Fig. 5.1(b) and (d)] is studied using the SQUID magnetometer. At large magnetic fields the CoFe and NiFe moments are aligned parallel with the field direction and the collector current is maximized. As the magnetic field decreases, the CoFe and NiFe moments rotate gradually away from the field direction, leading to a deviation from the parallel configuration. Consequently, a smaller collector current is observed. When the magnetic field is reversed, the NiFe moment switches first [Fig. 5.1(b) and (d)]. The orientation of the CoFe moment, on the other hand, continues to rotate

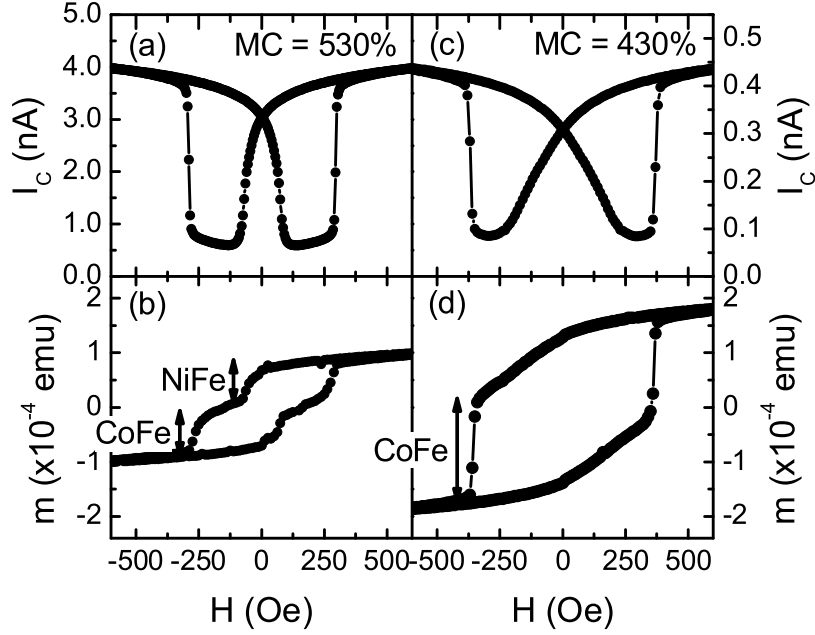


Fig. 5.1: Collector current and base magnetic moments as a function of the magnetic field for MTTs with a 50 Å $\text{Co}_{70}\text{Fe}_{30}$ /40 Å Cu/50 Å $\text{Ni}_{81}\text{Fe}_{19}$ [(a) and (b)] and a 90 Å $\text{Co}_{70}\text{Fe}_{30}$ /40 Å Cu/50 Å $\text{Ni}_{81}\text{Fe}_{19}$ [(c) and (d)] spin-valve base. The transport measurements were taken at $V_{EB} = 1.0$ V.

gradually up to about 270 Oe and 390 Oe for 50-Å-thick and 90-Å-thick CoFe layers, respectively, before it abruptly switches into the direction of the magnetic field. The collector current is minimized when the angle between the CoFe and NiFe magnetic moments is the largest. Because of the gradual switching of the CoFe and NiFe moments, a fully anti-parallel configuration is not achieved in these MTTs. However, giant magneto-currents of 530% and 430% are still obtained. Here the magneto-current is defined as:

$$MC = \frac{I_{C,max} - I_{C,min}}{I_{C,min}} \quad (5.1)$$

where $I_{C,max}$ and $I_{C,min}$ are the maximum and minimum collector current, respectively.

The SQUID measurement in Fig. 5.1(b) reveals that the magnetic moment of the CoFe layer is similar to that of the NiFe layer. Since these layers have the same nominal thickness, and, since CoFe has a considerably larger magnetic moment than NiFe [84], this suggests the formation of a silicide layer at the CoFe/Si(001) interface, which has a drastically reduced moment or is even non-magnetic. The CoFe film on top of the silicide layer likely consists of grains with different crystallographic orientations (also see Sec. 5.5). The magnetic switching behavior of this multi-crystalline CoFe film is determined by the nature of the grain growth and the interactions between individual grains. It will depend on parameters such as the grain size, the exchange length, and the domain wall width. Previous work has shown that the grain size of a 50-Å-thick $\text{Co}_{50}\text{Fe}_{50}$ film deposited on Si(001) is small in comparison with the exchange length and domain wall width, giving rise to a gradual reversal of the magnetic moment [83]. In the same study, both the grain size and switching field of the $\text{Co}_{50}\text{Fe}_{50}$ film were found to increase with its thickness. These results are consistent with the transport and SQUID measurements shown in Fig. 5.1.

The use of a non-magnetic seed layer to separate the CoFe layer from the Si substrate may limit CoFe-silicide formation and, therefore, could have a significant influence on the growth of the CoFe/Cu/NiFe spin-valve base, and hence its magnetic switching behavior. Fig. 5.2 shows the magnetic field dependence of the collector current for MTTs grown on 20-Å-thick non-magnetic seed layers. The insertion of a thin Cu or Au seed layer results in abrupt switching of the base magnetic moments at much smaller magnetic fields than those found for the spin-valve without a seed layer. For the Cu seed layer, the CoFe and NiFe switching fields are well separated, giving rise to a nearly anti-parallel alignment of the base magnetic moments at about 25 Oe and consequently a huge MC effect. For example, an MC value of 930% was measured at $V_{EB} = 1.0$ V, which, in combination with the abrupt magnetic switching behavior, results in a magnetic field sensitivity more than an order of magnitude larger than that of magnetic multilayers or magnetic tunnel junctions. Moreover, the CoFe layer now has a smaller switching field than the NiFe layer with the Cu seed layer. Fig. 5.3(b) shows the SQUID data for an MTT with a 20 Å Cu/80 Å CoFe/40 Å Cu/50 Å NiFe spin-valve base. The CoFe moment, which is larger than the NiFe moment, switches

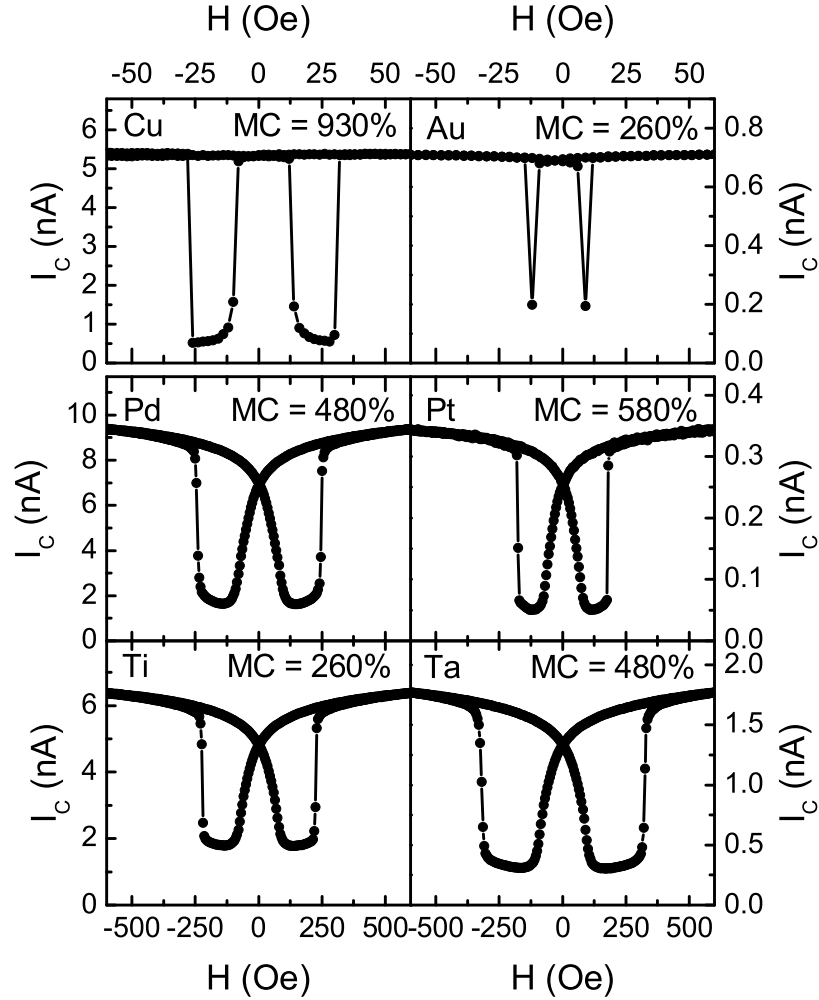


Fig. 5.2: Collector current as a function of the magnetic field for spin-valve MTTs with 20-Å-thick Cu, Au, Pd, Pt, Ti, and Ta seed layers at $V_{EB} = 1.0$ V.

at about 10 Oe, while the NiFe moment retains the same orientation up to about 25 Oe. This switching behavior is opposite to that of a spin-valve base without a seed layer.

The CoFe and NiFe switching fields are similar for the MTT with a 20-Å-thick Au seed layer (Fig. 5.2). Therefore, the anti-parallel configuration is never achieved and only a small MC effect is obtained. For a 10-Å-thick Au seed layer, however,

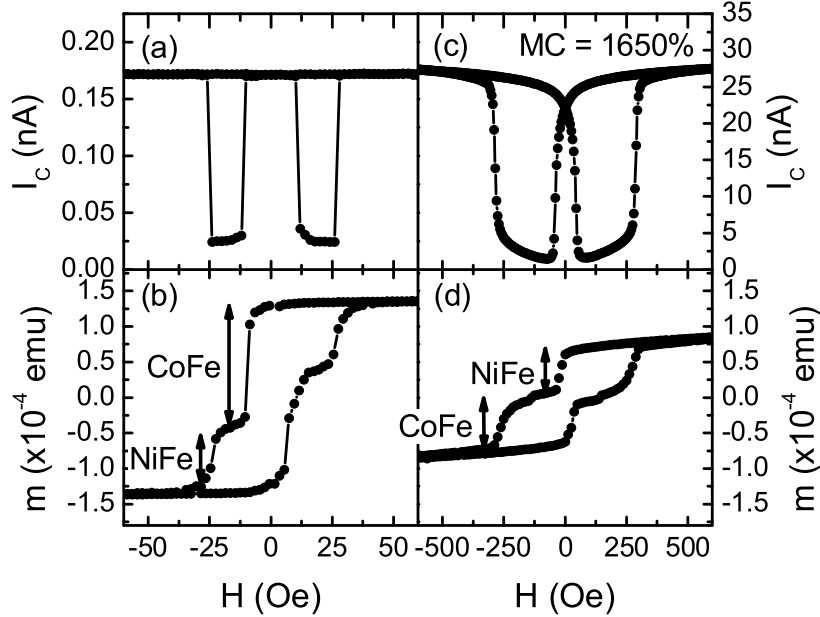


Fig. 5.3: Collector current and base magnetic moments as a function of the magnetic field for MTTs with a 20 Å Cu/80 Å Co₇₀Fe₃₀/40 Å Cu/50 Å Ni₈₁Fe₁₉ [(a) and (b)] and a 10 Å Au/50 Å Co₇₀Fe₃₀/40 Å Cu/50 Å Ni₈₁Fe₁₉ [(c) and (d)] spin-valve base. The transport measurements were taken at $V_{EB} = 1.0$ V.

the switching fields of the CoFe and NiFe moments become well separated and a giant MC effect is observed. Fig. 5.3(c) and (d) plot the collector current and base magnetic moments as a function of the magnetic field for an MTT with a 10 Å Au/50 Å CoFe/40 Å Cu/50 Å NiFe spin-valve base. The CoFe switching field is large and resembles that of the MTT without a seed layer. On the other hand, the NiFe moment switches more abruptly, giving rise to a nearly anti-parallel alignment of the base magnetic moments at about 60 Oe. The measured MC value is 1650% at $V_{EB} = 1.0$ V, which is considerably larger than that of an MTT without a seed layer.

The use of 20-Å-thick Pd, Pt, Ti, and Ta seed layers does not drastically alter the switching behavior of the spin-valve base magnetic moments. For Pt, Pd, and Ta seed layers, the MC values are comparable to that of MTTs without a seed layer. For

the Ti seed layer, the MC is actually reduced to 260% at $V_{EB} = 1.0$ V.

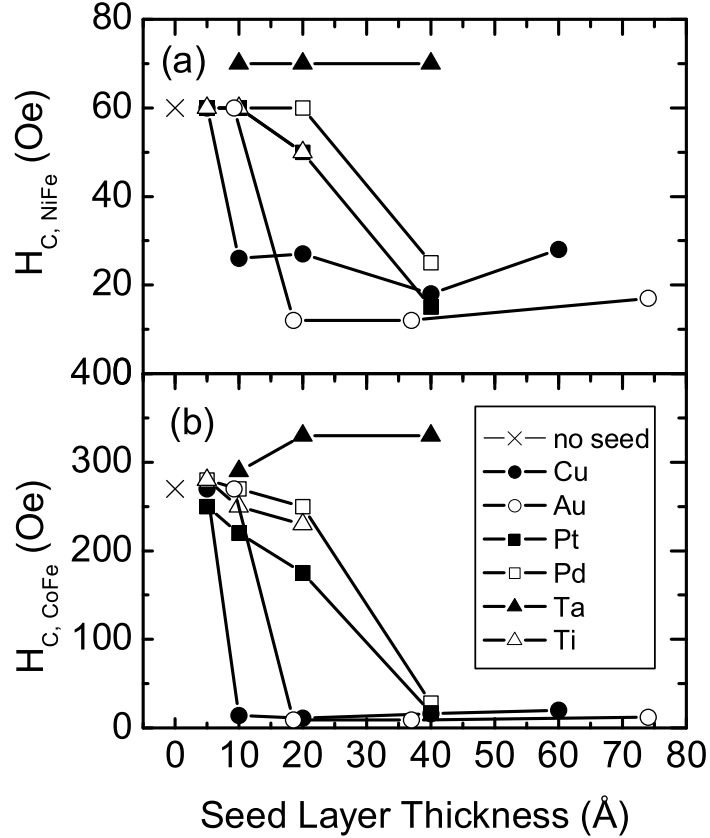


Fig. 5.4: NiFe (a) and CoFe (b) switching fields of a 50 Å $Co_{70}Fe_{30}$ /40 Å Cu/50 Å $Ni_{81}Fe_{19}$ spin-valve base as a function of the seed layer material and thickness.

Fig. 5.4 summarizes the NiFe and CoFe switching fields in a 50 Å $Co_{70}Fe_{30}$ /40 Å Cu/50 Å $Ni_{81}Fe_{19}$ spin-valve base grown on different seed layers. At small seed layer thicknesses (≤ 5 Å), the switching fields are very similar for all seed layer materials and do not substantially deviate from those of a spin-valve base without a seed layer. A drastic change occurs at a critical seed layer thickness of about 7.5 Å for Cu, 15 Å for Au, and 30 Å for Pt and Pd. Above these thicknesses, the CoFe switching field

decreases rapidly from ~ 270 Oe to ~ 15 Oe. In addition, the switching becomes much more abrupt. A similar but less dramatic change in the NiFe switching behavior is observed at about the same seed layer thickness. The changes in the CoFe and NiFe switching fields are not always beneficial. In some cases the switching fields are no longer separable and the MC effect is greatly reduced. Therefore, it is very important to carefully choose the seed layer material and film thickness in order to realize large MC effects. For Ta and Ti seed layers, the switching fields do not change significantly up to seed layer thicknesses of 40 \AA and 20 \AA , respectively. The tunnel barriers that are formed on top of spin-valves with Ta and Ti seed layers exhibit a small breakdown voltage (this is especially true for thick Ta and Ti seed layers). As a result, hot electron transport in these MTTs is limited to small emitter/base bias voltages, which is not desirable for device operations.

5.3 Transfer Ratio

Fig. 5.5 shows the transfer ratio at $V_{EB} = 1.0$ V for MTTs with a 50 \AA CoFe/ 40 \AA Cu/ 50 \AA NiFe spin-valve base grown on different seed layers. The data were measured in a magnetic field large enough to align the base magnetic moments to be parallel and normalized to the transfer ratio of an MTT without a seed layer (5×10^{-5} at $V_{EB} = 1.0$ V). The use of Cu and Au seed layers increases the transfer ratio, whereas the other seed layer materials are less beneficial or even detrimental. The variation of the transfer ratio with the seed layer depends on many parameters, such as the hot electron attenuation length in the metal and silicide layers, the thickness of these layers, and the Schottky barrier height (ϕ_S) between the seed layer and the Si collector.

The influence of the Schottky barrier height on the transfer ratio is related to the number of available conduction band states at a given bias voltage. If the Schottky barrier height is increased by the seed layer, the transfer ratio will be lowered and vice versa. This is most clearly illustrated in Fig. 5.6, where the bias dependence of the transfer ratio is plotted for MTTs with a 20 \AA seed layer (Cu or Pt)/ 50 \AA CoFe/ 40 \AA Cu/ 50 \AA NiFe spin-valve base. The onset bias voltage for hot electron

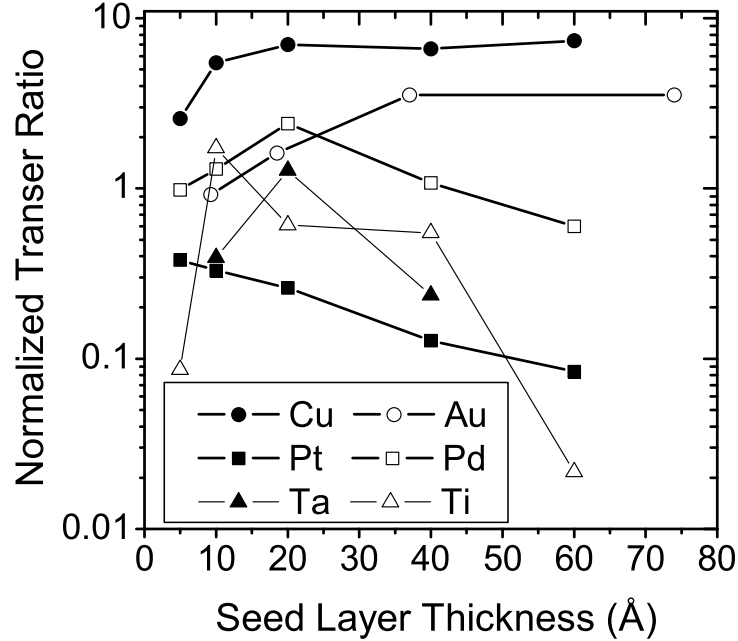


Fig. 5.5: Normalized transfer ratio as a function of the seed layer material and thickness at $V_{EB} = 1.0$ V.

collection by the Si(001) collector is very different for the two seed layers, indicating distinct Schottky barrier heights for Pt/Si and Cu/Si. The inset of Fig. 5.6 shows the magnetic field dependence of the collector current for the MTT with a Pt seed layer at $V_{EB} = 0.84$ V and 0.88 V. At $V_{EB} = 0.84$ V, the bias voltage is smaller than the Schottky barrier height and the collector current is dominated by the Schottky barrier leakage current. At $V_{EB} = 0.88$ V, when the bias voltage just exceeds the Schottky barrier height, hot electron collection is evident from the magnetic field dependence of the collector current. Such measurements give a Pt/Si Schottky barrier height of 0.85 ± 0.01 eV. Similarly, the Cu/Si Schottky barrier height is determined to be 0.65 ± 0.01 eV. The Schottky barrier heights for other metal/Si(001) interfaces can be measured in the same way and the results are summarized in Table 5.1. These barrier heights agree well with those given in the literature [85].

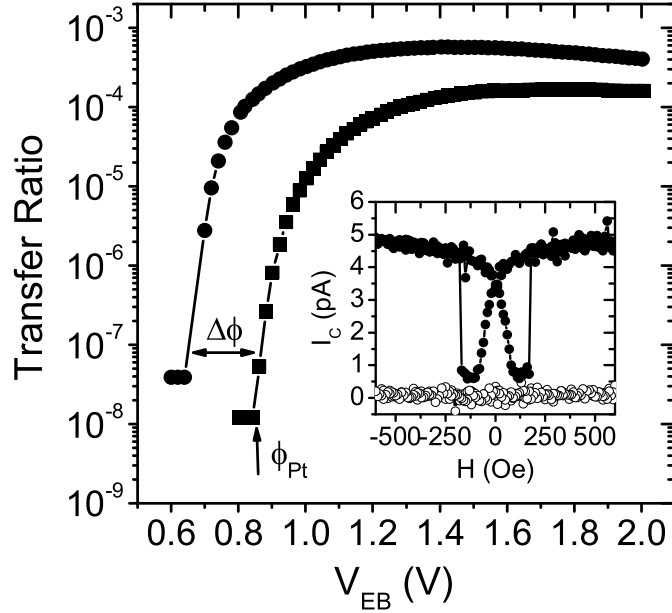


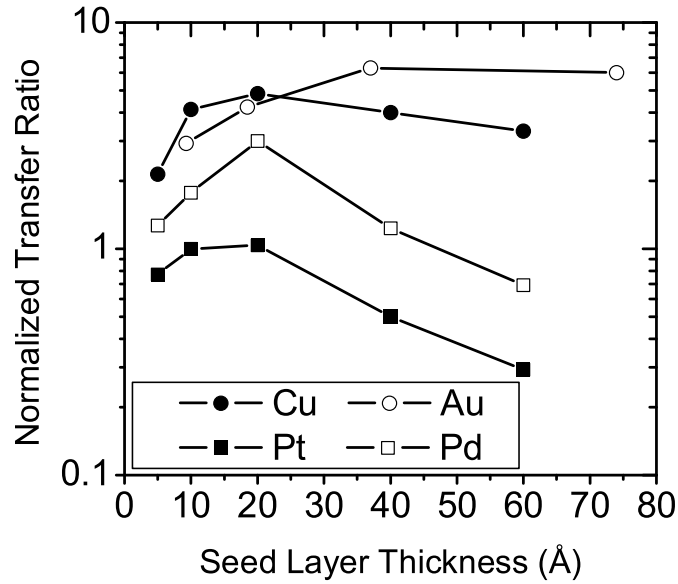
Fig. 5.6: Bias voltage dependence of the transfer ratio for MTTs with a 20 Å Cu/50 Å Co₇₀Fe₃₀/40 Å Cu/50 Å Ni₈₁Fe₁₉ (circles) and a 20 Å Pt/50 Å Co₇₀Fe₃₀/40 Å Cu/50 Å Ni₈₁Fe₁₉ (squares) spin-valve base. The inset shows the collector current for the MTT with a Pt seed layer as a function of the magnetic field at $V_{EB} = 0.84$ V (open circles) and 0.88 V (solid circles).

Except for the different onset voltages for hot electron collection, the bias dependence of the transfer ratio is qualitatively the same for the two MTTs in Fig. 5.6. In both cases, the transfer ratio initially increases rapidly with bias once the Schottky barrier height is exceeded. Then it saturates at a bias voltage about 0.6 V above the Schottky barrier height. Such saturation is similar to that shown in Fig. 4.2 and is related to enhanced scattering for electrons with higher energies.

The maximum transfer ratio of the MTT is largely independent of the Schottky barrier height. Rather, it is determined mainly by hot electron scattering processes in the spin-valve base and at the base/collector interface. Therefore, to make a fair evaluation of the hot electron transmission efficiency of the MTT device, it is

metal	Schottky barrier height (eV)
Co ₇₀ Fe ₃₀	0.68 ± 0.01
Cu	0.65 ± 0.01
Au	0.78 ± 0.01
Pt	0.85 ± 0.01
Pd	0.74 ± 0.01
Ta	0.60 ± 0.02
Ti	0.60 ± 0.02

Table 5.1: Schottky barrier heights at the metal/Si(001) interfaces.

Fig. 5.7: Normalized transfer ratio as a function of the seed layer material and thickness at $V_{EB} = 1.4$ V.

necessary to compare the transfer ratio at a bias voltage at which the transfer ratio is almost saturated. Fig. 5.7 shows such a comparison at $V_{EB} = 1.4$ V for MTTs

with Cu, Au, Pt, and Pd seed layers. For Ta and Ti seed layers, the tunnel barrier breakdown voltage is less than 1.4 V and thus such measurements are not possible. The transfer ratios are normalized to that of an MTT without a seed layer (1.3×10^{-4} at $V_{EB} = 1.4$ V). In contrast to Fig. 5.5, the influence of the Schottky barrier height on the transfer ratio is minimized in Fig. 5.7. Except for Pt, the use of a seed layer increases the transfer ratio significantly. The initial increase of the transfer ratio at small seed layer thicknesses indicates an immediate decrease of hot electron scattering near the metal/semiconductor interface. The transfer ratio increases with the seed layer thickness up to about 20 Å, after which it slowly decreases. This decrease is due to hot electron attenuation in the metal seed layer and is proportional to $e^{-(t-t_c)/\lambda}$. Here, λ is the hot electron attenuation length in the metal seed layer, t is the total thickness of the seed layer, and t_c is the thickness of the intermixed metal/Si interface layer that is formed during the seed layer growth on Si(001). Fits to the data for $t \geq 20$ Å yield $\lambda = 105$ Å for Cu, 32 Å for Pt, and 27 Å for Pd at a hot electron energy of 1.4 eV. The attenuation length in the Au film is extremely large and no reduction in the transfer ratio is measured for seed layer thickness up to about 75 Å. The small hot electron attenuation lengths in Pt and Pd films lead to a large decrease in the transfer ratio for thick seed layers. On the other hand, Cu and Au seed layers improve the transfer ratio over a wide thickness range: thin layers of Cu and Au can effectively reduce the CoFe-silicide formation and improve the transfer ratio, while thicker layers of these materials do not significantly reduce the transfer ratio due to their large hot electron attenuation lengths.

Besides the formation of a better metal/Si interface, the use of a non-magnetic seed layer may introduce structural and morphological changes in the subsequently deposited films, which could also influence the MTT transfer ratio.

5.4 Magneto-Current

In Fig. 5.8 the MC is plotted as a function of the electron energy relative to the top of the Schottky barrier for MTTs with a 50 Å CoFe/40 Å Cu/50 Å NiFe spin-valve base grown on different seed layers. Giant MC effects are obtained for all MTTs over

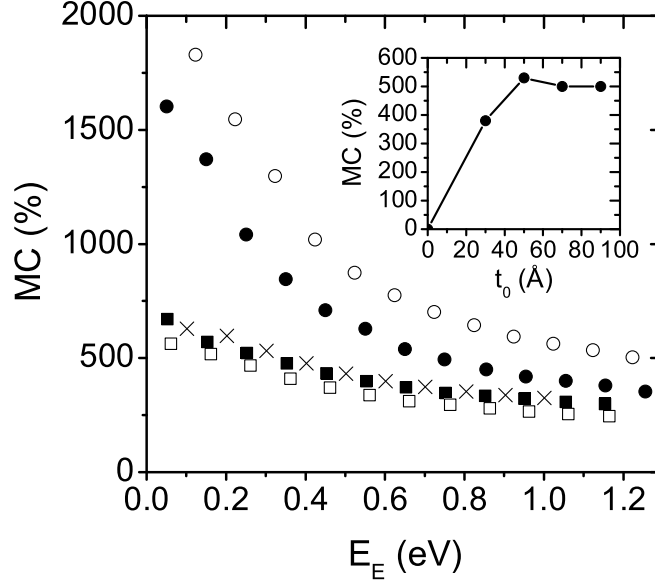


Fig. 5.8: MC as a function of the electron energy relative to the top of the Schottky barrier for MTTs with and without seed layers: no seed layer (crosses), 20 Å Cu (solid circles), 10 Å Au (open circles), 20 Å Pt (solid squares), 20 Å Pd (open squares). The inset shows the MC as a function of the CoFe layer thickness for MTTs without a seed layer at $V_{EB} = 1.0$ V.

a wide hot electron energy range. The decrease of the MC with electron energy can be explained by the model discussed in Chap. 3.

The seed layer affects the MC mainly by altering the switching behavior of the base magnetic moments. If the CoFe and NiFe magnetic moments switch abruptly at well separated magnetic fields, a nearly anti-parallel alignment of the moments can be realized. In this configuration, electrons with both spin states are effectively scattered in one of the two ferromagnetic layers. This results in a very small collector current and hence a giant MC effect. For MTTs without a seed layer or with 20-Å-thick Pt and Pd seed layers, such an anti-parallel alignment is never achieved and a reduced MC effect is observed. In contrast, for MTTs with thin Cu and Au seed layers, the reorientation of the base magnetic moments is more abrupt and occurs at

well separated magnetic fields. Therefore a large MC effect is obtained.

The use of seed layers may reduce the CoFe-silicide formation at the base/collector interface, which could also influence the MC. The intermixing of CoFe and Si reduces the effective CoFe layer thickness. Since the spin-filtering effect in ferromagnetic materials is stronger at larger layer thicknesses, a smaller CoFe thickness would decrease the spin-filtering effect and consequently the MC. The inset of Fig. 5.8 shows the dependence of the MC on the CoFe layer thickness (t_0) for MTTs with a t_0 CoFe/40 Å Cu/50 Å NiFe spin-valve base. Indeed, the MC increases with the CoFe layer thickness up to $t_0 \approx 50$ Å, after which it remains more or less constant. The insertion of a seed layer between the Si substrate and the CoFe layer will reduce the CoFe-silicide formation, which leads to a larger effective CoFe thickness. However, as illustrated by the inset of Fig. 5.8, this will not enhance the MC effect when the CoFe layer is thicker than 50 Å. Reduced CoFe-silicide formation in MTTs with a non-magnetic seed layer can therefore not explain the influence of the seed layers on the MC.

5.5 Magnetic Anisotropy

The transport measurements presented thus far were all conducted with the magnetic field parallel to the $[1\bar{1}0]$ direction of the Si(001) substrate. Fig. 5.9 shows the collector current measured with the magnetic field applied along different Si crystallographic orientations for an MTT with a 50 Å CoFe/40 Å Cu/50 Å NiFe spin-valve base. Rotation of the magnetic field away from the $[1\bar{1}0]$ direction changes neither the magnetic switching behavior of the base moments nor the MC. This clearly indicates the absence of a magnetic anisotropy in the CoFe and NiFe films, which is consistent with the multi-crystalline nature of the CoFe film when directly grown on Si(001) [83].

The same measurements were conducted for a similar MTT with a 20-Å-thick Cu seed layer and the results are given in Fig. 5.10. A uniaxial magnetic anisotropy is present in this device. Abrupt switching of the CoFe and NiFe moments and a large MC effect are only obtained when the magnetic field is parallel to the Si $[1\bar{1}0]$ direction, which is the magnetic easy axis direction. If the field is applied along the Si $[110]$ direction (the hard axis), a much smaller MC and very gradual magnetic

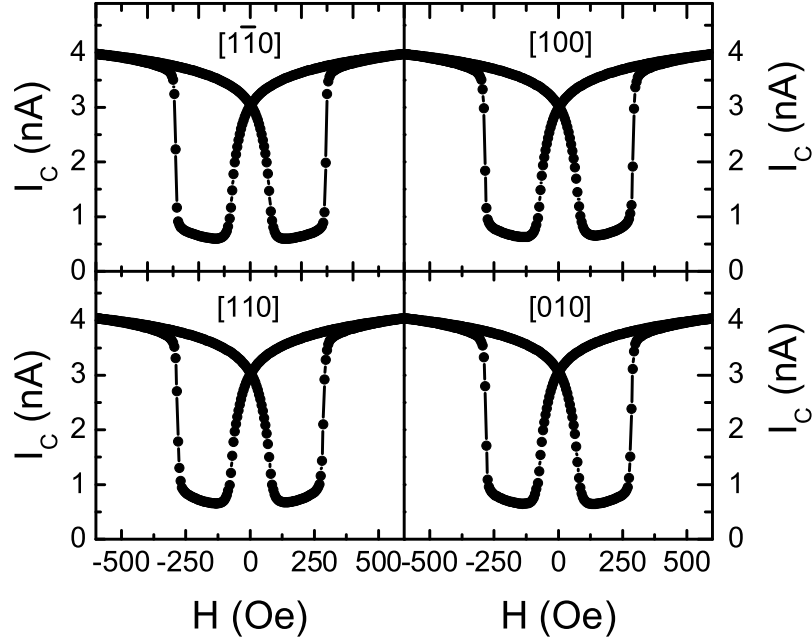


Fig. 5.9: Collector current as a function of the magnetic field applied along different directions for an MTT without a seed layer at $V_{EB} = 1.0$ V.

switching behavior is observed.

During the film deposition, there was a small magnetic field (provided by permanent magnets) in the deposition chamber along the Si $[1\bar{1}0]$ direction, which could induce the observed uniaxial anisotropy. In order to verify this, the same MTT device was grown with the Si substrate $[1\bar{1}0]$ direction at 90° with respect to the magnetic field direction in the deposition chamber. The magnetic easy axis of this MTT is now parallel to the Si $[110]$ direction (middle panel of Fig. 5.11), i.e., rotated by 90° with respect to the previous MTT. Therefore, the uniaxial magnetic anisotropy is indeed a result of the deposition geometry. Finally, a cubic magnetic anisotropy is observed if the MTT is grown with the Si substrate $[1\bar{1}0]$ direction at 45° with respect to the magnetic field direction in the deposition chamber (bottom panel of Fig. 5.11). The

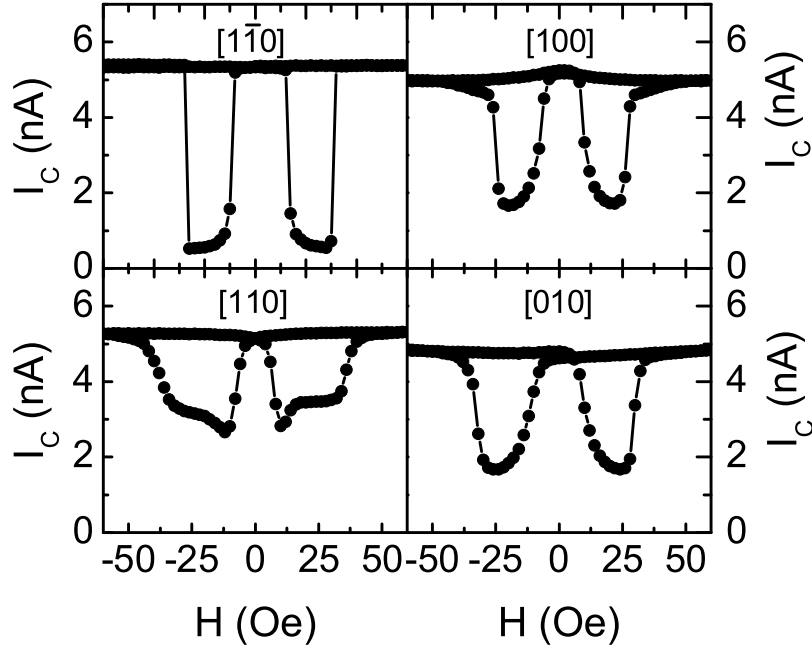


Fig. 5.10: Collector current as a function of the magnetic field applied along different directions for an MTT with a 20-Å-thick Cu seed layer at $V_{EB} = 1.0$ V.

magnetic easy axes in this case are along Si $[1\bar{1}0]$ and $[110]$ orientations. The presence of a cubic (due to the film structure) or uniaxial (due to the deposition geometry) magnetic anisotropy in the CoFe layer grown on Cu/Si(001) indicates that the CoFe film is mostly single crystalline, which is consistent with what has been reported in the literature [86, 87].

The results of magnetic anisotropy measurements for MTTs with or without a Cu, Au, Pt, or Pd seed layer are summarized in Fig. 5.12. Except for Cu, other seed layer materials do not introduce strong magnetic anisotropy, which is coincident with the large CoFe switching fields for MTTs with these seed layers (see Sec. 5.2). A plausible explanation is that these seed layers are not effective in preventing the intermixing between the CoFe layer and the Si substrate. As a result, a CoFe-silicide is

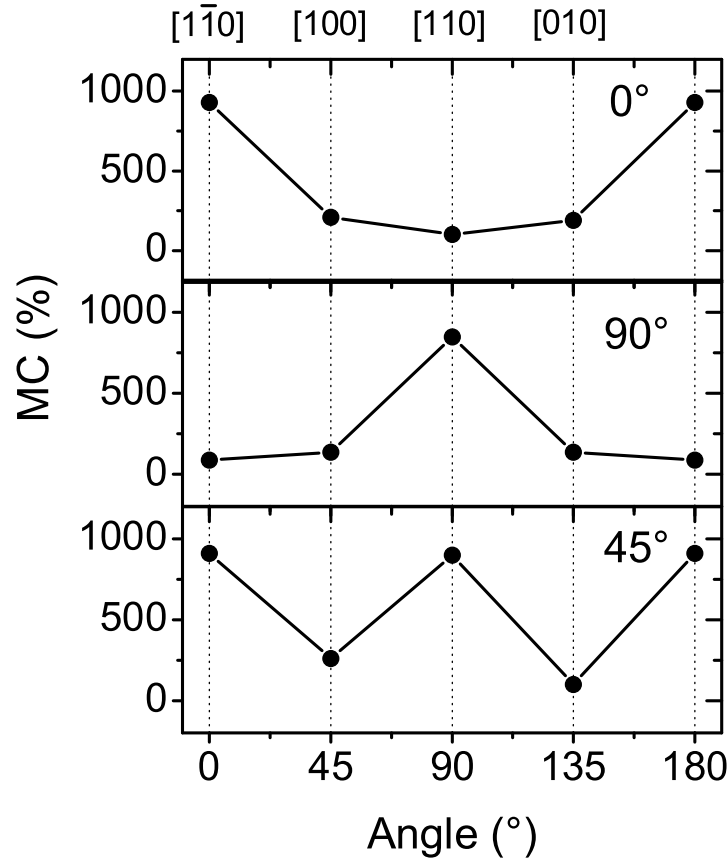


Fig. 5.11: MC as a function of the magnetic field direction for MTTs with a 20-Å-thick Cu seed layer at $V_{EB} = 1.0$ V. During film deposition, the Si substrate $[1\bar{1}0]$ direction was at 0° (upper panel), 90° (middle panel), and 45° (lower panel) with respect to the magnetic field direction in the deposition chamber.

formed, which is followed by the growth of a CoFe film containing grains with different crystallographic orientations. The reorientation of the magnetic moment of such a multi-crystalline film is gradual and nearly independent of the magnetic field direction. On the other hand, a 20-Å-thick Cu seed layer limits the intermixing between CoFe and Si, leading to a single crystalline CoFe film with a small switching field and a strong magnetic anisotropy. Increasing the Au, Pt, or Pd seed layer thickness will

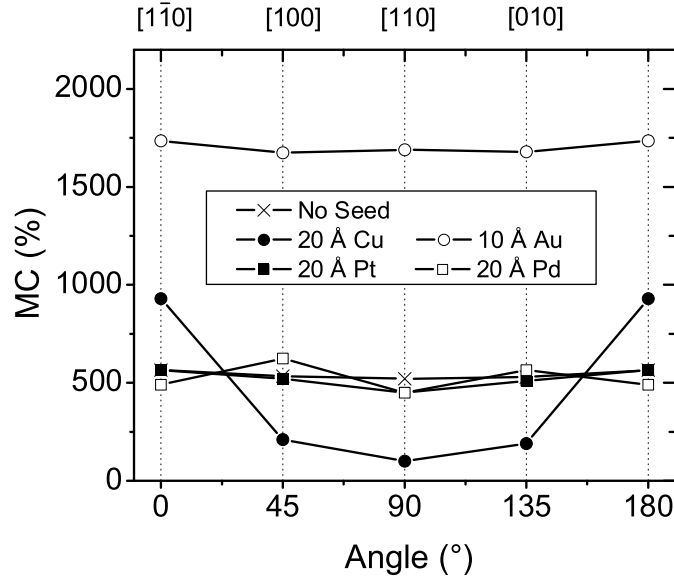


Fig. 5.12: MC as a function of the magnetic field direction for MTTs with or without seed layers at $V_{EB} = 1.0$ V.

eventually reduce the CoFe coercivity. In these cases, however, the CoFe and NiFe switching fields are no longer separable. As a result, the MC measurements cannot be used to study the magnetic anisotropy of the ferromagnetic films.

5.6 SIMS Analysis

Secondary ion mass spectrometer (SIMS) is a very useful technique to probe elemental composition depth profile of thin films. Several SIMS samples were grown with the following structures in order to study the intermixing between the metals and the Si substrate:

Si(001)/20 Å or no seed layer/50 Å $\text{Co}_{70}\text{Fe}_{30}$ /40 Å Cu/50 Å $\text{Ni}_{81}\text{Fe}_{19}$ /100 Å Ta

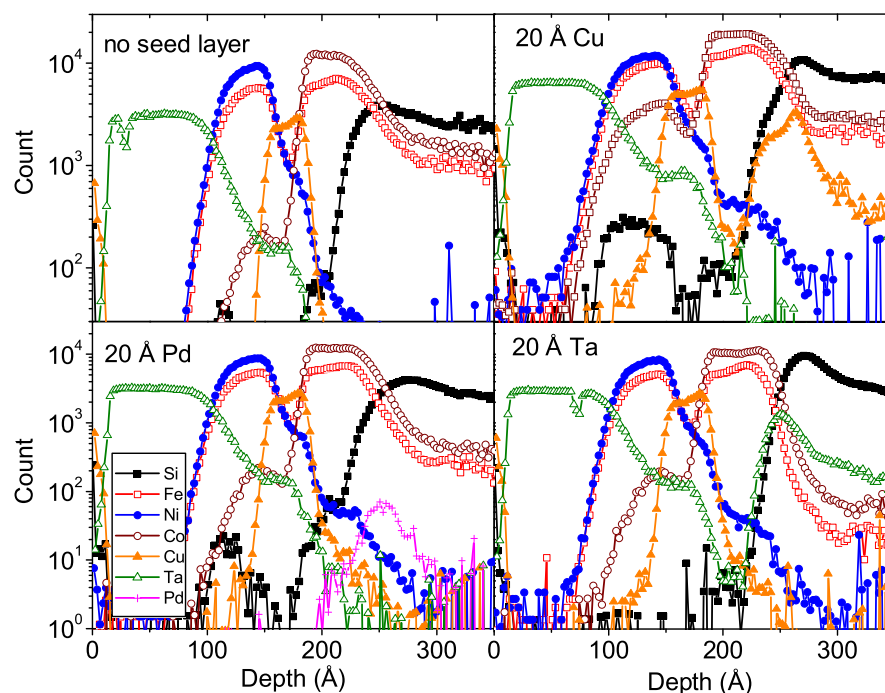


Fig. 5.13: SIMS data for samples without a seed layer and with a 20-Å-thick Cu, Pd, or Ta seed layer.

where the seed layer materials were Cu, Au, Pt, Pd, Ta, or Ti. For the sample with the Pt seed layer, the 50-Å-thick $\text{Ni}_{81}\text{Fe}_{19}$ layer was missing due to deposition errors.

Fig. 5.13 shows the SIMS data for the samples without a seed layer and with Cu, Pd, and Ta seed layers. The intermixing between Si and CoFe is evident for the sample without a seed layer. In contrast, the presence of a 20-Å-thick Cu seed layer limits such intermixing to mostly within the Cu film and greatly reduces the CoFe-silicide formation. The Pd seed layer is less effective in term of preventing the formation of CoFe-silicide. The Si profile clearly extends beyond the Pd layer. Ta works best as a barrier material for preventing the intermixing between Si and CoFe. The Si profile is confined within the seed layer. SIMS results for the Au, Pt and Ti seed layers are similar to those for the Cu, Pd and Ta seed layers, respectively.

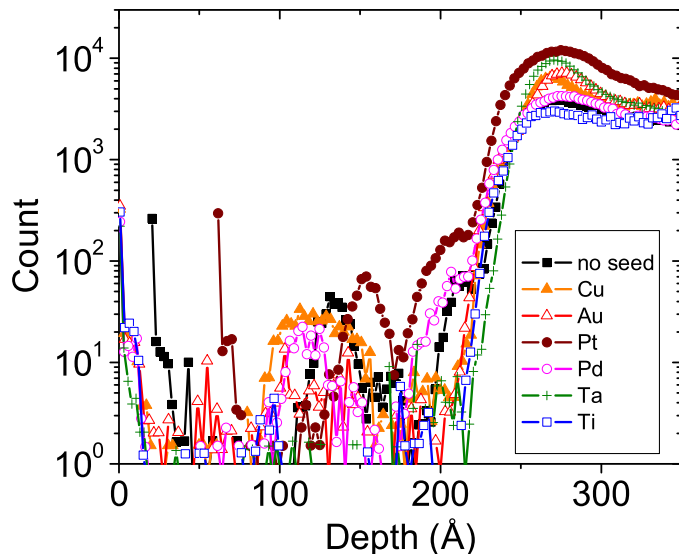


Fig. 5.14: Si depth profiles for the samples with or without seed layers.

The Si depth profiles for these samples are plotted in Fig. 5.14 for comparative purposes. For Cu, Au, Ta, and Ti seed layers, the Si concentration drops sharply at the metal/Si interface region, suggesting that these materials are effective for protecting the CoFe film. For Pt and Pd, the Si profile extends even further than that in the sample without a seed layer. A CoFe-silicide layer is obviously formed with 20-Å-thick Pt and Pd seed layers, which is consistent with the gradual switching of the CoFe moment and the smaller MC effects for MTTs with these seed layers. Although Ta and Ti are good barrier materials for preventing the CoFe-silicide formation, MTTs with these seed layers have poor performance. This is likely due to poor quality of the spin-valve base and the tunnel barrier grown on these seed layers.

5.7 Discussion and Summary

In this section, the experimental results are discussed using a simple morphological model. Three different situations are considered in this model. For MTTs without a

seed layer, part of the CoFe base layer intermixes with the Si substrate and forms a silicide. For MTTs with a thin seed layer, the seed layer is completely converted into silicide and a small amount of Si intermixes with the CoFe film. When the seed layer thickness exceeds a critical thickness t_c , only part of the seed layer forms silicide and the intermixing of Si with the rest of the seed layer and the CoFe layer is negligible.

The thickness of the CoFe-silicide in MTTs without a seed layer can be estimated from the CoFe layer thickness dependence measurements of the MC (inset of Fig. 5.8). No MC effect is measured if the CoFe film is thinner than about 25 Å. This agrees well with the silicide layer thickness found for Co and Fe films deposited on Si(001) [76,81, 82] and suggests that the CoFe-silicide is non-magnetic. Strong hot electron scattering in this silicide layer reduces the MTT transfer ratio. When the CoFe film thickness exceeds about 25 Å, a CoFe metal layer grows on the silicide layer, which likely consists of grains with different crystallographic orientations. As a result, the base magnetic moments switch very gradually in an external magnetic field. Perfect anti-parallel alignment of the base magnetic moments is never realized and a reduced MC effect is obtained. In addition, no magnetic anisotropy is observed due to the multi-crystalline nature of the ferromagnetic films.

The deposition of a seed layer induces an initial formation of a silicide interface layer on Si(001), followed by the corresponding metal film growth if the seed layer is thick enough [86–102]. The subsequent growth of the spin-valve base depends strongly on the seed layer thickness. If the seed layer is too thin, Si will still be able to intermix with CoFe. As a consequence, a CoFe-silicide layer is formed which is thinner than but has a structure similar to that formed when the CoFe layer is directly deposited on Si. Therefore, the magnetic switching behavior and transport properties of these MTTs do not differ much from those of MTTs without a seed layer. On the other hand, if the seed layer is thicker than the critical thickness t_c , very little CoFe-silicide will be formed and the CoFe film is mostly single crystalline. Such a film exhibits a strong magnetic anisotropy and a very abrupt switching behavior. In some cases, the coercivities of the CoFe and NiFe moments are no longer well separated, giving rise to a very small MC value. If, however, the seed layer material and thickness are appropriately selected, abrupt switching of the CoFe and NiFe moments can be

obtained at distinct switching fields, which will lead to a nearly perfect anti-parallel alignment of the CoFe and NiFe moments and thus a giant MC effect.

The proper use of a seed layer can increase the transfer ratio of the MTT. Although structural changes in the entire base layers may contribute to such an increase, the enhanced electron transmission is mostly due to much reduced base/collector interface scattering. Cu and Au seed layers provide the best interfaces in terms of hot electron collection efficiency. An additional advantage of Cu and Au seed layers is their large hot electron attenuation lengths, thus allowing the use of relatively thick seed layers without decreasing the collector current. Pt and Pd seed layers do not improve the transfer ratio significantly. They also have relatively short hot electron attenuation lengths which limit the use of thick seed layers. MTTs grown on Ta and Ti seed layers have poor performance. Neither the MC nor the transfer ratio is enhanced. Moreover, the tunnel barrier breakdown voltage is significantly reduced, which is not desirable for device operations.

Chapter 6

Tunnel Based Spin Injectors for Semiconductor Spintronics

6.1 Introduction

The dream of spin-based electronics has inspired much research into the transport and manipulation of carrier spins in semiconductors [2]. The electron spin relaxation time in semiconductors is found to be several orders of magnitude longer than the electron momentum and energy relaxation times [103]. Using an electric field, electrons in GaAs can be dragged over a distance of 100 μm without losing their spin coherence [104]. In addition to the long spin lifetimes and large spin diffusion lengths, semiconductors offer the flexibility of varying carrier doping profiles and spin relaxation rates, which can be very useful for building spintronic devices. For example, Ohno *et al.* showed that it is possible to control the ferromagnetism of InMnAs films by varying the hole concentration [105]. Karimov *et al.* demonstrated that electron spin relaxation rates in GaAs heterostructures can be varied by a factor of ten by applying a gate voltage [106]. These studies suggest that spin-based electronics could bring an entirely new generation of devices with fast speed, high density, low power consumption and non-volatility [107–110].

One of the prerequisites for semiconductor spintronics is to electrically generate spin-polarized carriers inside semiconductors for further manipulation, often referred

to as spin injection. The first demonstration of spin injection was achieved using diluted magnetic semiconductors, such as BeMnZnSe, GaMnAs, and ZnMnSe [111–113]. The ordering temperatures of these materials, however, are well below room temperature, thereby limiting their usefulness. By contrast, ferromagnetic metals display high Curie temperatures but, so far, direct spin injection from such metals into semiconductors using diffusive contacts shows very low efficiency [48, 49, 51, 52] and, in any case, may be fundamentally limited by the substantial conductivity mismatch between metals and semiconductors [50]. Inspired by the theoretical work of Rashba [53], ferromagnetic metal tunnel contacts, using either a carefully designed Schottky barrier [114–116] or an Al_2O_3 tunnel barrier [117–119], have been widely used for spin injection and promising progress has been made. In this approach, however, the maximum polarization of the injected electron current is limited by spin-dependent tunneling of electrons at the Fermi level of the metals. So far, the highest spin polarization reported in the literature using this method is about 32% at a low temperature (4.5 K) [116].

There is no such limitation for the magnetic tunnel transistor, in which the spin polarization of the injected electrons is determined mainly by spin-filtering in the base region of the device and can reach nearly 100%. Moreover, the magnetic tunnel transistor is a three terminal device, which allows the energy of these electrons to be varied over a wide range. In addition, since the electrons are injected ballistically through a tunnel barrier into the semiconductor, the device overcomes the fundamental conductivity mismatch problem. In Sec. 6.3, the first experimental demonstration of hot electron spin injection from an MTT source into semiconductors is discussed in detail. About 10% spin polarization is measured optically at 1.4 K using a GaAs/InGaAs quantum well (QW) light emitting diode (LED), which sets a lower bound on the spin injection efficiency. This study shows that electrons with a very high energy (~ 2 eV) are able to at least partially preserve their spin orientation after being transferred into semiconductors.

The moderate spin polarization obtained using an MTT injector is mostly likely due to spin relaxation of electrons with a very high energy [120]. Although the electrons at the base/collector interface are more than 95% spin-polarized, they lose

much of their polarization prior to recombination with the holes in the quantum well detector. To enhance the spin injection efficiency, a novel magnetic tunnel injector is formed from CoFe/MgO. Spin injection into GaAs from this type of injector is discussed in Sec. 6.4. Very high spin polarization of about 50% is observed at 100 K. Measurements at higher temperatures are limited only by the quantum well light emission efficiency.

6.2 Optical Selection Rules and Spin Relaxation Mechanisms

Quantum well light emitting diodes are commonly used as an optical detector of spin injection into direct band gap semiconductors, such as GaAs. In this method, the injected electrons (holes) are transported into a quantum well heterostructure, where they recombine with unpolarized holes (electrons) from the substrate and emit light. The circular polarization of the light is correlated to the carrier spin polarization by the optical selection rules [121]. The injected carriers may lose part or all of their spin polarization prior to recombination. Understanding such spin relaxation processes is therefore vital for the proper interpretation of the experiment. In the rest of this section, the selection rules and spin relaxation mechanisms are discussed in the context of electron injection since this is the case for the experiments presented in Sec. 6.3 and 6.4.

The most straightforward relation between the spin polarization of the injected electrons and the circular polarization of the quantum well electroluminescence (EL) is achieved in the Faraday geometry, where both the electron spin orientation and the light propagation direction are perpendicular to the quantum well plane. The optical selection rules in such a geometry are depicted in Fig. 6.1. For III-V compound semiconductors such as GaAs, the conduction band electrons have two spin states: $s = \pm 1/2$. In contrast, the GaAs hole spin states are more complicated. Two different holes, heavy holes (HH) ($s = \pm 3/2$) and light holes (LH) ($s = \pm 1/2$), are involved in electroluminescence. The recombination of electrons with holes will emit circularly

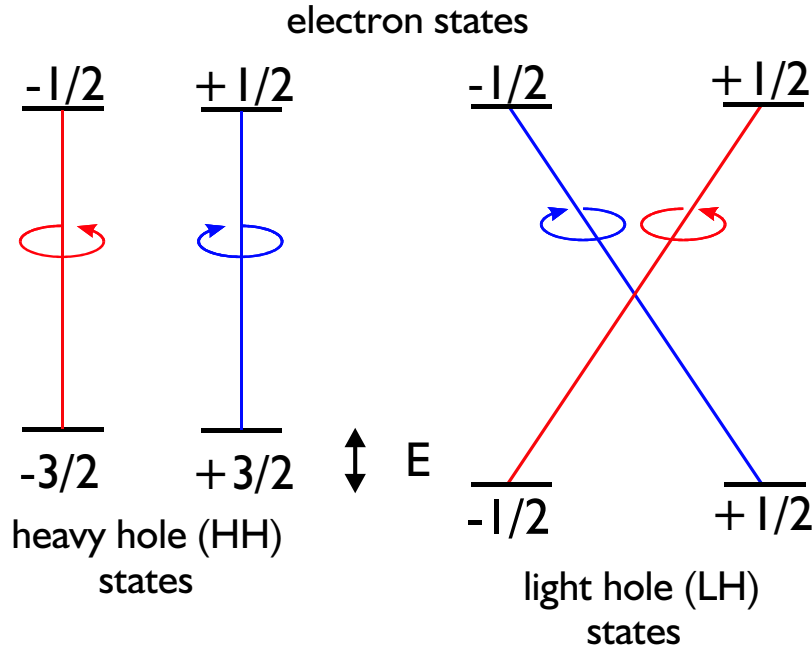


Fig. 6.1: Optical selection rules in the Faraday geometry.

polarized light, but the polarity of the light is opposite for electron recombination with the heavy and light holes. In bulk GaAs, the heavy and light hole bands are degenerate at the Brillouin zone center. In a quantum well, however, such degeneracy is lifted due to the confinement potential and/or the strain. Thus the heavy and light hole emission may be resolved spectrally if the emission linewidth is smaller than the splitting energy (ΔE) between the heavy and light hole bands. For the quantum well structures discussed in Sec. 6.3 and 6.4, the heavy hole band has smaller energy and dominates the electroluminescence. In this case, the measured EL polarization is equal to the electron spin polarization prior to recombination (Fig. 6.1).

In a typical spin injection experiment, the quantum well detector is buried inside the semiconductor heterostructure. The injected electrons are first transported into the quantum well region, where they spend a certain amount of time (described by the recombination time) before recombining with the holes and emitting light. The EL polarization does not include any spin relaxation effects prior to recombination and therefore sets a lower bound on the spin polarization of the injected electrons. To properly interpret the experimental data, it is necessary to understand various spin

relaxation mechanisms in semiconductors.

Spin relaxation mechanisms have been extensively studied via optical means [121]. Three relaxation mechanisms are found to be important: the Elliott-Yafet (EY), D'yakonov-Perel' (DP), and Bir-Aronov-Pikus (BAP) mechanisms. The EY process derives from the mixing of electron wave functions with opposite spin states due to spin-orbit coupling [122, 123]. As a result, electron momentum scattering leads to spin relaxation, with a rate proportional to the momentum scattering rate. The DP process is present in semiconductors without inversion symmetry [124, 125]. The mobile electrons see an effective magnetic field whose magnitude and orientation depend on the electron momentum. Spin precession around this magnetic field gives rise to spin relaxation. Momentum scattering randomizes the direction of the effective magnetic field and reduces the average precession effect. The DP spin relaxation rate is therefore inversely proportional to the momentum scattering rate, which is exactly the opposite to the EY process. The BAP process is due to electron-hole exchange and annihilation interactions [126]. In non-degenerate semiconductors, the BAP spin relaxation rate is proportional to the hole concentration. In the degenerate case, the hole concentration dependence of the spin relaxation rate becomes weaker [121]. The relative importance of the EY, DP, and BAP processes depends on the details of the sample and the experiment condition, such as semiconductor doping concentration, temperature, etc.

6.3 Spin Injection into GaAs from a Magnetic Tunnel Transistor

In this section it is shown that the MTT can be a useful source of spin-polarized hot electron currents for spintronic devices. In order to measure the spin injection efficiency, a quantum well light emitting diode was incorporated as the collector of the MTT, as shown in Fig. 6.2. The injected electrons recombined with holes in the quantum wells and emitted light. The circular polarization of the emitted light was then used to determine the electron spin polarization, as discussed in Sec. 6.2.

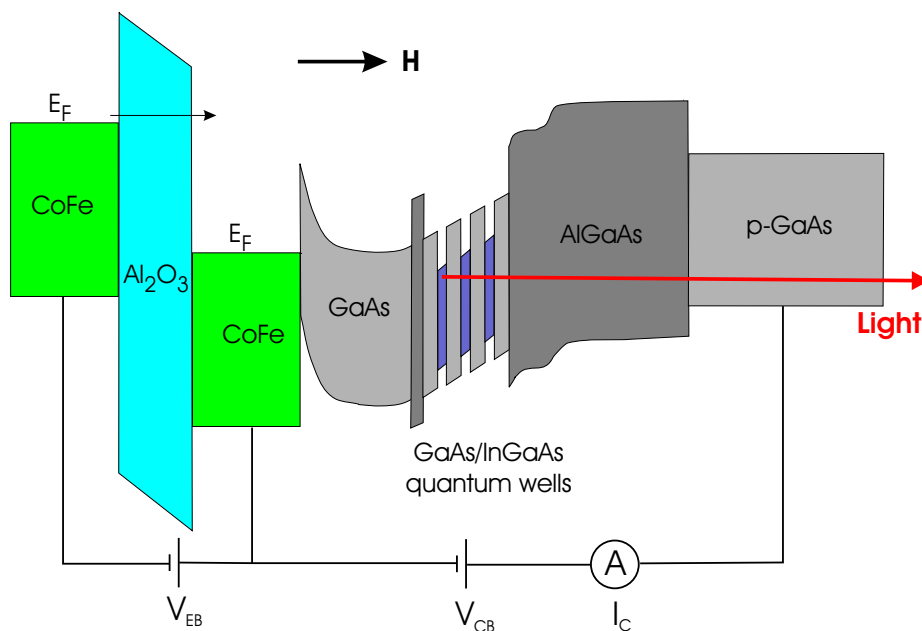


Fig. 6.2: An MTT spin injector with a QW detector.

The semiconductor LED structure was grown by molecular beam epitaxy (MBE) at Stanford University. Three p-type Al_{0.32}Ga_{0.68}As layers with stepped doping concentrations were first grown on a Be doped p-GaAs substrate: 4000 Å Al_{0.32}Ga_{0.68}As ($1 \times 10^{19} \text{ cm}^{-3}$) / 2800 Å Al_{0.32}Ga_{0.68}As ($2 \times 10^{18} \text{ cm}^{-3}$) / 1000 Å Al_{0.32}Ga_{0.68}As ($1 \times 10^{17} \text{ cm}^{-3}$). Subsequently a 600-Å-thick undoped Al_{0.32}Ga_{0.68}As layer was grown. The active region of the LED consisted of three GaAs/In_{0.2}Ga_{0.8}As quantum wells grown on top of the Al_{0.32}Ga_{0.68}As buffer layers, with an InGaAs well width of 80 Å and a GaAs barrier layer thickness of 150 Å. Another thin undoped Al_{0.32}Ga_{0.68}As layer (50 Å) was then grown on top of the quantum wells. Finally, 1000 Å n-type GaAs (Si doped, $5 \times 10^{16} \text{ cm}^{-3}$) was grown as the top layer to form a Schottky barrier with the ferromagnetic metal base. The doping concentration of this layer was optimized to obtain desired Schottky barrier characteristics. The Al_{0.32}Ga_{0.68}As layers on both sides of the quantum wells help to confine electrons and holes within the wells to promote recombination, i.e., the Al_{0.32}Ga_{0.68}As layers on the bottom prevent the hot electrons from traveling deep into the p-type layers, while the thin upper Al_{0.32}Ga_{0.68}As layer prevents the holes from traveling into the lightly doped n-type

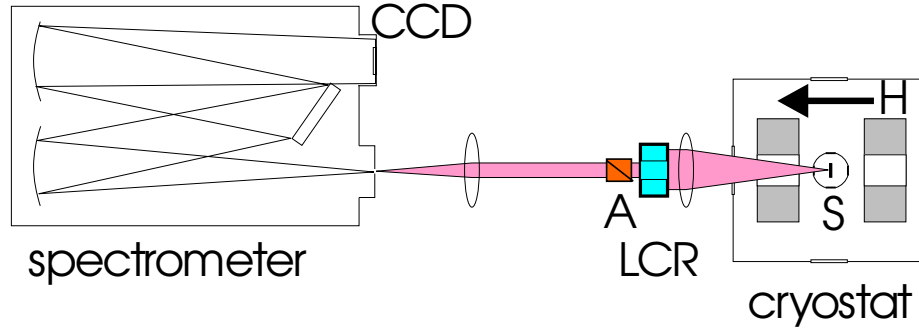


Fig. 6.3: Optical setup for the EL polarization measurements.

layer. The $\text{Al}_{0.32}\text{Ga}_{0.68}\text{As}$ layers on the substrate side also prevent the Be dopants from diffusing into the quantum well region. Finally, an arsenic capping layer was deposited on the top surface to prevent oxidation and to protect the top surface before the sample was removed from the MBE chamber and transferred into the sputtering chamber for MTT deposition. This capping layer is important since oxides or defects at the semiconductor surface could scatter electrons and reduce their spin polarization.

After the MBE growth, the sample was transferred in air into the ultra-high-vacuum sputtering chamber, where it was first heated at about 520°C to remove the arsenic cap. The sample was then cooled down to room temperature and the magnetic tunnel transistor was formed on the semiconductor LED by magnetron sputtering. A sequence of three shadow masks were used to form the base layer, the emitter isolation pads and the emitter layer, respectively. The base layer was comprised of 35 \AA $\text{Ni}_{81}\text{Fe}_{19}$ and 15 \AA $\text{Co}_{84}\text{Fe}_{16}$, with the NiFe layer adjacent to the LED. An Al_2O_3 tunnel barrier was then grown by reactive sputtering of Al in the presence of oxygen with a thickness of about 22 \AA . The emitter layer consisted of 50 \AA $\text{Co}_{84}\text{Fe}_{16}$. A 50-\AA -thick Ta layer was used as the capping layer to prevent oxidation of the CoFe emitter.

Fig. 6.3 shows the schematic drawing of the optical setup for the spin-polarized electroluminescence measurements. The MTT device was placed in a superconducting magnet cryostat with optical access. A magnetic field perpendicular to the ferromagnetic layers was applied to rotate their magnetic moments out of the film plane.

The emitter/base bias voltage V_{EB} determined the energy of the injected electrons, while the collector/base bias voltage V_{CB} was used to adjust the band-bending of the LED structure (Fig. 6.2). The GaAs/InGaAs quantum well luminescence energy is smaller than the GaAs band gap energy. Thus the substrate was transparent and the electroluminescence from the quantum wells was collected through the substrate. A combination of a liquid crystal retarder (LCR) and a linear polarizer (A) was used to selectively analyze the circular polarization components of the emitted light as σ_+ (left hand) or σ_- (right hand): the LCD converted the circularly polarized light into linearly polarized light, and the linear polarizer selected the desired polarization component for measurements. The spectrum of the selected component was measured with a grating spectrometer and a charge-coupled device (CCD).

The EL spectrum shown in Fig. 6.4 was measured with $V_{EB} = 2.06$ V and $V_{CB} = 1.0$ V at 1.4 K. The emitter and collector currents were 280 μA and 11.5 μA , respectively. The thick red and thin black lines represent the σ_+ and σ_- polarization components, respectively. Note that the width of the EL peaks was only about 2.5 nm, which was limited by the spectrometer resolution for the given signal level. According to absorption studies of similar samples, the separation in wavelength between the heavy and light hole emission peaks was about 40 nm in 80-Å-wide $\text{In}_{0.2}\text{Ga}_{0.8}\text{As}$ quantum wells. Therefore, the narrow EL linewidth enabled an unambiguous detection of electron-HH recombination, and the light polarization was equal to the electron spin polarization immediately prior to recombination.

As shown in Fig. 6.4, the EL polarization clearly depends on the magnetic field. At zero field, the intensities of the σ_+ (I_+) and σ_- (I_-) components are identical. At high fields, the EL becomes polarized with a significant difference between I_+ and I_- . The EL polarization is defined as:

$$P_{EL} = \frac{I_+ - I_-}{I_+ + I_-} \quad (6.1)$$

P_{EL} of about 13% at 2.5 T and -13% at -2.5 T are obtained at 1.4 K. The sign of P_{EL} indicates the injection of majority electron spins (-1/2 spin state) into the quantum wells, which is consistent with the sign of the collector current polarization observed

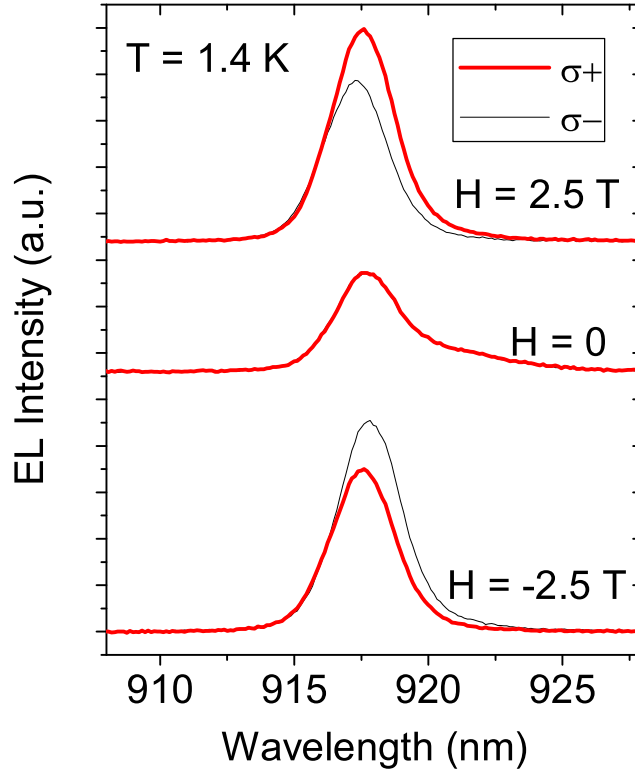


Fig. 6.4: EL spectrum measured at magnetic fields of 0 and ± 2.5 T at 1.4 K for an MTT injector. The thick red and thin black lines represent the σ_+ and σ_- circular polarization components, respectively.

in electrical transport measurements of similar magnetic tunnel transistors. Excitons in GaAs/In_{0.2}Ga_{0.8}As quantum wells have a large g-factor, leading to a large Zeeman splitting energy as shown by the shift of the EL peak center positions for the σ_+ and σ_- components at high magnetic fields. The overall EL intensity at zero magnetic field is smaller than that at high magnetic fields. The origin of such field dependence is unclear at present. It may result from a change of the recombination efficiency and/or spin relaxation rate in the quantum wells caused by the magnetic field.

In Fig. 6.5(a), the EL polarization is plotted as a function of the magnetic field

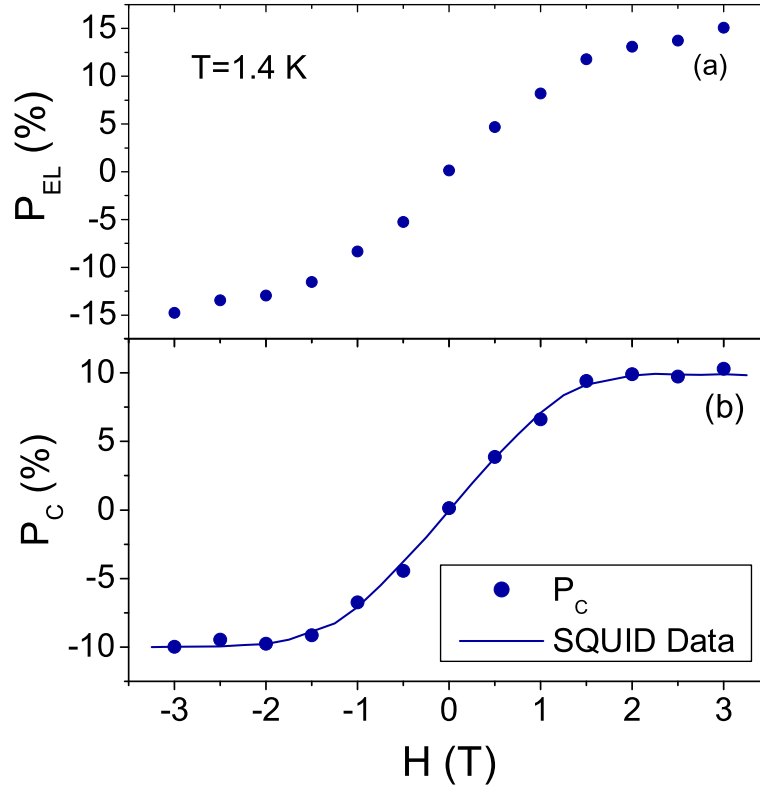


Fig. 6.5: EL polarization before (a) and after (b) subtraction of a linear background as a function of the magnetic field for an MTT injector. The solid line in (b) is the magnetization of the ferromagnetic layers measured with SQUID at 10 K, which is scaled to compare with the polarization data.

under the same bias conditions as described above. P_{EL} increases rapidly with the magnetic field up to ~ 2 T, where the magnetic moments of the ferromagnetic layers are expected to be completely rotated out of plane by the field. Above 2 T, P_{EL} continues to increase with the field, but at a slower rate. For GaAs/InGaAs quantum well light emission at low temperatures, the increase of circular polarization at high magnetic fields is likely due to a background polarization caused by thermalization of the exciton spins in the magnetic field. Shown in Fig. 6.5(b) is the polarization P_C

obtained after subtracting this linear background polarization from P_{EL} . A P_C value of about 10% is measured at high fields.

Polarization dependent light reflection at the ferromagnetic base/GaAs interface may give rise to a contribution to the EL polarization. However, it was found that this effect is very small (less than 1%) by passing linearly polarized light through the backside of the wafer and measuring the polarization of light reflected from the ferromagnetic layers. The solid line in Fig. 6.5(b) shows the magnetization of the ferromagnetic layers measured with a SQUID magnetometer at 10 K in a magnetic field oriented perpendicular to the layers. The field dependence of the emitter and base magnetization is in excellent agreement with the field dependence of P_C , confirming that P_C is related to the injection of spin-polarized hot electrons from the magnetic tunnel transistor injector.

Fig. 6.6(a) summarizes the collector/base bias voltage dependence of P_{EL} measured at 2.5 T. Below about 1 V the luminescence is too weak to measure P_{EL} . Above 1 V P_{EL} first decreases with bias, then changes sign at $V_{CB} \approx 1.4$ V, and finally stays approximately constant at higher bias voltages. Note that P_{EL} does not exclude the background polarization effects. The sign reversal of P_{EL} suggests that the injected electrons completely lose their initial spin orientation prior to recombination at high bias voltages due to a strong bias dependence of the spin relaxation rate in the semiconductor. Increasing V_{CB} results in a larger hole current flowing from the p-GaAs substrate into the quantum wells [see the inset of Fig. 6.6(a)]. Electron-hole interactions can result in electron spin relaxation to the $s = +1/2$ state through the BAP mechanism. When the hole concentration is low, the spin relaxation rate is proportional to the number of holes in the quantum wells and, therefore, is expected to increase with the collector/base bias voltage. Other spin relaxation processes could also be influenced by the bias. For example, spin relaxation through the DP mechanism is very sensitive to the hot electron energy [120]. At large collector/base bias voltages, the conduction band bending of the top n-GaAs layer increases and the injected hot electrons would need to lose more energy to reach the bottom of the conduction band. During this process, they are more likely to lose their initial spin orientation.

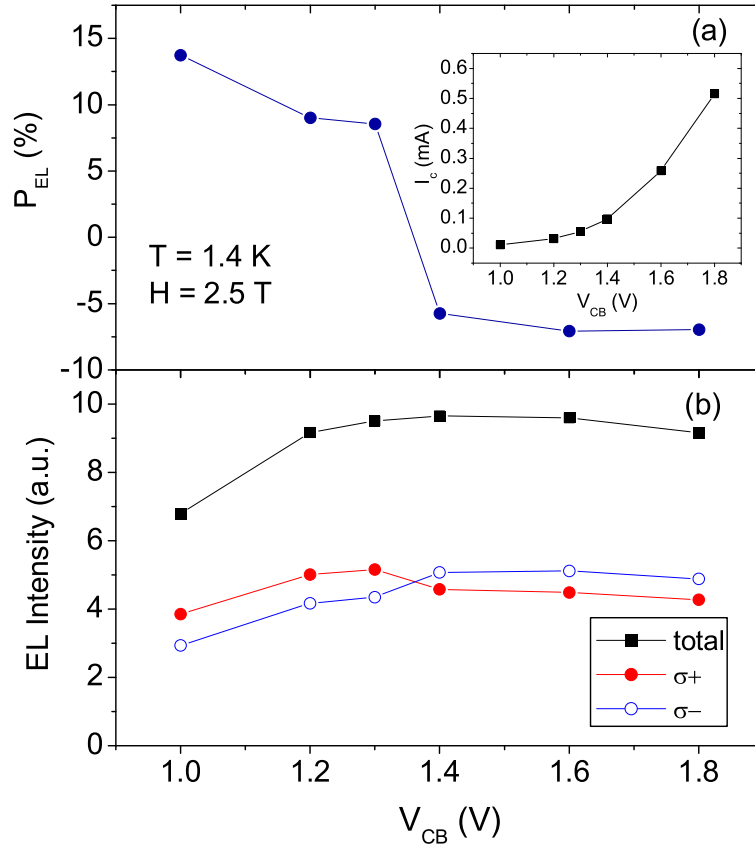


Fig. 6.6: Collector/base bias dependence of the EL polarization (a) and intensity (b). The EL polarization was measured at 2.5 T without background subtraction. The inset in (a) shows the collector current as a function of V_{CB} .

The bias dependence of the EL intensities at 2.5 T is summarized in Fig. 6.6(b). Increasing the collector/base bias voltage brings more holes into the quantum wells. As a result, electron-hole recombination becomes more efficient and the EL intensities go up with bias. However, when the bias is above ~ 1.4 V, there are already enough holes in the quantum wells. Recombination is now limited by the number of electrons injected into the quantum wells. Thus, the total EL intensity stays approximately

constant. Meanwhile, the intensity of the σ_+ component decreases due to spin relaxation to the $s = +1/2$ state prior to recombination, which leads to a negative EL polarization at high bias.

The DP electron spin relaxation rate in GaAs is approximately proportional to E^3 , E being the electron energy. As a result, the DP mechanism becomes very effective at elevated electron energies [120]. The injected hot electrons lose a significant amount of polarization during the process of thermalization to the bottom of the conduction band. After the hot electrons are transported into the quantum well region, further spin relaxation can occur before recombination [127]. The measured EL polarization indicates the electron spin polarization right before they recombine with the holes and, therefore, sets a lower bound on the spin injection efficiency. It would be interesting to use other semiconductor collectors (e.g., Si or GaN), where the DP mechanism is not so important [120, 128]. Under these circumstances the measured spin polarization should be larger.

6.4 Spin Injection into GaAs from a MgO Based Tunnel Injector

The small collector current of the MTT requires the device to operate at a high electron energy in order to obtain enough signal in the spin injection experiments. Electron spin relaxation, however, is very efficient at this high energy leading to a moderate EL polarization of about 10%. To increase the electron current at lower energies while maintaining a high spin polarization, a CoFe/MgO tunnel injector is formed for spin injection. The tunneling spin polarization of an Fe/MgO structure has been studied using first principle calculations [129, 130]. It was found that for the majority electrons, the Bloch states with Δ_1 symmetry decay slowly in the MgO barrier as evanescent states with the same symmetry. For the minority electrons, however, no Bloch states have Δ_1 symmetry, leading to rapid decay of these states in the MgO barrier. As a result, the majority electrons have a much larger tunneling conductance than the minority electrons and, therefore, a high spin polarization of the

tunneling current is expected. This was confirmed by Parkin *et al.* experimentally, where they measured a tunneling spin polarization of about 85% in an optimized CoFe/MgO structure using superconducting tunneling spectroscopy [131]. Such a high spin polarization is very attractive for spin injection.

Comprehending the spin relaxation processes in semiconductors is essential for the design and operation of spintronic devices. Spin relaxation has been extensively studied for optically excited carriers [121]. While these studies are of great importance, it is necessary to perform direct measurements of spin relaxation in the context of electrical injection. Recent efforts on electrical spin injection, however, have focused mainly on improving the injection efficiency. The study of spin relaxation of electrically injected carriers remains inadequate.

In this section, the spin injection experiments using a CoFe/MgO tunnel injector are presented. GaAs/Al_{0.08}Ga_{0.92}As quantum well LEDs were used to optically detect the spin injection efficiency. Electroluminescence polarization reached $\sim 50\%$ at 100 K. The temperature and bias voltage dependence of the EL polarization was consistent with a dominating DP spin relaxation mechanism in these experiments.

The schematic band diagram of the two terminal CoFe/MgO tunnel injector and the quantum well LED detector is shown in Fig. 6.7. Both n-i-p and p-i-p LEDs were grown using MBE at Stanford University with the following structure: p-GaAs substrate / 5700 Å p-Al_{0.08}Ga_{0.92}As buffer layers / 750 Å undoped Al_{0.08}Ga_{0.92}As / 100 Å undoped GaAs / 150 Å undoped Al_{0.08}Ga_{0.92}As / 1000 Å n- or p- Al_{0.08}Ga_{0.92}As (n $\sim 5 \times 10^{16}$ cm⁻³ and p $\sim 1 \times 10^{17}$ cm⁻³) / 50 Å undoped GaAs. These samples were capped with arsenic in the MBE chamber before transferred in air into the sputtering deposition chamber, where they were heated at 550 °C to remove the arsenic cap. After the samples cooled down to room temperature, shadow masks were used to deposit a 31-Å-thick MgO tunnel barrier and a 50-Å-thick Co₇₀Fe₃₀ electrode. Finally, a Ta capping layer was used to protect the CoFe film from oxidation. The active injector area was about $100 \times 300 \mu\text{m}^2$.

The samples were mounted in the superconducting magnet cryostat for spin-polarized EL measurements. By applying a bias voltage (V_T) across the LED structure, spin-polarized electrons were injected from the CoFe electrode into the quantum

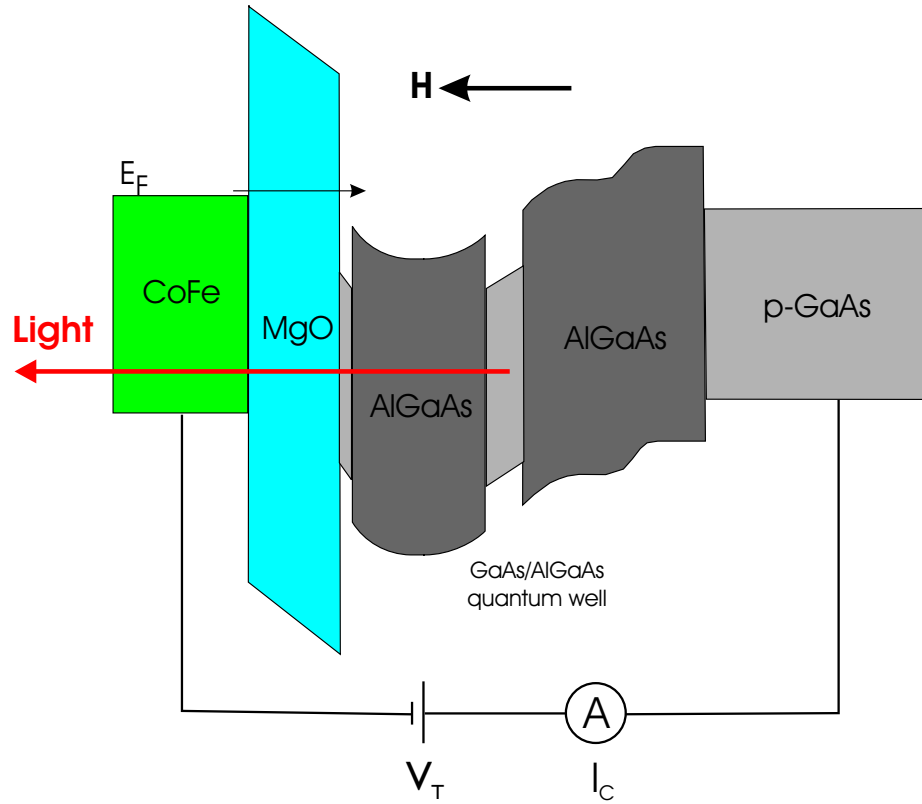


Fig. 6.7: A CoFe/MgO spin injector with a QW detector.

well, where they recombined with holes from the substrate and emitted light. The excitons in the GaAs/AlGaAs quantum well have a small g -factor. Thus the EL background polarization was significantly reduced. However, the GaAs substrate was no longer transparent to the luminescence. Therefore the light had to be collected from the front-side of the sample, i.e., through the metal and MgO layers. The same optical setup as described in Sec. 6.3 was used to measure the EL polarization at various temperatures and bias voltages in a perpendicular magnetic field, which rotated the CoFe magnetic moment out of the film plane.

Fig. 6.8 shows the EL spectrum of the n-i-p sample at 100 K with a bias voltage and current of 1.8 V and 0.12 mA, respectively. The longer wavelength EL peaks are due to electron-HH recombination, whose intensities are equal for the left and right circular polarization components in the absence of a magnetic field while becoming

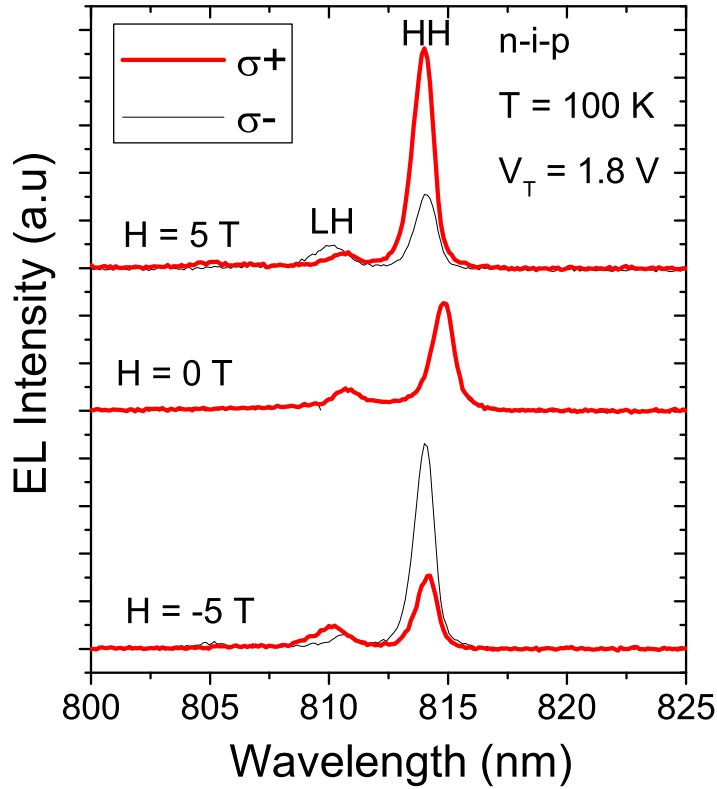


Fig. 6.8: EL spectrum measured at magnetic fields of 0 and ± 5 T at 100 K for a CoFe/MgO injector. The thick red and thin black lines represent the σ_+ and σ_- circular polarization components, respectively.

significantly polarized at magnetic fields of ± 5 T. Again, the sign of P_{EL} indicates majority electron spin injection from the CoFe layer. The shorter wavelength EL peaks are due to electron-LH recombination and appear only at temperatures above 30 K when the light hole band becomes thermally populated. The heavy hole emission is well resolved from the light hole emission in these experiments due to its narrow peak linewidth (~ 1 nm). The discussion hereafter focuses on the heavy hole emission only and its polarization is referred to as P_{EL} , which is equal to the electron spin polarization prior to recombination (see Sec. 6.2).

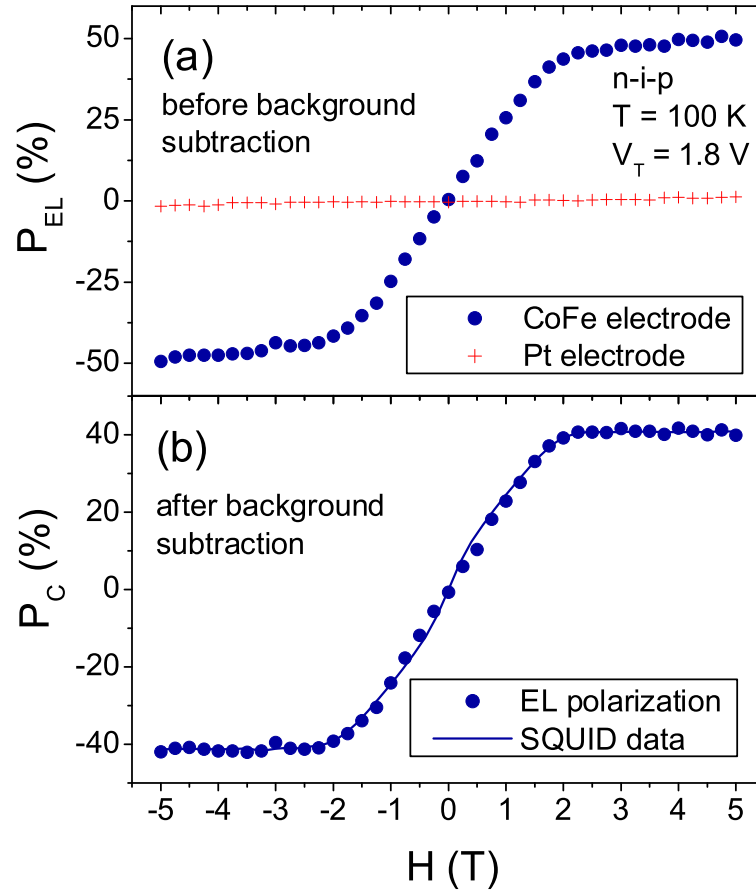


Fig. 6.9: EL polarization before (a) and after (b) subtraction of a linear background as a function of the magnetic field for a CoFe/MgO injector. The crosses in (a) is the EL polarization measured when the CoFe electrode is replaced by a Pt electrode. The solid line in (b) is the CoFe magnetization measured with SQUID at 20 K, which is scaled to compare with the polarization data.

The magnetic field dependence of P_{EL} for the n-i-p sample is depicted in Fig. 6.9(a) (solid circles). The polarization increases rapidly with the field up to about 2 T, when the CoFe moment is completely rotated out of plane. Above 2 T, P_{EL} continues to increase with the field approximately linearly at a slower rate of $\sim 1.7\%/T$ and

finally reaches $\sim 50\%$ at 5 T. This linear increase of P_{EL} above 2 T (referred to as the "background" polarization hereafter) is most likely due to the suppression of spin relaxation by the magnetic field. It is well-known that a perpendicular magnetic field can reduce DP spin relaxation [121], which dominates in these experiments as will be discussed later in this section. In photoluminescence studies of similar structures with a circularly polarized pump light, reduced spin relaxation was indeed seen when a perpendicular magnetic field was applied. Note that Zeeman splitting in the GaAs/AlGaAs quantum well is negligible, compared to kT, at 100 K and cannot account for the observed background polarization. P_C , the EL polarization after subtraction of the linear background, is shown in Fig. 6.9(b) (solid circles) as a function of the magnetic field. A P_C value as high as 42% is obtained at 100 K. The solid line in Fig. 6.9(b) is the CoFe magnetization measured with SQUID at 20 K in a perpendicular magnetic field. The excellent agreement between the EL data and the SQUID data indicates that the large EL polarization truly originates from spin injection by the CoFe/MgO tunnel injector.

For comparative analysis, P_{EL} was measured for a control sample with a non-magnetic Pt electrode in place of CoFe [crosses in Fig. 6.9(a)]. The polarization was on the order of 1% and had very weak magnetic field dependence. Additional photoluminescence experiments with a linearly polarized pump light also gave a small polarization ($< 2\%$) and weak field dependence. These results proved that the effects of polarization-dependent light absorption or reflection by the metal and semiconductor layers were very small.

The bias and temperature dependence of P_C is summarized in Fig. 6.10 for both the n-i-p and p-i-p samples. The relatively small confinement potential of the GaAs/Al_{0.08}Ga_{0.92}As quantum well leads to very weak EL signal at high temperatures and thus limits the experiments to 1.4 – 100 K. Over this temperature range, P_C decreases with bias at a given temperature. A similar bias dependence has been observed in optical experiments, which was attributed to spin relaxation through the DP mechanism before photo-excited electrons reached the quantum well [132]. Higher bias voltages lead to an increased electron momentum and consequently a larger effective magnetic field for DP spin relaxation, which results in a smaller EL

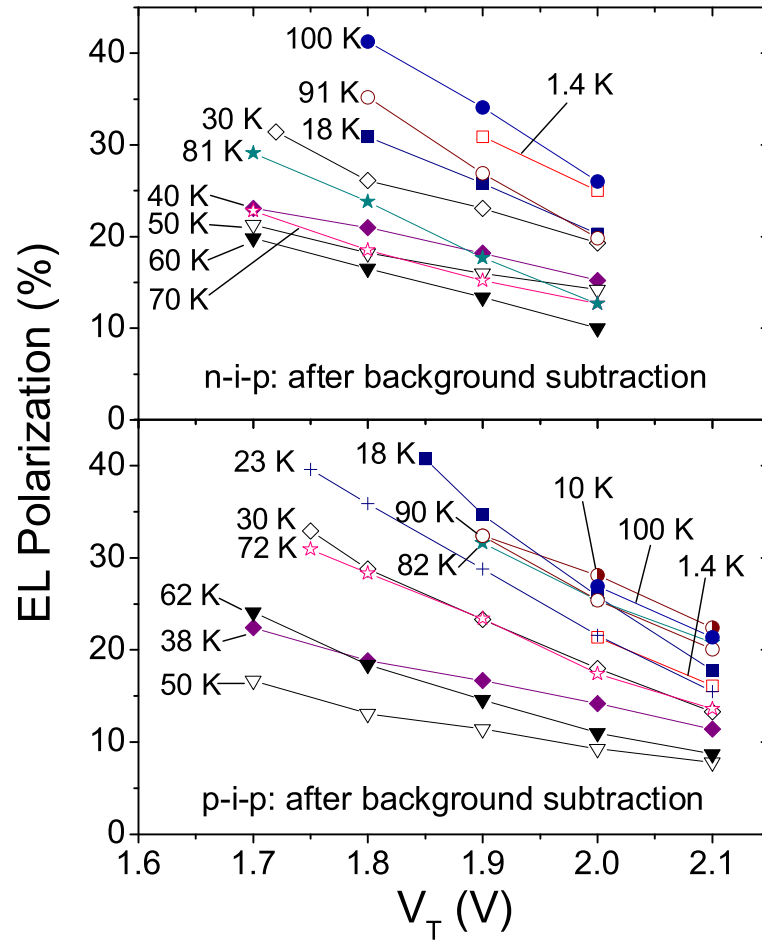


Fig. 6.10: Bias and temperature dependence of P_C for the n-i-p (a) and p-i-p (b) samples.

polarization.

The temperature dependence of P_C is rather striking: P_C begins quite high at low temperatures, decreases with temperature towards a minimum at $\sim 50 - 60$ K, then increases with temperature. This unique temperature dependence is most clearly illustrated in Fig. 6.11, where P_C at a given bias voltage is plotted as a function of temperature for both the n-i-p (open circles) and p-i-p (solid circles)

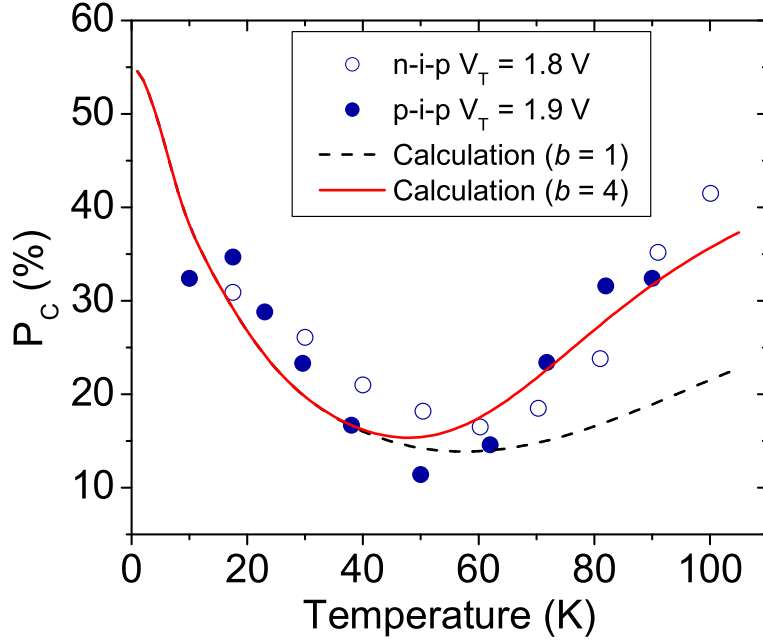


Fig. 6.11: Measured temperature dependence of P_C for the n-i-p (open circle) and p-i-p (solid circles) samples and calculated results for $b=1$ (dashed line) and $b=4$ (solid line). Other fitting parameters used in the calculations are: residual donor and acceptor concentrations $5 \times 10^{13} \text{ cm}^{-3}$ and $1 \times 10^{13} \text{ cm}^{-3}$, deformation potential 7 eV, polar optical phonon energy 35 meV, electron effective mass 0.067, spin polarization when the electrons reach the QW 55%, electron-HH recombination time 320 ps. These parameters are consistent with values in the literature for GaAs heterostructures.

samples. The non-monotonic temperature dependence is strong evidence that the electron spin relaxation is dominated by the DP mechanism within the quantum well. The DP spin relaxation rate (τ_S^{-1}) in a quantum well is given by $\tau_S^{-1} \propto \tau_P T$, where τ_P is the electron momentum relaxation time and T is temperature [125, 133]. At low temperatures, the momentum scattering is dominated by ionized impurity scattering and has weak temperature dependence. As a result, $\tau_P T$ increases with temperature and so does τ_S^{-1} . At high temperatures, polar optical phonon scattering, which increases very rapidly with temperature, dominates the momentum scattering.

Consequently $\tau_P T$, and therefore τ_S^{-1} , decrease with temperature. The variation of the electron momentum scattering rate with temperature gives rise to the observed temperature dependence of P_C [133].

A model calculation is used to elucidate the origin of the temperature dependence of P_C . The electron momentum relaxation rate due to impurity and phonon scattering is calculated using the following equation:

$$\left\langle \frac{1}{\tau_P(E)} \right\rangle = \left\langle \frac{1}{\tau_I(E)} + \frac{1}{\tau_N(E)} + \frac{1}{\tau_D(E)} + \frac{1}{\tau_{PE}(E)} + \frac{b}{\tau_{OP}(E)} \right\rangle \quad (6.2)$$

where E is the electron energy, τ_I , τ_N , τ_D , τ_{PE} , and τ_{OP} are momentum scattering times due to ionized impurity, neutral impurity, deformation potential acoustic phonon, piezoelectric phonon, and polar optical phonon scattering, respectively [134], b is a fitting parameter, and $\langle \rangle$ denotes averaging over the electron energy distribution. This model is not meant to be rigorous and so, for simplicity, the bulk momentum scattering rates are used in the calculations. However, a fitting parameter b is used to adjust the weight of the polar optical phonon scattering. With $b = 1$, the non-monotonic temperature dependence of P_C is reproduced (dashed line in Fig. 6.11) although the rise of P_C at high temperatures is not as large as the experiment data, suggesting that some momentum scattering mechanisms are not included or underestimated in the model [135, 136]. Indeed, much improved agreement with the experimental results is obtained by arbitrarily increasing the polar optical phonon scattering rate, i.e., setting $b = 4$ (solid line in Fig. 6.11). Note that in these calculations, the spin polarization when the electrons arrive at the quantum well is assumed to be a temperature-independent constant (see the caption of Fig. 6.11). This suggests that the spin injection efficiency is not sensitive to temperature.

A few subtle points require further discussion. First, the model does not consider any magnetic field effects. Therefore the calculated results are compared with P_C , which excludes the magnetic field dependence of the EL polarization. Second, the bias voltage V_T is across the entire LED structure. As the temperature changes, the total voltage drop across the MgO barrier and the n- or p-AlGaAs depletion region (V_1) can vary slightly even if V_T remains constant. As shown in Fig. 6.10, P_C

is quite sensitive to the bias condition, which naturally raises the question whether the temperature dependence of P_C can be explained by the variation of V_1 at different temperatures. However, the change of V_1 would only introduce a monotonic temperature dependence and therefore cannot account for the experimental results. In addition, current-voltage measurements suggest that the change of V_1 with temperature at a given V_T is small and cannot influence the temperature dependence of P_C significantly. Finally, EY and BAP spin relaxation are ignored in the model. However, neither of these mechanisms can explain the observed temperature dependence of P_C . EY spin relaxation rate is proportional to the momentum scattering rate and would give rise to a smaller EL polarization at high temperatures, whereas BAP relaxation is due to electron-hole exchange interactions and cannot cause a non-monotonic temperature dependence. Furthermore, DP spin relaxation in bulk semiconductor has a rate proportional to T^3 [121] and is unlikely to cause such a pronounced non-monotonic temperature dependence. The temperature dependence of P_C is therefore due mainly to DP spin relaxation within the quantum well. DP relaxation is very sensitive to the momentum scattering rate and the semiconductor structure dimensionality. Thus by engineering semiconductor parameters such as the doping concentration or the structure dimensionality, it is possible to manipulate the spin relaxation rate, which can be very useful for designing spintronic devices.

While the presented optical measurements were limited by the quantum well emission efficiency to temperatures below about 100 K, the spin injection is expected to remain efficient up to room temperature due to the high Curie temperature of CoFe and the weak temperature dependence of tunneling. The MgO based tunnel spin injectors can be easily fabricated with magnetron sputtering. Moreover, the MgO barrier prevents the intermixing between the ferromagnetic metal and the semiconductor and thus leads to better thermal stability. These desired features, in combination with their high tunneling spin polarization at high temperature, make the MgO based tunnel spin injectors promising for future spintronic applications.

Chapter 7

Summary

Spin-dependent electron transport in metals and semiconductors is of great importance both scientifically and technologically. The first part of this dissertation focused on such transport in a novel three terminal device combining ferromagnetic metals and semiconductors: the magnetic tunnel transistor. In one type of the magnetic tunnel transistor, a magnetic tunnel junction, comprised of two ferromagnetic metal electrodes separated by a tunnel barrier, is deposited onto a semiconductor substrate. The two ferromagnetic electrodes and the semiconductor form the emitter, base, and collector of the magnetic tunnel transistor, respectively. When an emitter/base bias voltage is applied across the tunnel barrier, spin-polarized electrons are injected from the emitter into the base. A portion of the injected electrons can traverse the base layer while maintaining enough energy to overcome the Schottky barrier at the base/collector interface and form the collector current. Due to spin-dependent electron scattering rates in the base, the collector current strongly depends on the alignment of the emitter and base magnetic moments. The relative change in the collector current, when the alignment is varied from anti-parallel to parallel, is defined as the magneto-current, which is a measure of the magnetic field sensitivity of this device. Large magneto-current values exceeding 100% can be readily obtained in this type of magnetic tunnel transistor.

One advantage of the magnetic tunnel transistor is that the electron energy can

be easily controlled by the emitter/base bias voltage. In addition, the magneto-current and the collector current are very sensitive to the semiconductor collector electronic structure and the spin-dependent scattering processes in the base and at the base/collector interface. Therefore, the magnetic tunnel transistor is a very useful tool to study these scattering processes and to probe the dependence of electron transport on the semiconductor band structure at various electron energies. One such example was to measure the spin-dependent electron attenuation lengths in ferromagnetic thin films grown on GaAs(001). By varying the ferromagnetic base layer thickness and measuring the corresponding variations of the magneto-current and collector current, the majority and minority electron attenuation lengths were extracted for CoFe and NiFe films in the electron energy range of 1 – 1.9 eV. A large spin asymmetry was observed with a majority to minority attenuation length ratio of about 4 – 6. Moreover, it was found that the majority electron attenuation length decreased with the electron energy while the minority electron attenuation length was almost independent of the electron energy in the experimental energy range. This spin asymmetry in electron attenuation lengths can be explained by strong spin-dependent electron-electron scattering in the base.

In another study, the magneto-current was measured as a function of the emitter/base bias voltage for magnetic tunnel transistors with GaAs(001), GaAs(111), and Si(001) collectors. For the magnetic tunnel transistors with GaAs collectors, a pronounced non-monotonic bias voltage dependence of the magneto-current was observed, whereas for the magnetic tunnel transistor with a Si collector the magneto-current decreased monotonically with bias. A model calculation based on spin-dependent inelastic scattering in the base and diffusive scattering at the base/collector interface can well account for the experimental data. The difference between magnetic tunnel transistors with GaAs and Si collectors was attributed to their distinct conduction band structures.

In the magnetic tunnel transistors with a single ferromagnetic base layer, the magneto-current derives from the emitter spin polarization and the spin-filtering effect in the base. While spin-filtering can readily achieve a spin polarization of more than 90% for a base layer of ~ 30 Å or thicker, the emitter spin polarization is typically

less than 50% and eventually limits the magneto-current effect. To realize a higher magnetic field sensitivity, a spin-valve base can be used in a different type of magnetic tunnel transistor, where the emitter is a non-magnetic Cu layer and the spin-valve base consists of a NiFe/Cu/CoFe or NiFe/Au/CoFe sandwich. In this case, the magneto-current results from spin-filtering effects in the NiFe and CoFe layers. Giant magneto-current values of 3400% and 1650% were obtained for magnetic tunnel transistors with GaAs and Si collectors, respectively. Such an extraordinarily high field sensitivity is very attractive for sensor applications. Comparison of the transport properties of magnetic tunnel transistors with NiFe/Cu/CoFe and NiFe/Au/CoFe bases revealed that Cu is a superior spacer material than Au.

There is great interest in integrating the magnetic tunnel transistor with a Si collector since Si is the most widely used semiconducting material. However, ferromagnetic metals deposited directly on Si tend to react with the Si and form a silicide layer, which drastically degrades the device performance. By inserting a non-magnetic seed layer at the base/collector interface, it is possible to reduce such silicide formation and improve the magnetic field sensitivity and transfer ratio of the device. A thorough investigation was conducted on the influence of non-magnetic seed layers (Au, Cu, Pt, Pd, Ta, and Ti) on the magneto-transport properties of magnetic tunnel transistors with a Si collector. A thin Cu or Au seed layer ($\sim 10 - 20 \text{ \AA}$) was found to give the desired improvement.

The magnetic tunnel transistor has very high magnetic field sensitivity. However, the small transfer ratio limits its usefulness as a device. A large part of the electron current loss is due to strong electron scattering at the base/collector interface. By optimizing this interface, it is possible to improve the transfer ratio significantly. The magnetic tunnel transistor operates at bias voltages larger than the base/collector Schottky barrier height. Reducing the Schottky barrier height is important in terms of lowering the device power consumption. Despite these drawbacks, the magnetic tunnel transistor remains a useful tool to study spin-dependent hot electron transport in metals, semiconductors, and at their interfaces.

The second part of this dissertation concentrated on the electrical injection of spin-polarized electron currents into semiconductors, which is an essential component for

semiconductor spintronic devices. The magnetic tunnel transistor is an intriguing spin injector since it can generate a highly spin-polarized hot electron current at room temperature through spin-filtering in the base. A quantum well light emitting diode can be used as an optical detector of the spin injection efficiency. The electron spin polarization is correlated to the circular polarization of the quantum well electroluminescence by the optical selection rules. Successful hot electron spin injection into GaAs at an energy of ~ 2 eV was demonstrated for the first time using the magnetic tunnel transistor, with a lower bound of 10% spin polarization at 1.4 K. This moderate polarization was most likely a consequence of significant electron spin relaxation in the semiconductor at such a high energy. In contrast to the magnetic tunnel transistor injector, much higher spin injection efficiency was found for a two terminal spin injector formed from a CoFe/MgO magnetic tunnel structure, where a spin polarization of at least $\sim 50\%$ was observed at 100 K. Measurements at higher temperatures were limited only by the quantum well light emission efficiency. The electroluminescence polarization varied non-monotonically with temperature and decreased with bias at a given temperature, which was consistent with dominating DP spin relaxation within the quantum well.

The optical measurements with a quantum well detector are useful for demonstration of spin injection into semiconductors. For device applications, however, both electrical injection and detection are desired. The MgO based tunnel structure may be used as both the spin injector and detector for future spintronic devices because it can offer a large tunneling spin polarization at high temperatures and can be easily integrated into existing fabrication techniques.

Bibliography

- [1] G. E. Moore, *Electronics* **38**, 114 (1965).
- [2] S. A. Wolf *et al.*, *Science* **294**, 1488 (2001).
- [3] M. N. Baibich, J. M. Broto, A. Fert, F. Nguyen Van Dau, and F. Petroff, *Phys. Rev. Lett.* **61**, 2472 (1988).
- [4] G. Binasch, P. Grünberg, F. Saurenbach, and W. Zinn, *Phys. Rev. B* **39**, 4828 (1989).
- [5] S. S. P. Parkin, N. More, and K. P. Roche, *Phys. Rev. Lett.* **64**, 2304 (1990).
- [6] S. S. P. Parkin, R. Bhadra, and K. P. Roche, *Phys. Rev. Lett.* **66**, 2152 (1991).
- [7] M. Julliere, *Phys. Lett.* **54A**, 225 (1975).
- [8] T. Miyazaki and N. Tezuka, *J. Magn. Magn. Mater.* **139**, L231 (1995).
- [9] J. S. Moodera, L. R. Kinder, T. M. Wong, and R. Meservey, *Phys. Rev. Lett.* **74**, 3273 (1995).
- [10] S. Parkin *et al.*, *Proc. IEEE* **91**, 661 (2003).
- [11] S. S. P. Parkin *et al.*, *J. Appl. Phys.* **85**, 5828 (1999).
- [12] D. J. Monsma, J. C. Lodder, T. J. A. Popoma, and B. Dieny, *Phys. Rev. Lett.* **74**, 5260 (1995).
- [13] D. J. Monsma, R. Vlutters, and J. C. Lodder, *Science* **281**, 407 (1998).

- [14] R. Jansen *et al.*, Phys. Rev. Lett. **85**, 3277 (2002).
- [15] K. Mizushima, T. Kinno, T. Yamauchi, and K. Tanaka, IEEE Trans. Magn. **33**, 3500 (1997).
- [16] R. Sato and K. Mizushima, Appl. Phys. Lett. **79**, 1157 (2001).
- [17] S. van Dijken, X. Jiang, and S. S. P. Parkin, Appl. Phys. Lett. **80**, 3364 (2002).
- [18] W. H. Meiklejohn and C. P. Bean, Phys. Rev. **102**, 1413 (1956).
- [19] S. van Dijken, X. Jiang, and S. S. P. Parkin, Appl. Phys. Lett. **82**, 775 (2003).
- [20] S. van Dijken, X. Jiang, and S. S. P. Parkin, Appl. Phys. Lett. **83**, 951 (2003).
- [21] D. J. Monsma and S. S. P. Parkin, Appl. Phys. Lett. **77**, 883 (2000).
- [22] S. van Dijken, X. Jiang, and S. S. P. Parkin, Phys. Rev. B **66**, 094417 (2002).
- [23] D. P. Pappas *et al.*, Phys. Rev. Lett. **66**, 504 (1991).
- [24] H.-J. Drouhin, A. J. van der Sluijs, Y. Lassailly, and G. Lampel, J. Appl. Phys. **79**, 4734 (1996).
- [25] D. Oberli, R. Burgermeister, S. Riesen, W. Weber, and H. C. Siegmann, Phys. Rev. Lett. **81**, 4228 (1998).
- [26] E. Y. Tsybal and D. G. Pettifor, Phys. Rev. B **54**, 15314 (1996).
- [27] M. Aeschlimann *et al.*, Phys. Rev. Lett. **79**, 5158 (1997).
- [28] R. Vlutters, O. M. J. van 't Erve, S. D. Kim, R. Jansen, and J. C. Lodder, Phys. Rev. Lett. **88**, 027202 (2002).
- [29] W. H. Rippard and R. A. Buhrman, Phys. Rev. Lett. **84**, 971 (2000).
- [30] G. Schönhense and H. C. Siegmann, Ann. Phys. (Leipzig) **2**, 465 (1993).
- [31] M. Getzlaff, J. Bansmann, and G. Schönhense, Solid State Commun. **87**, 467 (1993).

- [32] J. C. Gröbli, D. Oberli, and F. Meier, Phys. Rev. B **52**, R13095R13097 (1995).
- [33] E. Vescovo *et al.*, Phys. Rev. B **52**, 13497 (1995).
- [34] L. D. Bell, Phys. Rev. Lett. **77**, 3893 (1996).
- [35] J. J. Quinn, Phys. Rev. **126**, 1453 (1962).
- [36] E. Zarate, P. Apell, and P. M. Echenique, Phys. Rev. B **60**, 4309 (1999).
- [37] R. Knorren, K. H. Bennemann, R. Burgermeister, and M. Aeschlimann, Phys. Rev. B **61**, 9427 (2000).
- [38] H.-J. Drouhin, Phys. Rev. B **62**, 556 (2000).
- [39] H.-J. Drouhin, J. Appl. Phys. **80**, 6805 (2001).
- [40] J. K. M. Plihal, D. L. Mills, Phys. Rev. Lett. **82**, 2579 (1999).
- [41] J. Hong and D. L. Mills, Phys. Rev. B **59**, 13840 (1999).
- [42] J. Hong and D. L. Mills, Phys. Rev. B **62**, 5589 (2000).
- [43] M. P. Gokhale and D. L. Mills, Phys. Rev. Lett. **66**, 2251 (1991).
- [44] W. A. Harrison, *Solid State Theory*, (Dover, New York, 1980).
- [45] S. A. Chambers *et al.*, Phys. Rev. B **34**, 6605 (1986).
- [46] F. Xu *et al.*, Phys. Rev. B **35**, 2375 (1987).
- [47] S. A. Chambers and V. A. Loebis, Appl. Phys. Lett. **60**, 38 (1992).
- [48] P. R. Hammar, B. R. Bennett, M. J. Yang, and M. Johnson, Phys. Rev. Lett. **83**, 203 (1999).
- [49] S. Gardelis, C. G. Smith, C. H. W. Barnes, E. H. Lindfield, and D. A. Ritchie, Phys. Rev. B **60**, 7764 (1999).

- [50] G. Schmidt, D. Ferrand, L. W. Molenkamp, A. T. Filip, and B. J. van Wees, Phys. Rev. B **62**, 4790 (2000).
- [51] A. T. Filip *et al.*, Phys. Rev. B **62**, 9996 (2000).
- [52] C. M. Hu, J. Nitta, A. Jensen, J. B. Hansen, and H. Takayanagi, Phys. Rev. B **63**, 125333 (2001).
- [53] E. I. Rashba, Phys. Rev. B **62**, R16267 (2000).
- [54] A. Fert and H. Jaffrés, Phys. Rev. B **64**, 184420 (2001).
- [55] S. van Dijken, X. Jiang, and S. S. P. Parkin, Phys. Rev. Lett. **90**, 197203 (2003).
- [56] X. Jiang, S. van Dijken, R. Wang, and S. S. P. Parkin, Phys. Rev. B **69**, 014413 (2004).
- [57] D. Guthrie *et al.*, Phys. Rev. B **54**, 16972 (1996).
- [58] D. Smith, E. Lee, and V. Narayanamurti, Phys. Rev. Lett. **80**, 2433 (1998).
- [59] D. Smith, M. Kozhevnikov, E. Lee, and V. Narayanamurti, Phys. Rev. B **61**, 13914 (2000).
- [60] J. S. Blakemore, J. Appl. Phys. **53**, R123 (1982).
- [61] T. Yamauchi and K. Mizushima, Phys. Rev. B **61**, 8242 (2000).
- [62] C. A. Ventrice Jr., V. P. LaBella, G. Ramaswamy, H. P. Yu, and L. J. Schowalter, Phys. Rev. B **53**, 3952 (1996).
- [63] Z.-J. Ding and R. Shimizu, Scanning **18**, 92 (1996).
- [64] M. K. Weilmeier, W. H. Rippard, and R. A. Buhrman, Phys. Rev. B **59**, R2521R2524 (1999).
- [65] S. S. P. Parkin, Z. G. Li, and D. J. Smith, Appl. Phys. Lett. **58**, 2710 (1991).
- [66] S. S. P. Parkin, Phys. Rev. Lett. **71**, 1641 (1993).

- [67] M. D. Stiles, J. Appl. Phys. **79**, 5805 (1996).
- [68] P. Zahn, J. Binder, I. Mertig, R. Zeller, and P. H. Dederichs, Phys. Rev. Lett. **80**, 2326 (1998).
- [69] J. J. Sun and P. P. Freitas, J. Appl. Phys. **85**, 5264 (1999).
- [70] P. LeClair, H. J. M. Swagten, J. T. Kohlhepp, R. J. M. van de Veerdonk, and W. J. M. de Jonge, Phys. Rev. Lett. **84**, 2933 (2000).
- [71] P. Lambin and F. Herman, Phys. Rev. B **30**, 6903 (1984).
- [72] I. Turek, J. Kudrnovský, V. Drchal, and P. Weinberger, Phys. Rev. B **49**, 3352 (1994).
- [73] J. M. Gallego, R. Miranda, S. Molodtsov, C. Laubschat, and G. Kaindl, Surf. Sci. **239**, 203 (1990).
- [74] G. Rangelov, P. Augustin, J. Stober, and T. Fauster, Surf. Sci. **307-309**, 264 (1994).
- [75] K. Prabhakaran and T. Ogino, Appl. Surf. Sci. **100/101**, 518 (1996).
- [76] Y.-E. Wu, J.-S. Tsay, S.-C. Chen, T.-Y. Fu, and C.-S. Shern, Jpn. J. Appl. Phys. **40**, 6825 (2001).
- [77] J. M. Gallego, J. M. García, J. Alvarez, and R. Miranda, Phys. Rev. B **46**, 13339 (1992).
- [78] K. Konuma *et al.*, J. Appl. Phys. **73**, 1104 (1993).
- [79] G. Crecelius, Appl. Surf. Sci. **65/66**, 683 (1993).
- [80] E. V. Chubunova, I. D. Khabelashvili, Y. Y. Lebedinskii, V. N. Nevolin, and A. Zenkevich, Thin Solid Films **247**, 39 (1994).
- [81] R. Kläsages *et al.*, Phys. Rev. B **56**, 10801 (1997).

- [82] F. Zavaliche, W. Wulfhekel, H. Xu, and J. Kirschner, *J. Appl. Phys.* **88**, 5289 (2000).
- [83] C. L. Platt, A. E. Berkowitz, D. J. Smith, and M. R. McCartney, *J. Appl. Phys.* **88**, 2058 (2000).
- [84] R. C. O'Handley, *Modern Magnetic Materials: Principles and Applications*, (Wiley, New York, 2000).
- [85] S. S. Li, *Semiconductor Physical Electronics*, (Plenum, New York, 1993).
- [86] R. Naik *et al.*, *J. Magn. Magn. Mater.* **121**, 60 (1993).
- [87] M. Shima, L. Salamanca-Riba, T. P. Moffat, R. D. McMichael, and L. J. Swartzendruber, *J. Appl. Phys.* **84**, 1504 (1998).
- [88] B. G. Demczyk, R. Naik, G. Auner, C. Kota, and U. Rao, *J. Appl. Phys.* **75**, 1956 (1994).
- [89] K. Oura and T. Hanawa, *Surf. Sci.* **82**, 202 (1979).
- [90] M. Hanbücken, Z. Imam, J. J. Méoïs, and G. Le Lay, *Surf. Sci.* **162**, 628 (1985).
- [91] K. Hricovini *et al.*, *Surf. Sci.* **211/212**, 630 (1989).
- [92] X. F. Lin and J. Nogami, *J. Vac. Sci. Technol. B* **12**, 2090 (1994).
- [93] E. Landree, D. Grozea, C. Collazo-Davila, and L. D. Marks, *Phys. Rev. B* **55**, 7910 (1997).
- [94] J. H. Kim, G. Yang, S. Yang, and A. H. Weiss, *Surf. Sci.* **475** (2001).
- [95] J. R. Abelson *et al.*, *J. Appl. Phys.* **63**, 689 (1988).
- [96] Y. C. Liu, T. P. Chen, S. Fung, and C. D. Beling, *J. Appl. Phys.* **76**, 7423 (1994).
- [97] D. M. Solina *et al.*, *Thin Solid Films* **372**, 94 (2000).

- [98] S. Okada, K. Oura, T. Hanawa, and K. Satoh, *Surf. Sci.* **97**, 88 (1980).
- [99] G. W. Rubloff, P. S. Ho, J. F. Freeouf, and J. E. Lewis, *Phys. Rev. B* **23**, 4183 (1981).
- [100] R. M. Tromp, E. J. van Loenen, M. Iwami, R. G. Smeenk, and F. W. Saris, *Surf. Sci.* **124**, 1 (1983).
- [101] A. Noya, M. Takeyama, K. Sasaki, and T. Nakanishi, *J. Appl. Phys.* **76**, 3893 (1994).
- [102] R. Larciprete, M. Danailov, A. Barinov, L. Gregoratti, and M. Kiskinova, *J. Appl. Phys.* **90**, 4361 (2001).
- [103] J. M. Kikkawa and D. D. Awschalom, *Phys. Rev. Lett.* **80**, 4313 (1998).
- [104] J. M. Kikkawa and D. D. Awschalom, *Nature* **397**, 139 (1999).
- [105] H. Ohno *et al.*, *Nature* **408**, 944 (2000).
- [106] O. Z. Karimov *et al.*, *Phys. Rev. Lett.* **91**, 246601 (2003).
- [107] S. Datta and B. Das, *Appl. Phys. Lett.* **56**, 665 (1990).
- [108] D. Loss and D. P. DiVincenzo, *Phys. Rev. A* **57**, 120 (1998).
- [109] I. Žutić, J. Fabian, and S. Das Sarma, *Phys. Rev. Lett.* **88**, 066603 (2002).
- [110] J. Fabian, I. Žutic, and S. Das Sarma, *Phys. Rev. B* **66**, 165301 (2002).
- [111] R. Fiederling *et al.*, *Nature* **402**, 787 (1999).
- [112] Y. Ohno *et al.*, *Nature* **402**, 790 (1999).
- [113] B. T. Jonker *et al.*, *Phys. Rev. B* **62**, 8180 (2000).
- [114] H. J. Zhu *et al.*, *Phys. Rev. Lett.* **87**, 016601 (2001).
- [115] A. T. Hanbicki, B. T. Jonker, G. Itskos, G. Kioseoglou, and A. Petrou, *Appl. Phys. Lett.* **80**, 1240 (2002).

- [116] A. T. Hanbicki *et al.*, Appl. Phys. Lett. **82**, 4092 (2003).
- [117] V. F. Motsnyi *et al.*, Appl. Phys. Lett. **81**, 265 (2002).
- [118] T. Manago and H. Akinaga, Appl. Phys. Lett. **81**, 694 (2002).
- [119] P. Van Dorpe *et al.*, Jpn. J. Appl. Phys. **42**, L502 (2003).
- [120] S. Krishnamurthy, M. van Schilfgaarde, and N. Newman, Appl. Phys. Lett. **83**, 1761 (2003).
- [121] F. Meier and B. P. Zakharchenya, *Optical Orientation*, (North-Holland, New York, 1984).
- [122] R. J. Elliott, Phys. Rev. **96**, 266 (1954).
- [123] Y. Yafet, in *Solid State Physics*, edited by F. Seitz and D. Turnbull, volume 14, Academic, New York, 1963.
- [124] M. I. D'yakonov and V. I. Perel', Sov. Phys. JETP **33**, 1053 (1971).
- [125] M. I. D'yakonov and V. Yu. Kachorovskii, Sov. Phys. Semicond **20**, 110 (1986).
- [126] G. L. Bir, A. G. Aronov, and G. E. Pikus, Sov. Phys. JETP **42**, 705 (1976).
- [127] T. Amand *et al.*, Phys. Rev. B **50**, 11624 (1994).
- [128] J. Fabian and S. Das Sarma, J. Vac. Sci. Technol. B **17**, 1708 (1999).
- [129] W. H. Butler, X.-G. Zhang, T. C. Schulthess, and J. M. MacLaren, Phys. Rev. B **63**, 054416 (2001).
- [130] J. Mathon and A. Umerski, Phys. Rev. B **63**, 220403(R) (2001).
- [131] S. S. P. Parkin *et al.*, (unpublished).
- [132] H. Sanada *et al.*, Appl. Phys. Lett. **81**, 2788 (2002).
- [133] V. I. Puller, L. G. Mourokh, and N. J. M. Horing, Phys. Rev. B **67**, 155309 (2003).

[134] C. M. Wolfe, G. E. Stillman, and W. T. Lindley, *J. Appl. Phys.* **41**, 3088 (1970).

[135] H. Ehrenreich, *Phys. Rev.* **120**, 1951 (1960).

[136] K. Hess, *Appl. Phys. Lett.* **35**, 484 (1979).